Technische Universität München

Max-Planck-Institut für Physik
(Werner-Heisenberg-Institut)

Top-Quark and Top-Squark Production at Hadron Colliders at Electroweak NLO

Monika Kollár

To Dano

Abstract

In this work, the impact of $\mathcal{O}(\alpha)$ contributions on the cross sections for the top-quark pair production within the SM and for the top-squark pair production within the MSSM is investigated. For these processes, the EW–QCD interference leads to additional contributions at $\mathcal{O}(\alpha\alpha_{\mathrm{s}}^2)$ level which are not present at Born-level. In addition, parton densities at NLO QED give rise to non-zero photon density in the proton. It is shown that the size of photon-induced production rates is comparable to other EW NLO contributions. The cross sections differential in $\sqrt{\hat{s}}$ and p_{T} are studied and discussed in kinematic ranges accessible at the LHC and at the Tevatron. The NLO EW contributions become significant at high p_{T} and high $\sqrt{\hat{s}}$ and should be included in the numerical analysis.

Contents

Chapter 1

Introduction

Over the twentieth century, unceasing theoretical and experimental efforts in particle physics were concentrated on building a model that would describe the basic elements of nature in a consistent way. It was found that the protons and neutrons in the nuclei are not fundamental objects, but they are composed of quarks, which together with the leptons are considered to be the elementary particles. The fundamental forces of strong, weak and electromagnetic interactions are widely believed to be described by quantum field theories based on local gauge symmetries. The elementary particles can then interact through exchange of gauge field quanta (gluons, weak bosons and photons). All of this knowledge is embedded into the currently established model of elementary particle physics, the Standard Model (SM) [1–4]. Only the fourth fundamental force, gravity, is not yet included in the quantum theory picture.

After many years of testing, which proved that the Standard Model is an impressively consistent theory for the energy ranges accessible at colliders up to now [5], it has become clear that it is not the ultimate theory. Indeed, many deficiencies such as the hierarchy problem, the dark matter origin problem, or the coupling unification at some higher scale require new physics which might already be present at the TeV scale. With the startup of the Large Hadron Collider (LHC) at CERN, a revolution in high energy particle physics might be at hand.

Supersymmetric models are very popular candidates for the SM extension. They introduce a new symmetry between fermions and bosons which enables the solving of many of the SM problems. From the phenomenological point of view, supersymmetric theories are rich in new particles which can be searched for at colliders. Unlike the SM, supersymmetric models introduce more than one Higgs boson, and typically one of them is required to be light and thus within accessible energy range. For these reasons, searches for the Higgs boson(s) and supersymmetric particles are considered to be among the main tasks of the LHC program.

Due to the high precision expected at the LHC, comparison of experimental results with theoretical predictions allows to further test the consistency of the SM. Precise understanding of the SM predictions is crucial in the searches for new physics, where the SM processes are important contributions to the background. In this context, the role of quantum corrections as a tool to achieve high theoretical accuracy is essential. At hadron colliders, the largest higher-order contributions arise from the quarks and gluons and are referred to as QCD corrections. The current status in this field is typically beyond the next-to-leading-order (NLO). For a complete one-loop treatment, also contributions from the electroweak (EW) sector require closer inspection. From intuitive expectations, these are comparable in size with the next-to-next-to-leading-order (NNLO) in QCD, however, in some cases this might not be true.

In this work, we study the effects of higher-order contributions from the EW sector on specific production processes at the LHC within the SM and within its minimal supersymmetric extension, the Minimal Supersymmetric Standard Model (MSSM) [6, 7]. We investigate the numerical impact of the EW corrections on the total hadronic cross sections as well as on the differential hadronic cross sections where these effects can typically become sizeable.

In the first part of our studies, we concentrate on the production of top quark pairs. Top quark physics is expected to be the one field of LHC interest where both accurate SM tests and searches for new physics will be carried out. The current uncertainties for the top quark observables, as obtained at the Tevatron collider at Fermilab, are expected to be further reduced at the LHC. In this context precise predictions for the top quark pair production cross section become a necessity.

In the second part of our work, we study the SUSY-EW corrections to the production of top-squark pairs within the MSSM. Top-squarks are the supersymmetric partners of the top quarks and in many supersymmetric models, they are one of the candidates for the lightest squark. At the LHC, the production of squarks and gluinos is expected to yield the largest contributions to the total production rate of supersymmetric particles. In this context, the top-squark pair production cross section, which essentially dependes only on the top-squark mass and very little on other supersymmetric parameters, can be used to directly extract the top-squark mass in case of a discovery. In this sense it can provide a direct measurement of a supersymmetric parameter and thus can be used to constrain models of supersymmetry breaking. In our analysis, we assume the CP-conserving MSSM with real parameters and *R-parity* conservation.

The outline of this thesis is as follows: In chapter 2, a short introduction to the SM is given. The deficiencies of the SM are emphasized to motivate the efforts for its extension.

In chapter 3 we first discuss basic principles of supersymmetric theories, then present basic ingredients which are necessary to build a supersymmetric model. Further, we focus on the simplest supersymmetric extension of the SM, the MSSM, and explain in detail the particle content of the model.

In chapter 4 we present the methods of regularization and renormalization which are necessary tools for higher order calculations. We introduce basic concepts for the regularization procedures, which allow divergences that appear in the loop integrals to be handled and also the renormalization schemes that are needed to restore the physical meaning of the calculated quantities.

Chapter 5 is dedicated to the calculations of cross sections at the hadronic level. In the first part we briefly introduce the parton model, which provides the necessary link between perturbation theory, which describes the interactions of partons, and the observable interactions of hadrons. In this context, the notion of factorization is essential. In the last part of this chapter, we comment on the effects of including the NLO QED contributions into the parton distribution functions.

In chapter 6 we present our studies of top-quark pair production at NLO in QED and investigate the impact of QED corrections on the total hadronic cross sections as well as on the differential hadronic cross sections at the Tevatron and at the LHC. The QED corrections form a subclass of the full EW corrections within the SM and require treatment of infrared (IR) singularities which are related to the null photon mass. Also, it is necessary to consider effects of the QED–QCD interference which is a natural consequence of hadronic interactions.

In chapter 7 we discuss the SUSY-EW corrections to the top-squark pair production cross section and present calculations for the total and differential hadronic cross sections. Again, we investigate also the energy ranges of the Tevatron, but we focus on the LHC owing to its discovery potential. As the QED-like contributions are included in the SUSY-EW corrections, it is necessary to compensate for IR singularities related to the photon and take into account the QED–QCD interference.

Chapter 2

Standard Model

2.1 Basics of the Standard Model

The Standard Model (SM) [1–4] is the commonly established theory of elementary particle physics. It is one of the best tested theories in physics and its predictions impressively agree with experimental data [5].

Within the SM three universal interactions are described at quantum level by the non-Abelian gauge group of a direct product of $SU(3)_C \times SU(2)_L \times U(1)_Y$. The color gauge group $SU(3)_C$ forms the base of strong interactions while electromagnetic and weak interactions are unified under the electroweak gauge symmetry $SU(2)_L \times U(1)_Y$. Within each group the group generators correspond to spin-1 gauge bosons, which mediate the interactions among constituents of the matter. Counting the number of generators, there are eight gauge bosons for $SU(3)_C$, called gluons, three gauge bosons for $SU(2)_L$ and one for $U(1)_Y$, called W and B bosons, respectively. The gauge bosons transform under the adjoint representation of the respective group.

The fundamental constituents of matter are spin-$\frac{1}{2}$ particles, the fermions. There are two types of fermions: quarks, which have non-zero color charge and leptons, which are color-neutral. For this reason only the quarks interact via strong interactions. Furthermore, the quarks as well as the leptons appear in three generations. Within each generation the left-handed components of fermions transform as doublets while the right-handed components transform as singlets under $SU(2)_L$. This has no impact on the transformations under $SU(3)_C$. Therefore the strong interactions are blind to the left–right asymmetry and to the flavor. The structure of the fermionic sector is summarized in Table 2.1. The right-handed neutrinos are not included in the SM and the neutrino masses are set to zero. Although there is evidence for the non-zero neutrino masses from the flavor-changing experiments [5], these effects are completely negligible at large colliders [8]. Therefore for collider physics without the loss of generality,

Table 2.1: Classification of the SM fermions. Left-handed doublets and right-handed singlets within each generation are shown together with electroweak quantum numbers. I_3 is the third component of the weak isospin I, Y is the weak hypercharge and Q is the electric charge.

Fermions				I_3	Y	Q
quarks	$\begin{pmatrix} u \\ d \end{pmatrix}_L$	$\begin{pmatrix} c \\ s \end{pmatrix}_L$	$\begin{pmatrix} t \\ b \end{pmatrix}_L$	$\frac{1}{2}$ $-\frac{1}{2}$	$\frac{1}{3}$ $\frac{1}{3}$	$\frac{2}{3}$ $-\frac{1}{3}$
	u_R	c_R	t_R	0	$\frac{4}{3}$	$\frac{2}{3}$
	d_R	s_R	b_R	0	$-\frac{2}{3}$	$-\frac{1}{3}$
leptons	$\begin{pmatrix} \nu_e \\ e \end{pmatrix}_L$	$\begin{pmatrix} \nu_\mu \\ \mu \end{pmatrix}_L$	$\begin{pmatrix} \nu_\tau \\ \tau \end{pmatrix}_L$	$\frac{1}{2}$ $-\frac{1}{2}$	-1 -1	0 -1
	e_R	μ_R	τ_R	0	-2	-1

neutrinos can be considered to be strictly massless within the SM.

If the SM was a theory with an exact gauge symmetry all gauge bosons would be massless. This is true for the gluons but as shown by experiments it does not apply to all gauge bosons in the electroweak sector [5]. For this reason electroweak symmetry has to be broken in the SM. However, in order to preserve gauge invariance of the SM Lagrangian it is not possible to introduce explicit mass terms. Thus another mechanism has been invented, the Higgs mechanism, which breaks the electroweak symmetry spontaneously [9].

The idea of Higgs mechanism is to introduce into the Lagrangian a new complex scalar field Φ, which behaves like a doublet under the $SU(2)_L$ and has a non-zero vacuum expectation value (VEV) v. The Higgs potential can be written as

$$V(\Phi) = -\frac{m_H^2}{2}\left(\Phi^\dagger \Phi\right) + \frac{m_H^2}{2v^2}\left(\Phi^\dagger \Phi\right)^2 , \tag{2.1}$$

where m_H denotes the Higgs mass. In this way the invariance of the Lagrangian under $SU(2)_L \times U(1)_Y$ is preserved, but as a consequence of the non-zero VEV, the ground state of the Lagrangian is no longer invariant under the electroweak symmetry. Still it remains invariant under the symmetry of electromagnetic interactions $U(1)_Q$ with the electric charge Q defined as $Q = I_3 + \frac{Y}{2}$. Here Y is the weak hypercharge and I_3 is the third component of the weak isospin.

After electroweak symmetry breaking all particles of the SM acquire their masses via interactions with the Higgs field. In the electroweak sector the gauge boson triplet W_μ^i, $i = 1\ldots3$ of $SU(2)_L$ and the gauge boson B_μ of $U(1)_Y$ are rotated into mass

eigenstates of the theory as

$$W_\mu^\pm = \frac{1}{\sqrt{2}} \left(W_\mu^1 \mp i W_\mu^2 \right), \quad Z_\mu = c_W W_\mu^3 - s_W B_\mu, \quad A_\mu = c_W W_\mu^3 + s_W B_\mu. \quad (2.2)$$

Here s_W and c_W denote sine and cosine of the electroweak mixing angle. The two W bosons, which have non-zero electric charge, and the neutral Z boson receive masses proportional to the VEV v of the Higgs field:

$$m_W = \frac{e}{2s_W} v, \qquad m_Z = \frac{e}{2s_W c_W} v, \qquad (2.3)$$

where e is the elementary unit charge. The neutral boson A is identified as photon and remains massless owing to the unbroken electromagnetic $U(1)_Q$ symmetry.

In analogy to the symmetry breaking in the gauge sector, Yukawa interaction terms are introduced to couple the fermions to the Higgs field. This allows for the fermion masses. For massless neutrinos there is no difference between the flavor eigenstates and the mass eigenstates in the leptonic sector. In the quark sector, however, the flavor eigenstates are rotated into the mass eigenstates as described by the Cabbibo-Kobayashi-Maskawa (CKM) matrix [10]. Due to the unitarity of the CKM matrix the mixing is absent in the interactions mediated by neutral currents. The CKM matrix can be set to the identity matrix if effects related to the quark mixing can be neglected.

In the Higgs sector of the SM the electroweak symmetry breaking results in one massive scalar boson, the Higgs boson, and three massless scalars, the Goldstone bosons [11]. The massless scalars are unphysical and can be eliminated by an appropriate choice of the gauge, the unitary gauge. The degrees of freedom of the unphysical Goldstone bosons are retransformed into longitudinal modes, which are necessary for the massive vector bosons. The Higgs boson itself is the only particle within the SM, which has not yet been experimentally observed. Its mass is not predicted within the SM, but there are constraints from the requirement of consistent perturbation theory [12]. Direct experimental searches yield a lower limit on $m_H \geq 114.4$ GeV [13]. The best fit determined from all precision electroweak data (all high Q^2 data) gives $m_H = 85^{+39}_{-28}$ GeV [14].[1]

To complete the SM Lagrangian gauge-fixing and ghost terms have to be introduced. The fixing of gauge is necessary for the quantization. Due to the gauge invariance any choice of gauge is allowed. Working in the unitary gauge has the advantage that no unphysical intermediate particles occur. However, for a systematic treatment of quantization it is better to use a renormalizable gauge. The renormalizability of the SM [16] allows to make predictions for measurable quantities by considering only a

---

[1]An independent global fit to all data in [15] yields $m_H = 84^{+32}_{-25}$ GeV.

finite number of higher order contributions within the perturbative expansion. Usually gauge-fixing of the 't Hooft type is used:

$$\mathcal{L}_{R_\xi} = -\frac{1}{2\xi_G}\left(\partial_\mu G^{a\mu}\right)^2 - \frac{1}{2\xi_A}\left(\partial_\mu A^\mu\right)^2 - \frac{1}{2\xi_Z}\left(\partial_\mu Z^\mu + M_Z\xi_Z G^0\right)^2$$
$$-\frac{1}{2\xi_W}\left|\partial_\mu W^{+\mu} + iM_W\xi_W G^+\right|^2, \tag{2.4}$$

with gluon fields $G^{a\mu}$, photon field A^μ, vector boson fields Z^μ and $W^{\pm\mu}$ and Goldstone bosons G^0 and $G^\pm$. The parameters $\xi^{A,Z,W}$ are arbitrary. Finally, the unphysical degrees of freedom of the gauge bosons which were introduced by the gauge-fixing are compensated with the Faddeev–Popov ghost terms [17]. For practical applications the 't Hooft-Feynman gauge is used with parameters $\xi^A = \xi^Z = \xi^W = 1$. In this gauge propagators of the gauge bosons have a simple form. Also, masses of the unphysical Goldstone and ghost fields are equal to masses of the corresponding physical fields.

After adding the gauge-fixing and ghost terms, the SM Lagrangian becomes suitable for higher order calculations.

2.2   Open questions and the role of quantum corrections

As already mentioned in the previous section, predictions of the SM are in an impressive agreement with experimental results. This is due to the high precision achieved in the experiments as well as in the theoretical calculations. In the context of perturbation theory it is possible to reach higher precision by including higher order contributions. Over the past years many radiative corrections have been worked out and helped to improve and stabilize the SM predictions.

Despite this remarkable success the conceptual situation within the SM is still unsatisfactory. There are open questions left, which point out that the SM cannot be the ultimate theory.
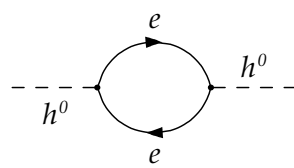
The first obstruction is due to the nonexistence of a quantum theory of gravity. At very large energy scales, of the order of the Planck scale $M_{\text{Planck}} \sim 10^{19}$ GeV, gravitational effects become comparable with other interactions and can no longer be ignored. However, it is not possible to include gravity into the SM because there is no consistent quantum theory of gravity available. For this reason the SM can only be a low-energy approximation of some not yet known fundamental theory.

Following this argument reveals another problem. If the SM originates from symmetry breaking of an underlying theory, all coupling constants have to unify at some

large scale. This scale is usually refered to as the Grand Unification Theory (GUT) scale and is typically of the order of $M_{\mathrm{GUT}} \sim 10^{15}$ GeV. Within a GUT model all three SM gauge groups merge into a single GUT gauge group. Possible candidates are $SU(5)$ [18] or $SO(10)$ [19]. However, GUT theories based on the $SU(5)$ group are already excluded by experiments. Their predictions for the proton lifetime are much smaller than the experimental limit [20]. Nevertheless, within the SM the unification of couplings is not realized [18]. Even with an assumption that potential new particles at the GUT scale might modify the running of couplings, the unification cannot be reached.

To find a proper way of how to include the SM into a GUT theory without further extensions seems to be a tedious task. A straightforward solution is to simply abandon this approach and focus on the hypothesis that the SM is valid up to the Planck scale.

Here another problem emerges, the infamous hierarchy problem [21, 22]. The origin of this problem is in the quadratic divergences which occur in the quantum corrections to the self-energy of the Higgs field (Fig. 2.1). To regulate these divergences one can introduce an ultraviolet momentum cut-off Λ_{UV} (see section 4.1), which can be interpreted as the energy scale of new physics. If we consider the SM to be valid up to the Planck scale, then the cut-off Λ_{UV} is of the order of M_{Planck}. Higher order corrections to the Higgs self-energy, which is connected to the Higgs-mass squared, are proportional to Λ_{UV}^2 and thus to M_{Planck}^2. However, the physical Higgs-mass squared is only of the order of $m_H^2 \sim (100\,\mathrm{GeV})^2$, which leads to a difference of about 30 orders of magnitude. An extreme "fine tunning" is necessary to obtain a physical mass of correct order of magnitude after including the higher order corrections. Obviously, it seems unnatural for the physical Higgs mass to be as small as it is favored by the precision experiments [14] (see section 2.1), unless there is new physics at much lower scale than the Planck scale.

$$\propto \int_{k^0 < \Lambda_{\mathrm{UV}}} d^4k \; \frac{1}{\not{p} + \not{k} - m_e} \frac{1}{\not{k} - m_e}$$

$$\approx \int_0^{\Lambda_{\mathrm{UV}}} k \; dk \quad \propto \Lambda_{\mathrm{UV}}^2$$

Figure 2.1: Electron-loop contribution to the self-energy of Higgs boson corresponds to an ultraviolet-divergent loop integral which is regularized by a cut-off Λ_{UV}. In this way the radiative corrections become proportional to Λ_{UV}^2.

Besides the problem that the Higgs mass is so small with respect to the Planck scale, fermion masses also differ by several orders of magnitude from each other. The pattern that occurs in their rearrangement is also not understood by the theory. Moreover, values of the masses are not predicted and contribute to a large number of free parameters within the SM, which have to be determined in experiments. This also makes the SM unfavorable against some underlying theory with smaller number of free parameters.

To complete the list of open questions in the SM it is necessary to mention the problem of the unknown origin of dark matter. According to the precision measurements of the cosmic microwave background [23] our universe consists of about 23% of non-baryonic weakly interacting matter, the dark matter. However, there is no appropriate SM candidate for the dark matter. The only suitable weakly interacting SM particles — the neutrinos, are not sufficient to account for the total amount of the dark matter as required by the measurements.

Various extensions of SM have been proposed in attempt to solve these problems. Most promising candidates are based on the concept of supersymmetry which will be discussed in the next chapter. Still, the problems do not diminish the importance of the SM. Precise understanding of the SM plays a crucial role in the searches for new physics. In this sense precise predictions based on the higher order calculations are a powerful tool to check the consistency of the SM. Observing deviations from the SM predictions contributes to indirect evidence for physics beyond the SM and eventually might give constraints on the proposed candidates.

Chapter 3

Supersymmetry

3.1 Motivation for supersymmetry

Although there are numerous deficiencies within the Standard Model as mentioned in the previous chapter, the idea of supersymmetry was originally motivated by different arguments. It was shown by Coleman and Mandula [24] that combining space-time and internal symmetries is possible only in a trivial way. The existence of a non-trivial extension of the Poincaré space-time symmetry was initially surprising. As proven by Haag, Łopuszánski and Sohnius [25] such an extension is possible if one gives up the commutator structure of the internal symmetry and postulates anticommutator relations instead. This approach leads to non-trivial commutator relations between the generators of internal symmetry and the Poincaré generators. In this way supersymmetry is established being the only possible non-trivial extension of the Poincaré symmetry [25], in terms of the supersymmetric Poincaré algebra:

$$
\begin{aligned}
\left\{Q_\alpha{}^A, \bar{Q}_{\dot{\beta}B}\right\} &= 2\,\delta^A_B\,(\sigma^\mu)_{\alpha\dot{\beta}}\,P_\mu\,, \\
\left\{Q_\alpha{}^A, Q_\beta{}^B\right\} &= \left\{\bar{Q}_{\dot{\alpha}A}, \bar{Q}_{\dot{\beta}B}\right\} = 0\,, \\
\left[P_\mu, Q_\alpha{}^A\right] &= \left[P_\mu, \bar{Q}_{\dot{\alpha}A}\right] = 0\,, \\
\left[M_{\mu\nu}, Q_\alpha{}^A\right] &= \frac{1}{2}\,(\sigma_{\mu\nu})_\alpha{}^\beta\,Q_\beta{}^A\,, \\
\left[M_{\mu\nu}, \bar{Q}^{\dot{\alpha}}{}_A\right] &= \frac{1}{2}\,(\bar{\sigma}_{\mu\nu})^{\dot{\alpha}}{}_{\dot{\beta}}\,\bar{Q}^{\dot{\beta}}{}_A\,.
\end{aligned}
\tag{3.1}
$$

The supersymmetry generators Q and $\bar{Q}$ of Eq. (3.1) are two-component Weyl spinor operators with spinor indices α, $\dot{\alpha}$, β, $\dot{\beta}$, running from 1 to 2. The undotted indices transform under the $(0, \frac{1}{2})$-representation of the Poincaré group whereas the dotted ones under the conjugated $(\frac{1}{2}, 0)$-representation. The indices A, B are related to the internal space and run from 1 to its dimension N. P_μ and $M_{\mu\nu}$ are the generators of the Poincaré group with Lorentz indices μ, ν running from 0 to 3. The elements of the Pauli

matrices σ^μ, $\sigma_{\mu\nu}$ and $\bar\sigma_{\mu\nu}$ appear as structure constants of the supersymmetric algebra. Theories with extended supersymmetry, i.e. with $N > 1$, do not have phenomenological prospects [26]. This is due to the fact that within four-dimensional field theories the extended supersymmetry does not allow for chiral fermions and parity violation as it is observed in the SM. Therefore only phenomenologically viable supersymmetric theories with $N = 1$ will be considered in the following.

The first anticommutator relation of Eq. (3.1) indicates the entanglement of supersymmetry and space-time symmetry. This provides a framework for the unification of particle physics and gravity. Since the general theory of relativity is invariant under the local Poincaré symmetry, imposing a local supersymmetry naturally incorporates the algebra of general relativity and thus gravity into the theory [6, 26].

Beside the original motivation for supersymmetry it was found later on that supersymmetric theories provide a natural solution to the hierarchy problem [27–29], allow for the unification of gauge couplings [20, 27] and furthermore, supply a candidate for the dark matter [30]. These are the biggest achievements of the supersymmetry from the phenomenological point of view.

3.2   Properties of supersymmetric theories

Under the action of the supersymmetric operator Q a bosonic state is transformed into a fermionic state and vice-versa:

$$Q|\text{boson}\rangle = |\text{fermion}\rangle\,, \qquad\qquad \text{Q}|\text{fermion}\rangle = |\text{boson}\rangle. \qquad (3.2)$$

In this way supersymmetry links fermionic and bosonic degrees of freedom. Fermions and bosons which transform into each other are called superpartners and they occur in supermultiplets. Each supermultiplet contains the same number of fermionic and bosonic degrees of freedom. As follows from Eq. (3.1),

$$\left[P^2, Q_\alpha\right] \;=\; \left[P^2, \bar Q_{\dot\alpha}\right] \;=\; 0\,, \qquad (3.3)$$

all states within a multiplet have the same mass. Furthermore, the supersymmetry generators also commute with the generators of gauge transformations. Therefore particles within the same multiplet must also be in the same representation of the gauge group and have the same quantum numbers of electric charge, weak isospin and color degrees of freedom.

There are two types of supermultiplets which are of special importance for the construction of supersymmetric Langrangians. One of them is called scalar or chiral
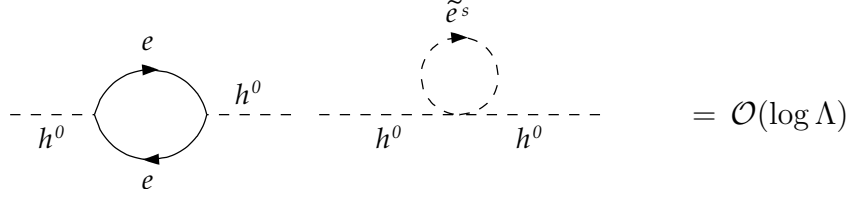
Figure 3.1: Quantum corrections to the self-energy of the Higgs boson from the electron and its superpartners, the selectrons, $(s = 1, 2)$. Quadratic divergences are no longer present and the total contribution depends only on the logarithm of the cut-off Λ.

supermultiplet, the other is refered to as gauge or vector supermultiplet. The particle content of the chiral supermultiplet consists of a Weyl fermion with two helicity states. These correspond to two degrees of freedom and of two real scalars, each with one degree of freedom. The two real scalars can be combined into one complex scalar field. The vector multiplet is composed of a massless spin-1 vector boson with two degrees of freedom. As a superpartner a massless spin-$\frac{1}{2}$ Weyl fermion is introduced.

It is possible to construct a single object composed of fermionic and bosonic fields of the corresponding supermultiplet, a superfield. Superfields are of particular convenience for the construction of supersymmetric Lagrangians. Basic notations and conventions of the superfield formalism and of the construction of supersymmetric Lagrangians in general are listed in appendix B. Detailed introductions can be found e.g. in [7,31].

As a consequence of the fact that supersymmetry links fermionic and bosonic degrees of freedom, it can provide a solution to the hierarchy problem [7,27–29] as already mentioned in the previous section. Since fermion and boson loops appear with opposite signs, quadratic divergences in radiative corrections to the self-energy of the Higgs field are fully compensated by contributions of the superpartners. As an example, the radiative correction to the Higgs self-energy corresponding to the electron, compensated by the superpartner contribution, is shown in Fig. 3.1. Unbroken supersymmetry guarantees this cancellation to all orders of perturbation theory.

3.2.1 Supersymmetry breaking

If supersymmetry were an exact symmetry of nature then particles and their superpartners would have the same mass. Since no superpartners have been observed yet, supersymmetry must be broken at energies accessible to present experiments. In analogy to the spontaneous electroweak symmetry breaking in the SM, spontaneous breaking of the supersymmetry can be introduced. This means that the Lagrangian remains invariant under the supersymmetry transformations, but it receives a vacuum state
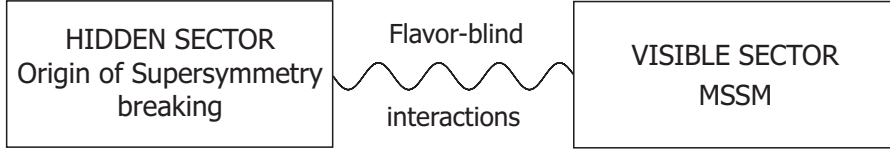
Figure 3.2: Schematic structure of supersymmetry breaking. The breaking takes place in a hidden sector from which it is transferred to a visible sector that can be accessed by experiments, e.g. the Minimal Supersymmetric Standard Model (MSSM) (see Sec. 3.3). The transition is mediated by some weak flavor-blind interaction specific for a given supersymmetry breaking scenario.

which is not invariant [32, 33].

Many models of spontaneous supersymmetry breaking have been proposed. Typically the breaking takes place at very high energies in a so-called "hidden" sector and thereafter it is transmitted to a visible sector which can be accessed by experiments. The transition is mediated by some kind of very weak interaction as shown in Fig. 3.2. Two popular candidates are gravity-mediated [34–36] and gauge-mediated [37, 38] supersymmetry breaking models.

At low energies the spontaneous breaking of supersymmetry is however, phenomenologically excluded [39]. Therefore it is replaced by the "soft" supersymmetry breaking which is a simple approach of how to include explicit symmetry breaking terms into the Lagrangian. These terms are strongly constrained by the request of preserving the solution to the hierarchy problem. Hence, they might not hinder a cancellation of quadratic divergences in the radiative corrections to the Higgs self-energy. All possible soft-breaking terms are elucidated in [40]. In the end, the Lagrangian consists of a supersymmetric part and of a soft part which is not invariant under the supersymmetry transformations,

$$\mathcal{L} = \mathcal{L}_{\text{SUSY}} + \mathcal{L}_{\text{soft}} \ . \tag{3.4}$$

3.2.2 R-parity

Within the Standard Model (SM) baryon and lepton number are implicitly conserved. This is based on the fact that no violating effects have ever been observed (the experimental limit on the proton life-time which supports the conservation has already been mentioned in section 2.2). Many other processes also give significant constraints on the violation of baryon and lepton number. These are reviewed e.g. in [41].

Nevertheless, there is no symmetry in the SM which would forbid the violation of baryon and/or lepton number. Postulating such conservation as a fundamental

principle of nature is generally not viable. This is caused by non-perturbative effects
in the electroweak sector which do violate baryon and lepton number, although these
effects are negligible for energy ranges of current high energy experiments.

The situation is different in supersymmetric theories. Here it is possible to impose
a symmetry which naturally conserves these quantum numbers and at the same time
does not contradict the non-perturbative baryon and lepton number violating effects.
This type of symmetry is given by *R-parity* [42]. A new quantum number R is intro-
duced from which R-parity is derived as $P_R = (-1)^R$. R-parity is not affected by the
supersymmetry breaking and is multiplicatively conserved. All SM particles including
all of Higgs scalars have $R = 0$, while $R = 1$ for all supersymmetric partners. The
link to baryon and lepton number conservation becomes obvious when the R-parity is
rewritten as a function of the baryon number B, lepton number L, and spin s,

$$P_R = (-1)^{2s+3(B-L)} .$$
(3.5)

Due to the R-parity conservation each interaction vertex connects even numbers of
supersymmetric particles. This means that they can be produced only in pairs and
furthermore, the lightest supersymmetric particle (LSP) is stable, which makes it a
popular candidate for dark matter.

3.2.3   Low-energy supersymmetry

Low-energy supersymmetry has been motivated by a natural explanation of the gauge
hierarchy problem which demands new physics at the TeV scale [28, 29]. This is of
particular interest for collider experiments. In addition, low-energy supersymmetric
models with R-parity conservation provide a suitable candidate for the dark matter [30]
and furthermore allow for the unification of gauge couplings at some large scale. The
latter is illustrated for the Minimal Supersymmetric Standard Model (MSSM) [6,7] in
Fig. 3.3. More details on MSSM will be presented in the next sections.

Experimental searches for supersymmetry [44] have been performed at LEP and
Tevatron experiments. Both have determined lower bounds on the masses of super-
symmetric particles. These limits strongly depend on the underlying mechanism of
supersymmetry breaking. For a recent review of the minimal supergravity (mSUGRA)
parameter space see [45]. Indirect constraints on the SUSY parameters arise from the
electroweak precision data. In general, the supersymmetric effects enter through higher
order corrections.

So far, there is no experimental evidence for supersymmetry. This is, however,
expected to change at the Large Hadron Collider (LHC). The LHC as a hadron collider
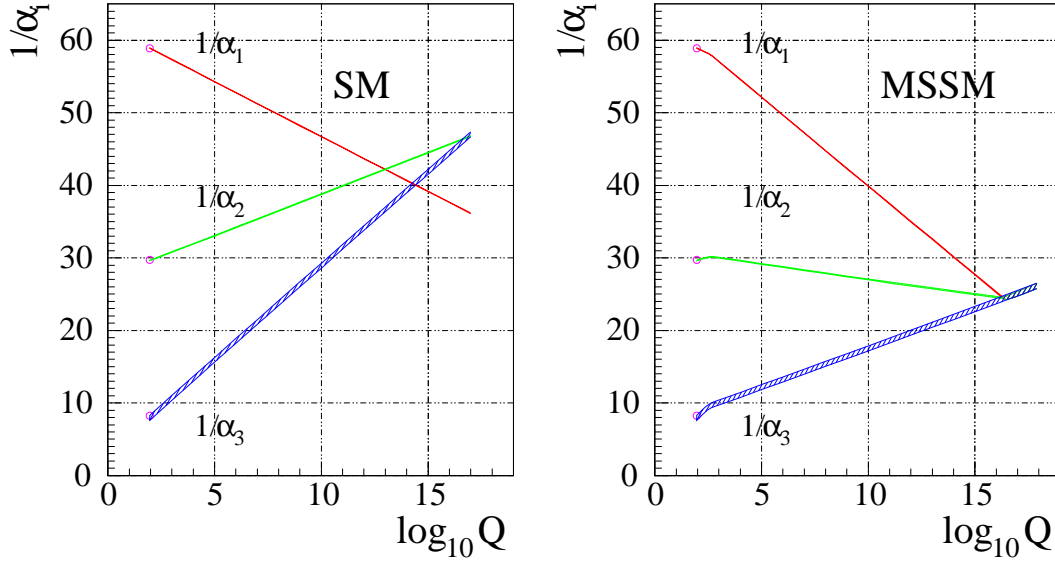
Figure 3.3: Evolution of the inverse of the three coupling constants in the Standard Model (left) and in the supersymmetric extension of the SM (MSSM) (right) [43]. Only in the latter case unification is obtained. The SUSY particles are assumed to contribute only above the effective SUSY scale MSUSY of about 1 TeV, which causes a change in the slope in the evolution of couplings. The thickness of the lines represents the error in the coupling constants.

with a center-of-mass energy of 14 TeV will serve as a discovery tool in most of the supersymmetric scenarios [44]. The only restriction is due to the mere existence of low-energy supersymmetry at the TeV scale.

The discovery potential of the LHC is of no doubt. Nevertheless, the concept of hadron colliders does not allow for high precision measurements. In this context more is expected from the International Linear Collider (ILC) project [46]. Such a linear e^+e^- collider provides much cleaner enviroment with lower background than a hadron machine.

As an exciting option, a collaboration of LHC and ILC has been proposed. The interplay between the ILC and the LHC during concurrent running of the two machines has the potential to maximise the physics gain from both facilities [47, 48].

It is also interesting to mention that there are models which consider the natural explanation of the gauge hierarchy problem to be "unnatural" [49]. In this sense, the effective supersymmetric theory at the TeV scale does not seem to be justified. Still, there are so called split-SUSY models [50] which propose that some fraction of the supersymmetric spectrum remains light enough (near the TeV scale) to provide successful gauge coupling unification and a viable candidate for the dark matter.

Taking into account all discovery options for low-energy supersymmetry leads to conclusion that any experimental evidence for supersymmetry would have a profound effect on the development of a more fundamental theory of particle physics than is currently available.

3.3 The Minimal Supersymmetric Standard Model

The Minimal Supersymmetric Standard Model (MSSM) is the simplest supersymmetric extension of the Standard Model (SM) [6, 7]. In analogy with the SM, the Lagrangian of MSSM is invariant under the local gauge symmetry of $SU(3)_C \times SU(2)_L \times U(1)_Y$. In addition, an $N=1$-supersymmetry with at most soft-breaking terms is imposed. The SM fields are incorporated into the MSSM via chiral and vector superfields. For each matter field there is a corresponding chiral superfield; vector superfields are assigned to gauge bosons. An octet of vector superfields is introduced for the $SU(3)_C$ gauge group, a triplet of vector superfields for the $SU(2)_L$ and a single vector field for the $U(1)_Y$ gauge group. As a result all SM particles gain superpartners: sfermions are scalar partners of the fermions and gauginos are fermionic partners of the gauge bosons.

Furthermore, R-parity P_R conservation is included into the MSSM Lagrangian. For all SM particles $P_R = +1$, for all superpartners $P_R = -1$. As a consequence, the lightest supersymmetric particle of the MSSM is stable and the leptonic and baryonic quantum number conservation is preserved.

In the Higgs sector, the single SM Higgs field must be replaced by two Higgs-doublets. Each belongs to a chiral superfield. There are several reasons why a single Higgs-doublet is not sufficient. In the first place, a hermitian conjugate corresponding to an antichiral superfield would be necessary to generate mass terms of both up- and down-like quarks and charged leptons. This would destroy invariance of the MSSM Lagrangian under the supersymmetry transformations. Therefore, the Lagrangian can only consist of chiral superfields. Moreover, two Higgs-doublets with opposite values of hypercharge are required to keep the MSSM free of anomalies. If the sum of hyper-charges of all fermions within the theory equals zero, all anomaly-contributions vanish. In this way anomalies related to the fermionic partners within the two Higgs-doublets are exactly canceled if these have opposite values of hypercharge.

The particle content of the MSSM is summarized in Tab. 3.1. For simplicity only the first generation of fermions is explicitely listed.

The Lagrangian of the MSSM consists of kinetic terms, mass terms and interaction terms for all fermions, Higgs- and gauge-bosons of the MSSM. It can be decomposed

Table 3.1: Classification of superfields and particles within the MSSM. The superfields are denoted with a hat, the superpartners carry a tilde. The generation index I runs from 1 to 3, the $SU(3)_C$ index a runs from 1 to 8, the $SU(2)_L$ index i from 1 to 3. Bold numbers in the group representation indicate the dimension of representation, **1** stands for the trivial representation, while *adj* refers to the adjoint representation of the corresponding group to which the gauge bosons belong. In case of the $U(1)_Y$ group, values of the hypercharge are explicitely given.

		fields		group representation		
	superfield	fermion field	boson field	$SU(3)_C$	$SU(2)_L$	$U(1)_Y$
matter sector						
quarks	$\hat{Q}_I$	$\begin{pmatrix} u_{L,I} \\ d_{L,I} \end{pmatrix}$	$\begin{pmatrix} \tilde{u}_{L,I} \\ \tilde{d}_{L,I} \end{pmatrix}$	**3**	**2**	$\frac{1}{3}$
squarks	$\hat{U}_I$	$u^c_{R,I}$	$\tilde{u}^+_{R,I}$	$\mathbf{3}^*$	**1**	$-\frac{4}{3}$
	$\hat{D}_I$	$d^c_{R,I}$	$\tilde{d}^+_{R,I}$	$\mathbf{3}^*$	**1**	$\frac{2}{3}$
leptons	$\hat{L}_I$	$\begin{pmatrix} \nu_{L,I} \\ e_{L,I} \end{pmatrix}$	$\begin{pmatrix} \tilde{\nu}_{L,I} \\ \tilde{e}_{L,I} \end{pmatrix}$	**1**	**2**	-1
sleptons	$\hat{E}_I$	$e^c_{R,I}$	$\tilde{e}^+_{R,I}$	**1**	**1**	2
gauge sector						
$SU(3)_C$	$\hat{G}^a$	$\tilde{\lambda}^a_G$	G^a_μ	$\mathbf{8}^{adj}$	**1**	0
$SU(2)_L$	$\hat{W}^i$	$\tilde{\lambda}^i_W$	W^i_μ	**1**	$\mathbf{3}^{adj}$	0
$U(1)_Y$	$\hat{B}$	$\tilde{\lambda}_B$	B_μ	**1**	**1**	0
Higgs sector						
	$\hat{H}_1$	$\begin{pmatrix} \tilde{H}^1_1 \\ \tilde{H}^2_1 \end{pmatrix}$	$\begin{pmatrix} H^1_1 \\ H^2_1 \end{pmatrix}$	**1**	**2**	-1
	$\hat{H}_2$	$\begin{pmatrix} \tilde{H}^1_2 \\ \tilde{H}^2_2 \end{pmatrix}$	$\begin{pmatrix} H^1_2 \\ H^2_2 \end{pmatrix}$	**1**	**2**	1

into

(i) a chiral part, the superpotential which describes interactions of the Higgs fields,

$$\mathcal{L}_{\text{chiral}} = \left(\epsilon^{ij} \left[\lambda_d \hat{H}^i_1 \hat{Q}^j \hat{D} - \lambda_u \hat{H}^i_2 \hat{Q}^j \hat{U} + \lambda_e \hat{H}^i_1 \hat{L}^j \hat{E} - \mu \hat{H}^i_1 \hat{H}^j_2 \right]\Big|_{\theta\theta} + \text{h.c.} \right), \tag{3.6}$$

with Yukawa couplings $\lambda_d, \lambda_u, \lambda_e$ and Higgs mass parameter μ, (for explanation of notations and conventions see appendix B)

(ii) a vector part which contains the kinetic terms of fermions as well as the interaction terms of scalar-, spinor- and vector-fields:

$$
\begin{aligned}
\mathcal{L}_{\text{vector,1}} &= \big[\hat{\bar{Q}} \, e^{2g'V'+2gV+2g_sV_s} \hat{Q} + \hat{\bar{U}} \, e^{2g'V'-2g_sV_s^T} \hat{U} + \hat{\bar{D}} \, e^{2g'V'-2g_sV_s^T} \hat{D} \\
&\quad + \hat{\bar{L}} \, e^{2g'V'+2gV} \hat{L} + \hat{\bar{E}} \, e^{2g'V'} \hat{E} \\
&\quad + \hat{\bar{H}}_1 \, e^{2g'V'+2gV} \hat{H}_1 + \hat{\bar{H}}_2 \, e^{2g'V'+2gV} \hat{H}_2 \, \big]\Big|_{\theta\theta\bar{\theta}\bar{\theta}} \, .
\end{aligned}
\tag{3.7}
$$

Here the following notation has been used:

$$
V_s = T_s^a V_s^a \, , \qquad V = T^a V^a \, , \qquad V' = \frac{Y}{2} v' \, ,
\tag{3.8}
$$

where T_s^a are the generators of $SU(3)_C$, T^a are the generators of $SU(2)_L$ and Y is the generator of $U(1)_Y$.

Furthermore, the vector part also consists of the kinetic terms of gauge bosons,

$$
\mathcal{L}_{\text{vector,2}} = \left(\left[\frac{1}{16g^2} W^{a\alpha} W_\alpha^a + \frac{1}{16g'^2} W'^\alpha W'_\alpha + \frac{1}{16g_s^2} W_s^{a\alpha} W_{s\alpha}^a \right]\Big|_{\theta\theta} + \text{h.c.} \right)
\tag{3.9}
$$

with $W_{s\alpha}^a$, W_α^a and W'_α being the field-strength tensors related to the vector-fields as shown in the following,

$$
W_{s\alpha}^a = -\frac{1}{4} \bar{D}\bar{D} \left(e^{-2g_sV_s} D_\alpha \, e^{2g_sV_s} \right) \, ,
\tag{3.10}
$$

$$
W_\alpha^a = -\frac{1}{4} \bar{D}\bar{D} \left(e^{-2gV} D_\alpha \, e^{2gV} \right) \, ,
\tag{3.11}
$$

$$
W'_\alpha = -\frac{1}{4} \bar{D}\bar{D} \left(e^{-2g'V'} D_\alpha \, e^{2g'V'} \right) = -\frac{g'}{4} \bar{D}\bar{D} D_\alpha V' \, .
\tag{3.12}
$$

The supersymmetric part of the MSSM Lagrangian can be summarized as follows,

$$
\mathcal{L}_{\text{SUSY}} = \mathcal{L}_{\text{chiral}} + \mathcal{L}_{\text{vector,1}} + \mathcal{L}_{\text{vector,2}} \, .
\tag{3.13}
$$

Supersymmetry breaking in the MSSM is realized explicitly via the soft breaking mechanism. This prevents quadratic divergences to affect the higher order corrections. Restrictions on the soft breaking Lagrangian are given in [40]. If only the first generation of fermions is taken into account, the soft part of MSSM Lagrangian can be written as

$$
\begin{aligned}
\mathcal{L}_{\text{soft}} &= - M_{L_{\tilde{q}}}^2 \left(\tilde{u}_L^+ \tilde{u}_L + \tilde{d}_L^+ \tilde{d}_L \right) - M_{\tilde{u}_R}^2 \tilde{u}_L^+ \tilde{u}_L - M_{\tilde{d}_R}^2 \tilde{d}_L^+ \tilde{d}_R \\
&\quad - M_{L_{\tilde{l}}}^2 \left(\tilde{\nu}_L^+ \tilde{\nu}_L + \tilde{e}_L^+ \tilde{e}_L \right) - M_{\tilde{e}_R}^2 \tilde{e}_L^+ \tilde{e}_R \\
&\quad - m_1^2 H_1^+ H_1 - m_2^2 H_2^+ H_2 + \left(m_3^2 \epsilon^{ij} H_1^i H_2^j + \text{h.c.} \right) \\
&\quad - \epsilon^{ij} \left(-\lambda_u A_u H_2^i \tilde{Q}^j \tilde{U} + \lambda_d A_d H_1^i \tilde{Q}^j \tilde{D} + \lambda_e A_e H_1^i \tilde{L}^j \tilde{E} + \text{h.c.} \right) \\
&\quad + \frac{1}{2} \left(M_1 \lambda_B \lambda_B + M_2 \lambda_W^a \lambda_W^a + M_3 \lambda_s^a \lambda_s^a + \text{h.c.} \right) \, .
\end{aligned}
\tag{3.14}
$$

Here λ_u, λ_d, λ_e, A_u, A_d, and A_e denote Yukawa and trilinear couplings which are in general complex 3×3 matrices in family space. The scalar mass parameters $M^2_{L_{\tilde{q}}}$, $M^2_{L_{\tilde{l}}}$, $M^2_{\tilde{u}_R}$, $M^2_{\tilde{d}_R}$ and $M^2_{\tilde{e}_R}$ are hermitian 3×3 matrices. They allow for mixing among the generations. The Higgs mass parameters m_1 and m_2 are real numbers whereas the gaugino mass parameters M_1, M_2 and M_3, as well as the bilinear Higgs coupling m_3, are complex numbers.

In complete analogy with the SM it is necessary to include gauge-fixing and ghost terms for consistent quantization of the MSSM Lagrangian (see section 2.1). The gauge-fixing and ghost terms are selected in a way identical to the SM. Thus the full expression of MSSM Lagrangian reads

$$\mathcal{L}_{\mathrm{MSSM}} = \mathcal{L}_{\mathrm{SUSY}} + \mathcal{L}_{\mathrm{soft}} + \mathcal{L}_{\mathrm{gauge-fixing}} + \mathcal{L}_{\mathrm{ghost}} \ . \tag{3.15}$$

While the kinetic and the gauge part of the MSSM Lagrangian only depend on SM parameters, in the superpotential and mainly the soft breaking part, new supersymmetric parameters are introduced. An unconstrained model contains in total 105 new parameters [51]. This very large number of new parameters seems to introduce a tremendous arbitrariness into the theory.

In order to constrain these parameters, experimental limits coming from lepton number conservation, flavor-changing neutral currents and CP violation observations [52] are imposed. When assuming a given model for the origin of supersymmetry breaking, the number of free parameters can be reduced significantly. For example within the mSUGRA scenario of the MSSM, all parameters can be derived from only 5 fundamental parameters which exist at the SUSY-breaking scale, using renormalization group equations [26, 31].

3.4 Particle content of the MSSM

3.4.1 Quarks and Leptons

In order to reproduce the experimental results, quarks and leptons have the same properties within the MSSM as in the SM. Left- and right-handed fermions are described by Weyl spinors which can be combined into Dirac spinors

$$u_I = \begin{pmatrix} u_{L,I} \\ \bar{u}^c_{R,I} \end{pmatrix} \ , \quad d_I = \begin{pmatrix} d_{L,I} \\ \bar{d}^c_{R,I} \end{pmatrix} \ , \quad e_I = \begin{pmatrix} e_{L,I} \\ \bar{e}^c_{R,I} \end{pmatrix} \ , \quad \nu_I = \begin{pmatrix} \nu_{L,I} \\ 0 \end{pmatrix} \ , \quad (3.16)$$

where the index I runs over generations from 1 to 3. The down-type quarks d_I are not exact mass eigenstates. These are obtained by rotating the flavor eigenstates d_I as

described by the CKM-matrix in the same way as in SM,

$$d'_I = V^{IJ}_{\text{CKM}} d_J \, . \tag{3.17}$$

Regarding the quark and lepton sector, the origin of masses is the main difference between the SM and MSSM. Within the MSSM, quarks and leptons receive their masses via Yukawa terms in the superpotential (Eq. 3.6) as

$$m_u = \lambda_u v_2 \, , \qquad m_d = \lambda_d v_1 \, , \qquad m_e = \lambda_e v_1 \, , \tag{3.18}$$

which can be rewritten as expressions for the Yukawa couplings

$$\lambda_u = \frac{m_u e}{\sqrt{2} m_W s_\beta} \, , \qquad \lambda_d = \frac{m_d e}{\sqrt{2} m_W c_\beta} \, , \qquad \lambda_e = \frac{m_e e}{\sqrt{2} m_W c_\beta} \, . \tag{3.19}$$

Here e is the elementary charge, m_W is the mass of the W boson and s_β and c_β stand for $\sin\beta$ and $\cos\beta$, with β being the mixing angle defined as ratio of the two vacuum expectation values v_2, v_1 (see section 3.4.3).

3.4.2 Squarks and Sleptons

In principle, all particles with the same quantum numbers can mix with each other. As the $SU(2)_L \times U(1)_Y$ symmetry is broken, only the color quantum numbers, electric charge and in addition, R-parity have to match. However, completely arbitrary soft breaking terms would lead to a mixing of fermions of different generations. Such mixing creates additional contributions to flavor changing neutral currents (FCNC) within the model. Besides the contribution related to the CKM-matrix which is already present in the SM, experimental limits [5] also constrain additional FCNC-effects to be very small [52]. In addition, most popular SUSY-breaking scenarios implement flavor-blind interactions to mediate the breaking mechanism from hidden to visible sector (see section 3.2.1).

For these reasons the soft breaking mass and 3×3 trilinear coupling matrices are chosen to be purely diagonal. This allows for a decomposition of squark and electron-like slepton mass matrices into a 2×2 form. The mixing is constrained to appear only within the left- and right-handed fields of each generation. As a consequence, the mass matrices can be written as

$$M_{\tilde{f}} = \begin{pmatrix} M^{LL}_{\tilde{f}} + m_f^2 & m_f \left(M^{LR}_{\tilde{f}} \right)^* \\ m_f \left(M^{LR}_{\tilde{f}} \right) & M^{RR}_{\tilde{f}} + m_f^2 \end{pmatrix} \tag{3.20}$$

with

$$M_{\tilde{f}}^{LL} = m_Z^2 \left(I_3^f - Q_f s_W^2 \right) c_{2\beta} + \begin{cases} M_{\tilde{Q}}^2 & \text{for left-handed squarks} \\ M_{\tilde{L}}^2 & \text{for left-handed sleptons} \end{cases} \qquad (3.21)$$

$$M_{\tilde{f}}^{RR} = m_Z^2 \left(Q_f s_W^2 \right) c_{2\beta} + \begin{cases} M_{\tilde{U}}^2 & \text{for right-handed up-like squarks} \\ M_{\tilde{D}}^2 & \text{for right-handed down-like squarks} \\ M_{\tilde{R}}^2 & \text{for right-handed electron-like sleptons} \end{cases}$$
$$(3.22)$$

$$M_{\tilde{f}}^{LR} = A_f - \mu^* \begin{cases} \cot\beta & \text{for up-like squarks} \\ \tan\beta & \text{for down-like squarks and electron-like sleptons} \end{cases}$$
$$(3.23)$$

Here Q_f is the fraction of electric charge of the sfermion, I_3^f is the third component of weak isospin, and m_Z the mass of the Z boson. Similarly to the previous section short-hand notations for sin and cos are used, with the mixing angle β defined as ratio of the two VEVs. $s_W = 1 - \frac{m_W^2}{m_Z^2}$ denotes sin of the Weinberg angle, μ is the Higgs mass parameter and A_f is the trilinear coupling.

Subsequently, the mass matrices can be diagonalized by unitary matrices $U_{\tilde{f}}$,

$$\mathcal{D}_{\tilde{f}} = U_{\tilde{f}} M_{\tilde{f}} U_{\tilde{f}}^\dagger = \begin{pmatrix} m_{\tilde{f}_1}^2 & 0 \\ 0 & m_{\tilde{f}_2}^2 \end{pmatrix} , \qquad (3.24)$$

to give mass eigenstates $\tilde{f}_1$ and $\tilde{f}_2$ which transform as

$$\begin{pmatrix} \tilde{f}_1 \\ \tilde{f}_2 \end{pmatrix} = U_{\tilde{f}} \begin{pmatrix} \tilde{f}_L \\ \tilde{f}_R \end{pmatrix} . \qquad (3.25)$$

In the sneutrino sector only the left-handed fields exist. For this reason interaction and mass eigenstates are identical.

From Eqs. (3.20–3.23) it is possible to deduce that the first- and second-family squarks and sleptons appear in almost unmixed pairs owing to their negligible Yukawa couplings. The mixing becomes significant only in the case of third generation.

3.4.3 Higgs and Gauge bosons

As previously mentioned, the Higgs sector of MSSM must consist of two scalar isospin doublets with opposite values of hypercharge

$$H_1 = \begin{pmatrix} v_1 + \frac{1}{\sqrt{2}}(\phi_1^0 - i\chi_1^0) \\ -\phi_1^- \end{pmatrix} , \qquad H_2 = \begin{pmatrix} -\phi_2^+ \\ v_2 + \frac{1}{\sqrt{2}}(\phi_2^0 - i\chi_2^0) \end{pmatrix} , \qquad (3.26)$$

where ϕ_1^0, ϕ_2^0, χ_1^0, χ_2^0 are real scalar fields and ϕ_1^-, $-\phi_2^+$ are complex scalar fields. Also, the expansion around the two corresponding vacuum expectation values v_1 and v_2 has been performed here.

Inserting (3.26) into the Higgs part of the MSSM Lagrangian leads to three uncoupled real 2×2 mass matrices for the Higgs fields. Mass eigenstates are obtained by a diagonalization procedure, which is in case of real 2×2 matrices simply a rotation,

$$
\begin{pmatrix} G^\pm \\ H^\pm \end{pmatrix} = \begin{pmatrix} c_\beta & s_\beta \\ -s_\beta & c_\beta \end{pmatrix} \begin{pmatrix} \phi_1^\pm \\ \phi_2^\pm \end{pmatrix} ,
$$
$$
\begin{pmatrix} G^0 \\ A^0 \end{pmatrix} = \begin{pmatrix} c_\beta & s_\beta \\ -s_\beta & c_\beta \end{pmatrix} \begin{pmatrix} \chi_1^0 \\ \chi_2^0 \end{pmatrix} ,
$$
$$
\begin{pmatrix} H^0 \\ h^0 \end{pmatrix} = \begin{pmatrix} c_\alpha & s_\alpha \\ -s_\alpha & c_\alpha \end{pmatrix} \begin{pmatrix} \phi_1^0 \\ \phi_2^0 \end{pmatrix} ,
\tag{3.27}
$$

where s_β, c_β, s_α, c_α are the short-hand notations used before for sin and cos. The mixing angle β is defined as ratio of the two VEVs

$$
\tan\beta = \frac{v_2}{v_1} \qquad \text{with} \qquad 0 < \beta < \frac{\pi}{2} .
\tag{3.28}
$$

Within the MSSM $\tan\beta$ acts as a free parameter. The mixing angle α is fixed by the relation

$$
\tan 2\alpha = \tan 2\beta \, \frac{m_A^2 + m_Z^2}{m_A^2 - m_Z^2} \qquad \text{with} \qquad -\frac{\pi}{2} < \alpha < 0 \quad .
\tag{3.29}
$$

Nevertheless, the choice of α within the allowed interval is not unique. By convention α is set such that $m_{h^0} < m_{H^0}$.

The Higgs sector consists of three Goldstone bosons $G^\pm$, G^0 which emerge from the electroweak symmetry breaking. The five remaining Higgs bosons are physical. There are two neutral CP-even bosons h^0 and H^0, one neutral CP-odd A^0 and two charged bosons $H^\pm$. By convention, the mass of the CP-odd Higgs boson m_A is chosen to be the second free parameter within the MSSM Higgs sector.

At the tree-level the Higgs boson masses can be parametrized in terms of m_A and $\tan\beta$ as follows,

$$
\begin{aligned}
m_{h^0,H^0} &= \frac{1}{2}\left(m_A^2 + m_Z^2 \mp \sqrt{(m_A^2 + m_Z^2)^2 - 4 m_A^2 m_Z^2 c_{2\beta}^2} \right) , \\
m_{H^\pm} &= m_A^2 + m_W^2 ,
\end{aligned}
\tag{3.30}
$$

with m_Z, m_W being the masses of the Z and W bosons which appear along with the photon as mass eigenstates of the $SU(2)_L \times U(1)_Y$ after the electroweak symmetry breaking. In complete analogy with the SM (see section 2.1), W and Z acquire masses

related to the vacuum expectation value v which is now given as $v = \sqrt{v_1^2 + v_2^2}$. Regarding the $SU(3)_C$ gauge group, there are eight massless gauge bosons, the gluons, with the same properties as in the SM.

The tree-level Higgs masses receive large contributions from radiative corrections. These have to be taken into account in order to obtain realistic predictions. At the one-loop level, the full set of radiative corrections have been computed [53–56]. Dominant two-loop contributions of the order of $\mathcal{O}(\alpha_t \alpha_s)$ [57–61], $\mathcal{O}(\alpha_t^2)$ [57, 62, 63], $\mathcal{O}(\alpha_b \alpha_s)$ [64, 65] and $\mathcal{O}(\alpha_t \alpha_b + \alpha_b^2)$ [66] have been calculated using the Feynman diagrammatic approach [67]. Values of the Higgs masses as given in [68] are used for numerical evaluations in the thesis.

3.4.4 Higgsinos and Gauginos

Similar to the sfermion sector, superpartners of gauge and Higgs bosons which possess identical quantum numbers mix with each other. In the non-colored charged sector there are two candidate pairs which can be composed of alike charged winos $\tilde{W}^\pm$ and Higgsinos $\tilde{H}^\pm$,

$$
\tilde{W}^\pm = \begin{pmatrix} -i\tilde{\lambda}_W^\pm \\ i\tilde{\bar{\lambda}}_W^\mp \end{pmatrix} , \qquad
\tilde{H}^+ = \begin{pmatrix} \tilde{H}_2^1 \\ \tilde{\bar{H}}_1^2 \end{pmatrix} , \qquad
\tilde{H}^- = \begin{pmatrix} \tilde{H}_1^2 \\ \tilde{\bar{H}}_2^1 \end{pmatrix} , \tag{3.31}
$$

with analogous relation as for the W bosons,

$$
\tilde{\lambda}_W^\pm = \frac{1}{\sqrt{2}} \left(\tilde{\lambda}_W^1 \mp i\tilde{\lambda}_W^2 \right) . \tag{3.32}
$$

These four two-component Weyl spinors can be combined into two four-component Dirac fermions $\tilde{\chi}_1^+$, $\tilde{\chi}_2^+$, called charginos. The mass matrix can be diagonalized by two unitary matrices U, V:

$$
U^* \begin{pmatrix} M_2 & \sqrt{2}m_W s_\beta \\ \sqrt{2}m_W c_\beta & \mu \end{pmatrix} V^\dagger = \begin{pmatrix} m_{\tilde{\chi}_1^+} & 0 \\ 0 & m_{\tilde{\chi}_2^+} \end{pmatrix} , \tag{3.33}
$$

such that $m_{\tilde{\chi}_{1,2}^+}$ are both positive and $m_{\tilde{\chi}_1^+} \leq m_{\tilde{\chi}_2^+}$. Subsequently, mass eigenstates of the charginos are given by

$$
\tilde{\chi}_i^+ = \begin{pmatrix} V \begin{pmatrix} -i\tilde{\lambda}_W^+ \\ \tilde{H}_2^1 \end{pmatrix} \\ U \begin{pmatrix} -i\tilde{\lambda}_W^- \\ \tilde{H}_1^2 \end{pmatrix} \end{pmatrix} , \qquad \mathrm{i} = 1 , 2 \quad . \tag{3.34}
$$

Also the uncolored neutral gauginos and higgsinos mix with each other. There are two neutral higgsinos $\tilde{H}_1^0$, $\tilde{H}_2^0$, zino $\tilde{Z}$ and photino $\tilde{A}$ available.

$$\tilde{H}_1^0 = \begin{pmatrix} \tilde{H}_1^1 \\ \bar{\tilde{H}}_1^1 \end{pmatrix} , \quad \tilde{H}_2^0 = \begin{pmatrix} \tilde{H}_2^2 \\ \bar{\tilde{H}}_2^2 \end{pmatrix} , \quad \tilde{Z} = \begin{pmatrix} -i\tilde{\lambda}_Z \\ i\bar{\tilde{\lambda}}_Z \end{pmatrix} , \quad \tilde{A} = \begin{pmatrix} -i\tilde{\lambda}_A \\ i\bar{\tilde{\lambda}}_A \end{pmatrix} . \tag{3.35}$$

In complete analogy with the SM case of Z and γ, the latter two are obtained by rotating $\tilde{\lambda}_W^3$ and $\tilde{\lambda}_B$ by the EW mixing angle,

$$\tilde{\lambda}_Z = c_W \tilde{\lambda}_W^3 - s_W \tilde{\lambda}_B , \qquad\qquad \tilde{\lambda}_A = s_W \tilde{\lambda}_W^3 + c_W \tilde{\lambda}_B . \tag{3.36}$$

In the end, there are four Weyl spinors at hand which can be transformed into four Majorana fermions, called neutralinos. Their mass matrix can be diagonalized by a unitary matrix N which obeys the order of increasing neutralino masses $m_{\tilde{\chi}_1^0} \leq m_{\tilde{\chi}_2^0} \leq m_{\tilde{\chi}_3^0} \leq m_{\tilde{\chi}_4^0}$,

$$N^* \begin{pmatrix} M_1 & 0 & -m_Z s_W c_\beta & m_Z s_W s_\beta \\ 0 & M_2 & m_Z c_W c_\beta & -m_Z c_W s_\beta \\ -m_Z s_W c_\beta & m_Z c_W c_\beta & 0 & -\mu \\ m_Z s_W s_\beta & -m_Z c_W s_\beta & -\mu & 0 \end{pmatrix} N^\dagger$$

$$= \begin{pmatrix} m_{\tilde{\chi}_1^0} & 0 & 0 & 0 \\ 0 & m_{\tilde{\chi}_2^0} & 0 & 0 \\ 0 & 0 & m_{\tilde{\chi}_3^0} & 0 \\ 0 & 0 & 0 & m_{\tilde{\chi}_4^0} \end{pmatrix} . \tag{3.37}$$

The neutralino mass eigenstates are given by:

$$\begin{pmatrix} \tilde{\chi}_1^0 \\ \tilde{\chi}_2^0 \\ \tilde{\chi}_3^0 \\ \tilde{\chi}_4^0 \end{pmatrix} = N \begin{pmatrix} -i\tilde{\lambda}_B \\ -i\tilde{\lambda}_W^3 \\ \tilde{H}_1^1 \\ \tilde{H}_2^2 \end{pmatrix} . \tag{3.38}$$

In the colored sector there are eight gauginos of $SU(3)_C$ called the gluinos. They are Majorana fermions with mass $m_{\tilde{g}} = |M_3|$ and can be written as

$$\tilde{g}^a = \begin{pmatrix} -i\tilde{\lambda}_G^a \\ i\bar{\tilde{\lambda}}_G^a \end{pmatrix} , \qquad a = 1, \dots, 8 \quad . \tag{3.39}$$

Chapter 4

Regularization and Renormalization

In general, the Lagrangian of a model contains free parameters which are not fixed by the theory but have to be determined in experiments. For this purpose, a renormalization scheme is selected in which the parameters are defined via their relations to measurable quantities. At tree-level, the Lagrangian parameters can be directly identified with physical observables like masses and coupling constants. However, these relations are modified by higher order contributions within perturbation theory.

Including radiative corrections does not only change the tree-level relations between free parameters and physical observables, it also leads to divergences in the loop integrals. For a consistent mathematical treatment it is necessary to regularize the divergences using a regularization procedure. This introduces a cut-off dependence into the relations between Lagrangian parameters and physical observables. Hence, the "bare" Lagrangian parameters cannot have any physical meaning. In order to restore the physical meaning they have to be replaced by the renormalized parameters. More details about regularization and renormalization procedures are described in the following sections.

4.1   Regularization

The integration over loop momenta leads to ultra-violet (UV) divergences. In order to obtain a UV finite result within a renormalization scheme, first of all, the divergences have to be controled by means of a regularization. A regularization parameter Λ is introduced into the theory that makes the loop integrals finite but Λ dependent. In this way the problem how to deal with divergent integrals is transformed into a task how to compensate for the dependence on the regularization parameter. In the end, the theoretical predictions have to be independent of such a parameter. Otherwise they would have no physical meaning.

Different regularization procedures are available. Few examples are described in the following:

(i) **Pauli-Villars Regularization**

The Pauli-Villars regularization [69] is based on a simple intuitive concept. To prevent the integral from reaching the UV divergent limit, the upper bound of the momentum integration is constrained by a cut-off parameter. Although this method is very illustrative, it violates gauge invariance and this constrains its applicability within the higher order calculations.

(ii) **Dimensional Regularization**

The dimensional regularization scheme [70] is a typical regularization procedure used within the SM. It is based on the fact that in four dimensional space-time the loop integrals are UV divergent. However, if the dimension of integration is shifted by an infinitesimal value ϵ to a new dimension $D = 4 - \epsilon$, the integrals become finite. In addition, a mass parameter μ is introduced to keep coupling constants dimensionless.

This scheme preserves gauge invariance but not the chiral symmetries such as supersymmetry. This is caused by the fact that additional degrees of freedom are introduced during the transition to D dimensions. As a consequence, the numbers of fermionic and bosonic degrees of freedom do not agree with each other anymore which results into a violation of supersymmetry.

(iii) **Dimensional Reduction**

The dimensional reduction scheme [71, 72] is a modification of the dimensional regularization suggested to avoid the supersymmetry violation. Unlike dimensional regularization, only the integrated momenta are expressed in D-dimensions whereas the fields are kept in four dimensions. A mathematically consistent formulation for this procedure has recently been established [73].

4.2   Renormalization

Unphysical parameters introduced into the theory via regularization have to be eliminated. This is taken care of by the renormalization. In general, the renormalization procedure consists of a set of rules which serve to restore, in a consistent way, the relations between parameters of the theory and physical observables.

Within the frequently used multiplicative renormalization, bare parameters of the Lagrangian g_0 are replaced by renormalized parameters g and renormalization constants

Z_g according to the relation

$$g_0 = Z_g g = \left(1 + \delta Z_g^{(1)} + \delta Z_g^{(2)} + \dots\right) g\,. \tag{4.1}$$

Here the renormalization constants Z_g have been expanded in perturbation series whose order is denoted by a superscript. The renormalized parameters g have finite values. The divergences which have been parametrized by means of regularization are absorbed into the renormalization constants Z_g.

In order to obtain finite S-matrix elements it is sufficient to perform renormalization for the Lagrangian parameters and for the wave functions of external particles. Nevertheless, to achieve a completely finite theoretical description, also all Green functions have to be finite. For this reason field renormalization has to be performed. Bare fields of the Lagrangian Φ_0 have to be replaced by renormalized fields Φ using renormalization constants Z_Φ,

$$\Phi_0 = \sqrt{Z_\Phi}\,\Phi = \left(1 + \frac{1}{2}\delta Z_\Phi^{(1)} - \frac{1}{8}\left(\delta Z_\Phi^{(1)}\right)^2 + \frac{1}{2}\delta Z_\Phi^{(2)} \dots\right)\Phi\,. \tag{4.2}$$

Again the renormalization constants Z_Φ are written as perturbation expansions

$$Z_\Phi = 1 + \delta Z_\Phi^{(1)} + \delta Z_\Phi^{(2)} + \dots \tag{4.3}$$

After insertion of the renormalized parameters and fields into the bare Lagrangian, this can be split into a renormalized part and a counter term part:

$$\mathcal{L}\left(g_0, \Phi_0\right) = \mathcal{L}\left(Z_g g, \sqrt{Z_\Phi}\,\Phi\right) = \mathcal{L}\left(g, \Phi\right) + \mathcal{L}_{\mathrm{CT}}\left(g, \Phi, \delta Z_g, \delta Z_\Phi\right)\,. \tag{4.4}$$

The renormalized Lagrangian is finite, free of unphysical regularization parameters and thus suitable for theoretical predictions. The counter term part can be expressed as perturbation series:

$$\begin{aligned}
\mathcal{L}_{\mathrm{CT}}\left(g, \Phi, Z_g, Z_\Phi\right) &= \mathcal{L}_{\mathrm{CT}}^{(1)}\left(g, \Phi, \delta Z_g^{(1)}, \delta Z_\Phi^{(1)}\right) + \\
&\quad \mathcal{L}_{\mathrm{CT}}^{(2)}\left(g, \Phi, \delta Z_g^{(1)}, \delta Z_\Phi^{(1)}, \delta Z_g^{(2)}, \delta Z_\Phi^{(2)}\right) + \dots
\end{aligned} \tag{4.5}$$

4.2.1   Renormalization schemes

The definition of all parameters of the theory and their connection to physical observables are fixed within a renormalization scheme. In an exact calculation to all orders in perturbation theory, the final result does not depend on the renormalization scheme. For practical purposes however, only contributions up to a given order are evaluated.

As a consequence, the result becomes dependent on the renormalization scheme, which reflects the theoretical uncertainty introduced by missing higher-order terms.

Consistent use of a renormalization scheme is one of the key issues within perturbative calculations. It requires an appropriate choice of input parameters since these are scheme dependent. Also the renormalization constants differ from one scheme to another. Altough divergent parts are the same within all schemes, finite contributions are scheme dependent.

(i) $\overline{\text{MS}}$ **renormalization scheme**

The minimal subtraction scheme, or short MS-scheme, [16] is the simplest renormalization scheme. It is based on the dimensional regularization procedure. Only the divergent terms in the higher order contributions are absorbed into the counter term part of Lagrangian, but no finite contributions. The mass parameter μ introduced by the regularization to keep couplings dimensionless is now transformed to a renormalization scale parameter μ_R. To specify a concrete renormalization scheme from large spectrum of MS-schemes, the scale μ_R must be fixed.

The $\overline{\text{MS}}$-scheme [74–76] is a modified minimal subtraction. It is a commonly used version of MS-scheme. It is based on a simple observation that the divergent terms parametrized as $1/\epsilon$ are always associated with certain constant terms. The whole set can be denoted as Δ^n, where n is the loop order. At the one-loop level, the explicit expression reads

$$\Delta = \frac{1}{\epsilon} - \gamma_E + \ln 4\pi \tag{4.6}$$

where γ_E is the Euler-Mascheroni constant. The $\overline{\text{MS}}$ scale is subsequently redefined as

$$\mu_R^{2^{\overline{\text{MS}}}} := \mu_R^2 e^{\ln 4\pi - \gamma_E} \tag{4.7}$$

(ii) $\overline{\text{DR}}$ **renormalization scheme**

The $\overline{\text{DR}}$-scheme is based on dimensional reduction. Apart from that it is identical with the $\overline{\text{MS}}$-scheme. As in the previous case, just the Δ^n terms are absorbed into the counter terms, but no finite contributions. The renormalization scale $\mu_R^{\overline{\text{DR}}}$ is redefined analogously to eq. (4.7).

At the one-loop level, the counter terms within both schemes are identical. Modifications are introduced at higher orders and are due to different finite contributions induced by the two regularizations.

(iii) **On-shell renormalization scheme**

Within the on-shell renormalization (OS) scheme [77, 78], the on-shell renormalization conditions are imposed. This means that particles are restricted to be on their mass-shell. The on-shell principle implies that the mass of a particle to be on-shell is given as real part of the pole of the propagator and in this way it can be directly interpreted as physical mass. To obey the on-shell conditions, not only divergent parts but also finite contributions are contained in the counter terms. Hence, all corrections to the real part of the pole of the propagator are absorbed into the mass counter terms.

If all variables are determined to be on-shell, the final result becomes totally independent on the renormalization scale μ. For the on-shell renormalization of coupling constants it is required that all loop-induced corrections to the particle coupling are absorbed into the counter terms for the coupling constant. The fields are determined to be on-shell by a consistent normalization, i.e. the residua of the propagators have to be equal to unity.

Complete expressions for the OS renormalization scheme within the SM at the one-loop level are given in [78]. The extension into the MSSM has been worked out by [79].

Chapter 5

Hadronic cross sections

Within the SM and MSSM, strong interactions of quarks and gluons are described by Quantum Chromodynamics (QCD) [3,4]. Unlike other fundamental interactions, they are based on the $SU(3)_C$ gauge group and consequently have the special properties of asymptotic freedom and confinement. Asymptotic freedom is a characteristic feature of short-distance interactions which keeps them very weak. This enables the quarks and gluons to behave almost like free particles. At large distances the situation is completely opposite. The interaction strenth rises with distance and binds the particles tightly together. The energy of interaction increases until it becomes sufficient for the creation of a new quark–antiquark pair. As a consequence, it is impossible to observe a single quark or gluon. This phenomenon is referred to as confinement.

Quarks and gluons can only be observed indirectly as constituents of color-neutral objects, called hadrons. It is evident that realistic theoretical predictions have to take this fact into account. However, due to the confinement, the perturbative approach can not be justified at the hadronic level. Therefore, it is necessary to establish a connection between the short-distance interactions of quarks and gluons which can be described by means of perturbation theory and the experimentally observable interactions of hadrons (e.g. [80]). The necessary link is provided by the parton model [81] and the factorization theorem [82] which will be discussed in the following.

5.1   Parton model

Unlike QCD, the parton model is based on many assumptions which have purely phenomenological origin. It was motivated by experimental results from deep inelastic electron–proton scattering (DIS) [83]. The most striking feature of the data is known as Bjorken scaling [84] and corresponds to approximate independence of the measured structure functions of the proton on the momentum transfer.
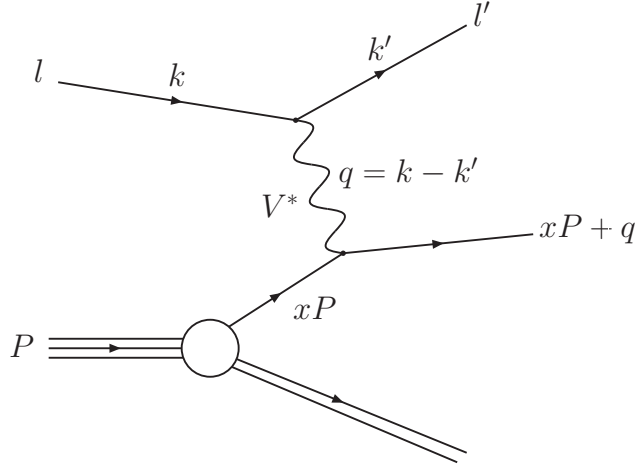
Figure 5.1: The schematic structure of deep inelastic lepton–hadron scattering at lead-
ing order. A single parton with fraction x of the hadron momentum P interacts with
the lepton via a hard process which can be computed in perturbation theory. The
non-perturbative effects within the hadron do not interfere because of Lorentz time
dilation.

The scaling can be explained if presuming that the hadron is composed of point-
like partons which interact with the electron. The process of electron–proton scattering
can then be approximated as an incoherent sum of elastic lepton–parton scatterings,
which can be described by perturbation theory. With help of QCD the partons can be
identified as quarks and gluons.

As shown in Fig. 5.1, any lepton–hadron DIS process can be regarded as a hard
scattering of the lepton on a parton within the hadron, whereas the non-perturbative
interactions of other partons in the hadron do not interfere. This assumption relies
on the effect of Lorentz time dilation. The time scales related to the movement of
the hadron and to the non-perturbative process of hadronization are much larger than
the time scale of the hard scattering. As a consequence, the hadron can be treated
as a static object during the hard scattering. Also the partons are effectively "frozen"
during the short time it takes the lepton to pass by. Multiple lepton–parton scattering
is strongly suppressed if assuming large momentum transfer. A single parton which
then participates in the hard scattering carries a momentum xP^μ given as a fraction
$x \in [0, 1]$ of the hadron momentum P^μ.

The same assumptions apply to interactions of hadrons. Two colliding hadrons
interact at the partonic level via a hard interaction of two partons which both carry
certain fractions of hadron momenta. The corresponding hadronic cross section can be

written as a convolution

$$\sigma_A(P_A, P_B) = \sum_{i,j} \int_0^1 \int_0^1 dx_a dx_b \, \hat{\sigma}_{i,j}^{(0)}(x_a P_A, x_b P_B) \, \Phi_{i|A}(x_a) \, \Phi_{j|B}(x_b) \,, \qquad (5.1)$$

where $\hat{\sigma}_{i,j}^{(0)}$ denotes the partonic cross section in leading order of perturbation theory, and $\Phi_{i|A}(x_a)$, $\Phi_{j|B}(x_b)$ are parton distribution functions (PDFs) or parton densities, which represent the probability to find a parton $i(j)$ with momentum fraction $x_a(x_b)$ in a hadron $A(B)$. The total hadronic cross section is integrated over all possible fractions of momenta and summed over all partons within the respective hadron. The parton densities only depend on the momentum fraction x but not on the momentum transfer. This corresponds to a manifestation of Bjorken scaling.

It is within the parton densities where the non-perturbative effects are included. Obviously, it is not possible to calculate them using the perturbative approach. Instead they have to be determined from experiments. It is important to realize that the parton densities depend on the hadron structure alone and are completely independent of the nature of the hard process. This makes them universal and therefore, they can be used for calculation of any hadronic cross section.

The concept of splitting the hadronic cross section into a perturbative partonic cross section and non-perturbative parton densities is a fundamental statement of the parton model, referred to as factorization [82].

So far, only the leading order effects were considered. Taking into account higher orders of perturbation series violates the Bjorken scaling. As a result, the parton densities become dependent on the momentum transfer in the interaction and the simple expression for the hadronic cross section given in Eq. (5.1) is no longer valid. Hence, it is evident that a generalization of the parton model and of the factorization theorem is necessary.

5.2   Factorization

As already mentioned in the previous section, factorization is the statement that the cross section for any hadronic process may be written as the convolution of two terms: a calculable hard scattering cross section and a non-perturbative parton density. To generalize this statement it is better to refer to a splitting into short-distance and long-distance interactions or from the point of view of energy into hard and soft effects. Obviously, such separation requires to introduce an energy scale, the factorization scale μ_f, additional to the renormalization scale μ, which is necessary in any perturbative
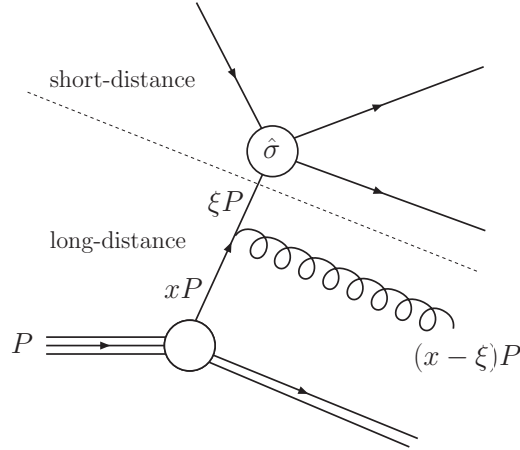
Figure 5.2: The schematic structure of a hadronic process as given by factorization. The process can be split into a short-distance part which corresponds to a hard process at the partonic level and a long-distance part which includes non-perturbative effects together with soft and collinear gluon radiation. The momentum fraction ξ of the parton which enters the hard process is reduced by gluon radiation. $\hat{\sigma}$ denotes the partonic cross section from which the mass singularities have been factorized.

computation. It is often convenient to choose the two scales μ and μ_f to be equal but this is not necessary in general.

As a consequence, the hadronic cross section is given by

$$\sigma_A(P_A, P_B) = \sum_{i,j} \int_0^1 \int_0^1 dx_a dx_b\, \hat{\sigma}_{i,j}(x_a P_A, x_b P_B, \mu_f)\, \Phi_{i|A}(x_a, \mu_f)\, \Phi_{j|B}(x_b, \mu_F)\,,$$

(5.2)

where $\hat{\sigma}$ denotes the short-distance partonic cross section and Φ_A, Φ_B are the parton densities which include long-distance interactions. The splitting between these two is realized at a factorization scale μ_f.

For illustration, the factorization of a hadronic process into long- and short-distance parts is shown in Fig. 5.2. As an example of long-distance effects the process of initial state radiation is sketched. Typically, this process involves the radiation of gluons which give rise to the characteristic gluonic radiative corrections. Due to the zero-mass of the gluon and to the fact that the masses of the light quarks are negligible with respect to the exchanged energies, the radiative corrections contain infrared and mass singularities. The origin of infrared singularities is related to the soft gluon radiation whereas the mass singularities, also called collinear singularities, emerge if a massless quark radiates a collinear gluon.

Although both soft and collinear gluon contributions can be calculated within per-

turbation theory, they are experimentally unresolvable. Therefore, they cannot be distinguished from other long-distance effects and are implicitly present in all measurements from which the parton densities are extracted. For a consistent computation of the hadronic cross section it is necessary that the short-distance partonic cross section is infrared-safe and also the mass singular terms have to be subtracted and absorbed into the parton densities.

5.2.1 Factorization schemes

Beyond lowest order in perturbation theory there is considerable ambiguity in separating the hard scattering cross section from the corresponding parton distributions. It is obvious that the choice of the factorization scale is not unique. Also, finite terms related to the higher order contributions can be arbitrarily distributed between the partonic cross section and the parton densities. A set of rules that makes these choices is called a factorization scheme.

It is absolutely crucial to use schemes consistently and to know in which scheme any given calculation or comparison to data is carried out. The two most commonly used factorization schemes are:

(i) **DIS factorization scheme**

The DIS scheme [85] is appealing for its close correspondance to experiment. In this scheme, order-by-order in perturbation theory, all higher order corrections to the structure function F_2 are absorbed into the distributions of quarks and antiquarks. The gluon distribution is not fixed. The factorization and renormalization scales are set to $\mu = \mu_f = Q$, where $Q^2 = -q^2$ and q is the lepton–hadron space-like momentum transfer, as defined in Fig. 5.1.

(ii) $\overline{\text{MS}}$ **factorization scheme**

The modified minimal subtraction scheme [74], in contrast to the DIS scheme, is theoretically more elegant and simple for calculations. It is defined in the framework of dimensional regularization. In this scheme the parton distributions are given directly in terms of hadronic matrix elements [86].

The connection between the two schemes in terms of definitions of the proton structure function F_2 can be found e.g. in [85].

It is important to stress that predictions for physical quantities are scheme independent. The only effect of a change in the renormalization and factorization scheme is to distribute the radiative corrections differently between the parton cross section, the structure functions and the strong coupling α_s.
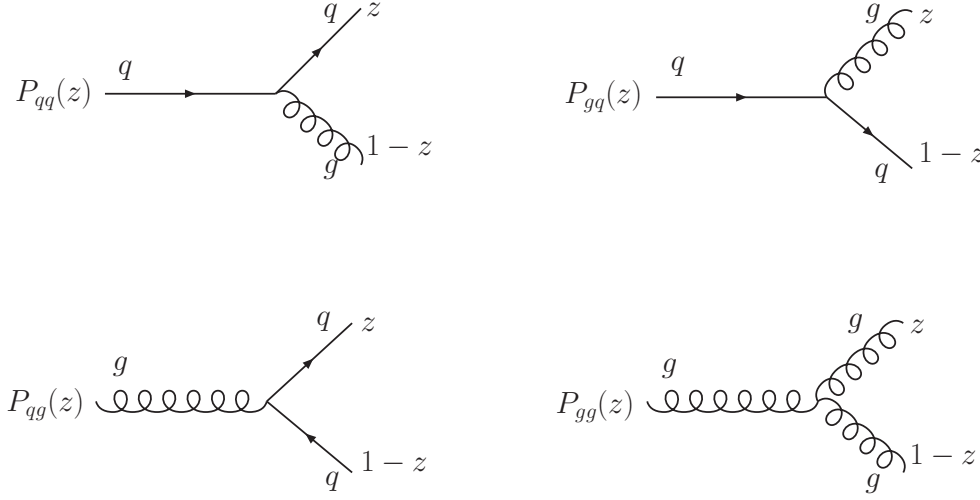
Figure 5.3: The splitting functions.

5.2.2   Splitting functions

Usually, the parton densities are extracted from measurements of the structure functions of hadrons in lepton–hadron deep inelastic scattering. As a consequence, they are determined at energy scales specific for the particular DIS interaction. However, for a consistent computation of hadronic cross sections, it is necessary to have access to parton densities at any scale fixed by the factorization. Thanks to the combination of the parton model and perturbative QCD, it is possible to evolve the parton densities using the evolution equations developed by Dokshitzer, Gribov, Lipatov, Altarelli and Parisi, collectively referred to as DGLAP evolution equations (see [87] and references therein). The DGLAP equations are coupled equations which desribe the change of the quark, antiquark, and gluon densities with the energy scale $\ln Q^2$ as

$$\frac{\partial}{\partial \ln Q^2} \left(\begin{array}{c} q_i(x, Q^2) \\ g(x, Q^2) \end{array} \right) = \frac{\alpha_s(Q^2)}{2\pi} \sum_j \int_x^1 \frac{d\xi}{\xi} \qquad (5.3)$$

$$\left(\begin{array}{cc} P_{q_i q_j}(\frac{x}{\xi}, \alpha_s(Q^2)) & P_{q_i g}(\frac{x}{\xi}, \alpha_s(Q^2)) \\ P_{g q_j}(\frac{x}{\xi}, \alpha_s(Q^2)) & P_{gg}(\frac{x}{\xi}, \alpha_s(Q^2)) \end{array} \right) \left(\begin{array}{c} q_j(\xi, Q^2) \\ g(\xi, Q^2) \end{array} \right)$$

where q_i, q_j are taken to include both the quark and antiquark distributions, g denotes the gluon distribution, and i, j are the flavor indices. The splitting functions P_{gg}, P_{qg}, P_{gq} and $P_{q_i q_j}$, also called evolution kernels, are the essence of DGLAP equations and describe the probabilities that a quark or gluon splits into a pair of partons. They are summarized graphically in Fig. 5.3.

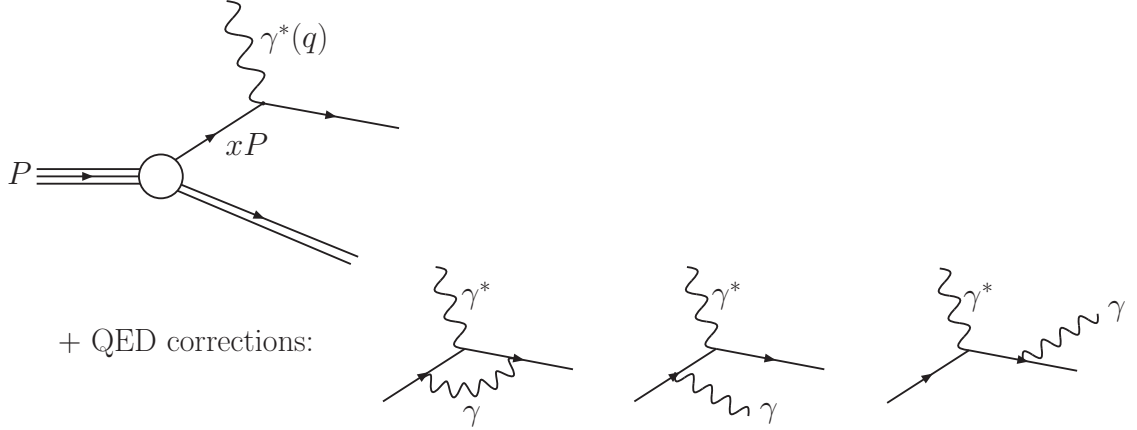The splitting functions P_{qg} and P_{gq} are flavor independent and identical for quarks

Figure 5.4: The QED one-loop corrections in deep inelatic lepton–hadron scattering.

and antiquarks. The $P_{q_i q_j}$ satisfy $P_{q_i q_j} = P_{\bar{q}_i \bar{q}_j}$ and $P_{q_i \bar{q}_j} = P_{\bar{q}_i q_j}$ and vanish at leading order unless $q_i = q_j$. The splitting functions can be expanded in $\alpha_s(Q^2)$. The leading order terms are given in appendix C.1.

5.3   Parton distributions with QED contributions

Parton distributions are an essential ingredient of hadron collider phenomenology. In order to allow for precision calculations, they have to be determined with an accuracy corresponding to the partonic level results. In the context of perturbative QCD, the current frontier is next-to-next-to-leading order (NNLO). Just from naive assumptions, also radiative corrections of the order $\mathcal{O}(\alpha)$ are expected to be numerically important at this level.

At the order $\mathcal{O}(\alpha)$, the QED contributions are of particular importance. Due to collinear photon emission off the incoming quarks, large logarithmic terms appear. These are proportional to $\alpha \log(Q^2/m^2)$. In principle, it would be possible to take these logarithms explicitly into account, but this would require a consistent choice of input quark masses. Furthermore, at very high Q^2 scales probed at hardon colliders, a resummation of these logarithms would be necessary.

Both difficulties can be avoided if applying an analogue of the QCD factorization theorem valid for the QED. As a result the collinear photon-induced logarithms can be absorbed into the parton distribution functions, exactly as it is done for for the collinear gluon-induced contributions in perturbative QCD (see e.g. [88]). By correctly taking into account the QED effects through modified DGLAP evolution equations (see appendix C.2), it is possible to obtain a consistent procedure for the overall electroweak

corrections to hard scattering processes involving initial state hadrons (see e.g. [89]).

In order to derive the parton distribution functions at next-to-leading order (NLO) in QED, virtual and real photonic contributions to lepton–nucleon DIS scattering, as shown in Fig. 5.4, have to be computed. First quantitave estimates of the QED effects on the evolution of parton distributions was made in [90], more recent investigation in [91]. However, both studies were based on a global QCD-only analysis of data and did not attempt to incorporate the QED effects to the best fit of data.

Fully consistent treatment was done by the MRST group in [92] and finally, parton distributions at NLO QED level are available. Although the QED corrections have only a very small effect on the evolutions of quarks and gluons, they have interesting side effects. They lead to isospin violation, since photons, unlike gluons, are not flavor blind. Furthermore, a distribution of photons inside the proton emerges.

Chapter 6

Top pair production at NLO QED

The top quark was discovered in 1995 by the CDF [93] and DØ [94] experiments at the Tevatron collider at Fermilab. Since then the experimental efforts have been concentrated on detailed studies of its properties as these provide significant consistency tests of the SM. The top quark mass is an important parameter within the SM and helps to give constraints on the mass of the Higgs boson [14, 15]. Currently, the value of the top quark mass as given by the world average [95] is

$$m_t = 171.4 \pm 2.1 \, \text{GeV} \,, \tag{6.1}$$

which is fully consistent with the SM prediction obtained from the global fit to all available electroweak data [14]

$$m_t = 171.7^{+2.0}_{-2.0} \, \text{GeV} \,. \tag{6.2}$$

In contrast to other fermions of the SM, the top quark is extremely heavy and therefore also extremely short-lived. As a consequence, it decays essentialy as a quasi-free quark [96]. Obviously, the top quark is one of the most interesting objects currently accessible in experiments.

6.1   Top pair production

The measurement of the top pair production cross section, $\sigma_{t\bar{t}}$, at hadron colliders is an important test of the SM. The observation of deviations from the SM prediction, which includes the higher order corrections, could indicate new non-standard production and decay mechanism. Also, precise knowledge of the SM processes as a main source of the background is crucial in direct searches for potential physics beyond the SM.

The measurement of $\sigma_{t\bar{t}}$ in $p\overline{p}$ collisions at $\sqrt{s} = 1.96$ TeV, performed at the Tevatron using $\sim 1 \, \text{fb}^{-1}$ of data collected during RUN II, gives a preliminary combined
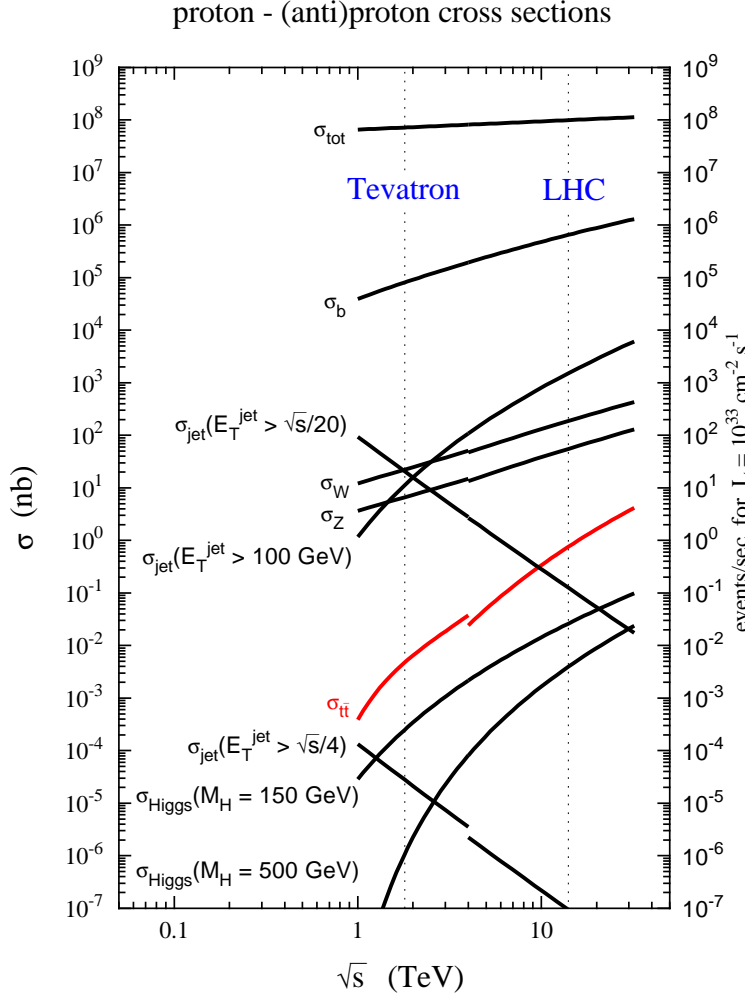
proton - (anti)proton cross sections

Figure 6.1: The comparison of the total hadronic cross section for various production channels at the Tevatron and LHC [98]. Red lines indicate predictions for the top pair production.

result[1] [97]

$$(\text{CDF}) : \sigma_{t\bar{t}} \left(m_t = 175 \, \text{GeV} \right) = 7.3 \pm 0.5 \, (\text{stat}) \pm 0.6 \, (\text{syst}) \pm 0.4 \, (\text{lumi}) \, \text{pb} \,. \quad (6.3)$$

An enhancement of about a factor of 100 is expected at the LHC (Fig. 6.1). Therefore, the LHC is anticipated to be a real "top factory" producing about 8 million $t\bar{t}$ pairs per year of running (at low luminosity). Apparently, this provides favorable conditions for numerous top quark studies.

Since the $t\bar{t}$ production cross section in pure QCD contains besides α_s the top quark mass as the only free parameter, it is suitable for the measurement of m_t. For a

---

[1]Cross section obtained combining results from all reconstruction channels at CDF. For DØ the combined result including RUN II data is not yet available.

consistent comparison with the value of m_t obtained from the reconstruction of $t\bar{t}$ decay products it is necessary to achieve a high precision in the cross section measurement. Thus radiative corrections have to be taken into account.

In lowest order, the $t\bar{t}$ production cross section in hadronic collisions is of $\mathcal{O}(\alpha_{\mathrm{s}}^2)$ and was calculated in [99]. The corresponding lowest order electroweak contributions of $\mathcal{O}(\alpha^2)$ to the Drell-Yan annihilation process via γ- and Z-exchange can be neglected. They contribute less than 1% at the partonic level owing to large m_t [100] and for this reason they are completely insignificant.

Dominant higher order contributions come from the QCD interactions. Cross sections and distributions including QCD effects to the order of $\mathcal{O}(\alpha_{\mathrm{s}}^3)$ were computed in [88], and an inspection of the QCD effects close to the production threshold was performed in [101]. Including the resummation of large logarithmic QCD contributions in the threshold region improves perturbative calculation and was done in [102, 103]. The prediction for $\sigma_{t\bar{t}}$ currently used at the Tevatron,

$$\sigma_{t\bar{t}}\,(m_t = 175\,\mathrm{GeV}) = 6.8^{+0.7}_{-0.9}\,\mathrm{pb}\,, \tag{6.4}$$

is based on the studies in [104] which include the next-to-leading-order (NLO) contributions and the resummation of soft logarithms to all orders of perturbation theory. In [105], also the next-to-next-to-leading-order (NNLO) soft-gluon corrections were taken into account. The measured value of $\sigma_{t\bar{t}}$ of Eq. (6.3) is in a good agreement with the SM prediction of Eq. (6.4), and the experimental precision is approaching the theoretical accuracy of $\sim \pm 12\%$ [97]. In the case of the LHC, the estimation of the next-to-leading-order and next-to-leading-log (NLO+NLL) QCD effects, as done in [103], gives

$$\sigma_{t\bar{t}}\,(m_t = 175\,\mathrm{GeV}, \mu = m_t) = 833\,\mathrm{pb}\,. \tag{6.5}$$

Also, the subclass of electroweak (EW) one-loop corrections of $\mathcal{O}(\alpha\alpha_{\mathrm{s}}^2)$, corresponding to the non-photonic contributions, was investigated [106]. These are of special interest due to the large Yukawa coupling of the top quark to the Higgs boson. However, they have little impact on the $\sigma_{t\bar{t}}$ within the SM, which is only $\sim 1\%$ of the Born-level cross section at the Tevatron, and the EW contributions do not exceed $\sim 3\%$ at the LHC [106, 107]. In these calculations contributions including the interference of QCD and EW interactions were neglected. A study of the non-photonic EW corrections with the gluon–Z interference effects was done in [108] and recently in [109–111].

Still, a subset of the full EW corrections, corresponding to the QED corrections, was not included in the previous calculations. To complete the SM prediction at the one-loop level, also the QED corrections have to be investigated.

To present a complete overview of the status of radiative corrections to the top quark pair production at hadron colliders, it is necessary to mention the studies of the higher order effects within certain extensions of the SM. These studies comprise calculations of the $\mathcal{O}(\alpha)$ one-loop corrections within the General 2-Higgs-Doublet Model (G2HDM) for both, the Tevatron [112] and the LHC [113]. Also, the SUSY QCD $\mathcal{O}(\alpha^2)$ contributions were investigated for the Tevatron [114, 115] and the LHC [116]. As SUSY provides an interesting extension of the EW sector, the SUSY EW corrections have been examined. Partial calculations relevant for the Tevatron were done in [115, 117]. The complete description of the top pair production cross section to $\mathcal{O}(\alpha\alpha_s^2)$, within the G2HDM and MSSM, with numerical results for the Tevatron and the LHC, was presented in [118].

In the following, we investigate the QED corrections to top pair production within the SM, but the computation is also valid for extensions (MSSM, G2HDM, ...). The effects from the interference of QCD and QED interactions are included. At this order the distribution of photons inside the proton becomes non-zero, adding further contribution to our calculation. In the end, we present numerical results for both, the Tevatron and the LHC.

6.1.1 $t\bar{t}$ cross section at the partonic level

At LHC energies, the $t\bar{t}$ production proceeds mainly through the fusion of two gluons

$$g^a(p_4) + g^b(p_3) \rightarrow t^j(p_2) + \bar{t}^l(p_1),$$

whereas at the Tevatron, the dominant production mechanism is the annihilation of a quark–antiquark pair

$$q_\alpha^i(p_4) + \overline{q}_\beta^k(p_3) \rightarrow t^j(p_2) + \bar{t}^l(p_1),$$

with α, β and i, j, k, l, a, b being flavor and color indices, respectively. The momenta of the interacting particles are denoted in brackets. Feynman diagrams for both production subprocesses are shown in Fig. 6.2. As already mentioned, the lowest order $\mathcal{O}(\alpha^2)$ contributions are negligible [100].

Expressions for the $\mathcal{O}(\alpha_s^2)$ Born-matrix elements, as given in [106], read

$$
\begin{aligned}
\mathcal{M}_B^{q\bar{q}} &= \delta_{\alpha\beta}\, \bar{u}_t^j(p_2)(-ig_s T_{jl}^c \gamma_\mu)\, v_{\bar{t}}^l(p_1) \left(\frac{-ig^{\mu\nu}}{\hat{s}}\right) \bar{v}_\beta^k(p_3)(-ig_s T_{ik}^c \gamma_\nu)\, u_\alpha^i(p_4) \;, \\
\mathcal{M}_B^{gg} &= g_s^2\, \epsilon_4^\mu(p_4)\, \epsilon_3^\nu(p_3)\, \bar{u}_t^j(p_2)\, T_{\mu\nu}^{ab}\, v_{\bar{t}}^l(p_1) \;,
\end{aligned}
\tag{6.6}
$$

where ϵ_3 and ϵ_4 are the polarization vectors of the gluons. In the gluon fusion channel,
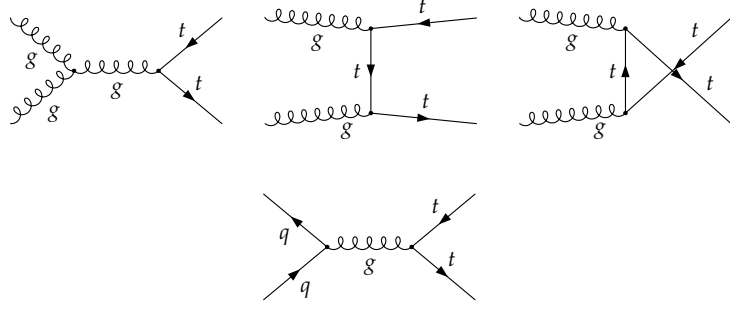
Figure 6.2: Feynman diagrams for the gg fusion and $q\bar{q}$ annihilation at leading order in QCD.

the following tensor notation has been used

$$
\begin{aligned}
T_{\mu\nu}^{ab} \quad = \quad & \frac{T_{jl}^c f_{abc}}{\hat{s}} \left[(\not{p}_4 - \not{p}_3)g_{\mu\nu} + (2p_3 + p_4)_\mu \gamma_\nu - (2p_4 + p_3)_\nu \gamma_\mu \right] \quad : \; s\text{-channel} \\
& + \frac{(-i)T_{jm}^a T_{ml}^b}{\hat{t} - m_t^2} \gamma_\mu(\not{p}_3 - \not{p}_1 + m_t)\gamma_\nu \quad : \; t\text{-channel} \\
& + \frac{(-i)T_{jm}^b T_{ml}^a}{\hat{u} - m_t^2} \gamma_\nu(\not{p}_4 - \not{p}_1 + m_t)\gamma_\mu \quad : \; u\text{-channel} . \quad\quad\quad (6.7)
\end{aligned}
$$

In the expressions above, α, β and i, j, k, l, m, a, b, c are flavor and color indices, respectively, T_{ij}^a denote the color generators and $\hat{s} = (p_1+p_2)^2 = (p_3+p_4)^2$, $\hat{t} = (p_3-p_1)^2$ and $\hat{u} = (p_4 - p_1)^2$ are the Mandelstam variables.

6.2 Structure of the NLO QED contributions

The QED sector can be treated independently from the weak part of the SM as a result of its direct relation to the unbroken electromagnetic gauge invariance. The pure QED corrections therefore form a substantial subclass of the complete electroweak $\mathcal{O}(\alpha)$ corrections. They consist of virtual and real contributions, according to the topology of photonic insertions. Both classes have to be combined in order to obtain a consistent, infrared (IR) finite result.

6.2.1 Virtual corrections

The virtual QED corrections consist of loop contributions with virtual photons. They can be described by the matrix elements $\delta\mathcal{M}_i$, $i = gg, q\bar{q}$ for both production subprocesses separately. Contracting these quantities with the Born-matrix elements $\mathcal{M}_B^i$, listed in the previous section, leads to differential cross sections at the partonic level
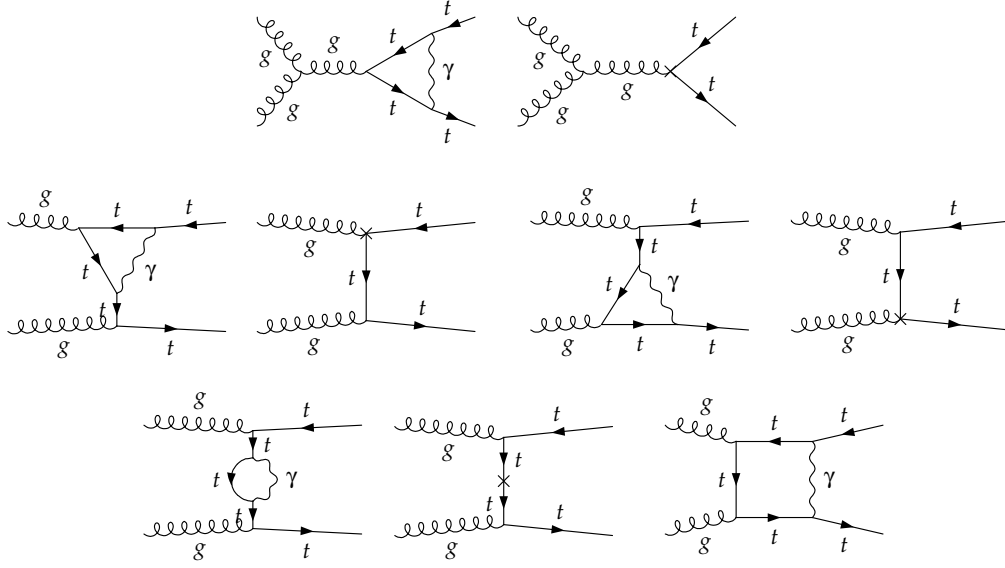
Figure 6.3: Feynman diagrams for the virtual QED $\mathcal{O}(\alpha\alpha_s^2)$ contributions to the gluon fusion (*u*-channel diagrams are not explicitly shown). Diagrams with crossed lines and vertices denote the counter terms.

of the order of $\mathcal{O}(\alpha\alpha_s^2)$

$$\frac{d\hat{\sigma}_i(\hat{t},\hat{s})}{d\hat{t}} = \frac{1}{16\pi^2\hat{s}}2\mathcal{R}e\overline{\sum}(\delta\mathcal{M}_i \times \mathcal{M}_B^{i*}) , \tag{6.8}$$

where $\hat{s}$ and $\hat{t}$ are the Mandelstam variables, as defined above.

The virtual QED corrections of $\mathcal{O}(\alpha\alpha_s^2)$ can be rearranged into self-energy, vertex and box corrections, according to the topology of Feynman diagrams which are shown in Figs. 6.3 and 6.4 for both production subprocesses. The contributing Feynman diagrams and the corresponding amplitudes were generated using *FeynArts* [119]. Subsequently, the algebraic reduction of one-loop tensor integrals into scalar integrals
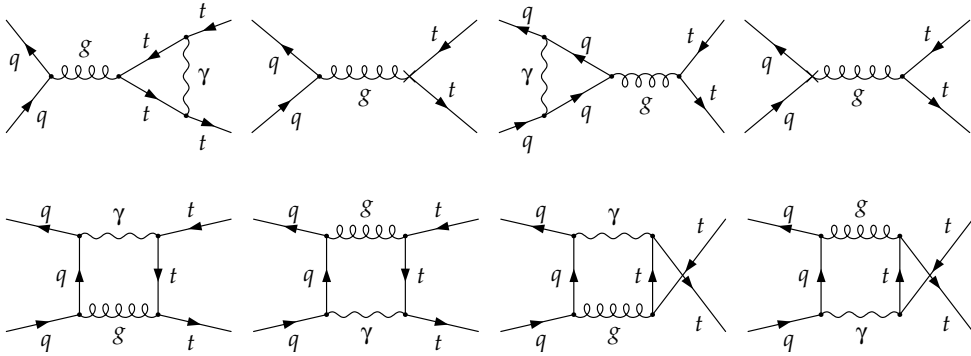

Figure 6.4: Feynman diagrams for the virtual QED $\mathcal{O}(\alpha\alpha_s^2)$ contributions to the $q\overline{q}$ annihilation. Diagrams with crossed vertices denote the counter terms.

was supported by *FormCalc* [120], and the scalar integrals were then evaluated with help of *LoopTools* [121]. The treatment of loop integrals is based on the basic reduction techniques worked out in [122, 123] which were further extended for 4-point loop integrals in the box contributions in [124, 125]. Some details about the classification and computation of loop integrals can be found in appendix D .

Due to the gauge invariance of QED, the whole set of one-loop contributions is gauge invariant. To compensate the ultraviolet (UV) singularities in the loop integrals, counter terms for the $gq\bar{q}$-vertex, $gt\bar{t}$-vertex and the top quark self-energy have to be included. There is no counter term for the gluon self-energy at $\mathcal{O}(\alpha)$ level since photons do not couple directly to gluons. The Ward Identity preserves the cancellation of UV singularities in the sum of vertex functions and corresponding counter terms with renormalization constants of the quark fields. Thus no coupling constant renormalization is needed.

The renormalization procedure, as described in section 4.2, consists in the first step of the replacement of bare parameters in the Lagrangian by the renormalized quantities. In the case of top quarks,

$$
\begin{aligned}
\Psi_{L,R} &\rightarrow \left(1 + \frac{1}{2}\delta Z_{L,R}\right)\Psi_{L,R} , \\
m_t &\rightarrow m_t - \delta m_t ,
\end{aligned}
\tag{6.9}
$$

where $\Psi_{L,R}$ are the left- and right-handed components of the quark fields. This yields the counter terms for the $gt\bar{t}$-vertex, $\delta\Lambda_\mu$, and for the top quark self-energy, $\delta\Sigma$ (denoted by crossed lines and vertices in Figs. 6.3 and 6.4), at NLO QED as follows:

$$
i\delta\Lambda_\mu = -ig_s T^c \gamma_\mu \, \delta Z_V ,
\tag{6.10}
$$

$$
i\delta\Sigma = i\left(\not{p}\,\delta Z_V - m_t\,\delta Z_V + \delta m_t\right) ,
\tag{6.11}
$$

with

$$
\delta Z_V = \frac{1}{2}\left(\delta Z_L + \delta Z_R\right) .
\tag{6.12}
$$

The renormalization constant of the top quark field, δZ_V, as well as the renormalization constant of the top quark mass, δm_t, have to be fixed within a renormalization scheme. We choose the on-shell renormalization scheme and impose the appropriate renormalization conditions on the renormalized top quark self-energy $\hat{\Sigma}$ that is defined

as a sum of the unrenormalized self-energy Σ and the corresponding counter term $\delta\Sigma$, as given in Eq.(6.11),

$$\hat{\Sigma} = \Sigma + \delta\Sigma \ . \tag{6.13}$$

The on-shell renormalization conditions that fix the finite parts of the counter terms are given in the following:

(i) Within the on-shell renormalization scheme the pole of the top quark propagator[2] defines the on-shell top quark mass:

$$\hat{\Sigma}\left(\slashed{p} = m_t\right) = 0 \ , \tag{6.14}$$

such that the mass renormalization constant is fixed by

$$\frac{\delta m_t}{m_t} = -(\Sigma_V + \Sigma_S)\big|_{p^2 = m_t^2} \ . \tag{6.15}$$

(ii) The residue of the top quark propagator is equal to one, which is equivalent to

$$\lim_{\slashed{p} \to m_t} \frac{1}{\slashed{p} - m_t} \hat{\Sigma}(\slashed{p}) = 0 \ , \tag{6.16}$$

fixing the wave function renormalization constants by

$$\delta Z_V = -\Sigma_V(p^2 = m_t^2) - 2m_t^2 \frac{\partial}{\partial p^2}(\Sigma_V + \Sigma_S)\big|_{p^2 = m_t^2} \ . \tag{6.17}$$

At NLO QED, the top quark self-energy consists of a single virtual photon insertion and can be defined as

$$: \quad i\,\Sigma \tag{6.18}$$

with

$$\Sigma(\slashed{p}) = \frac{\alpha}{4\pi} \left[\slashed{p}\,\Sigma_V(p^2) + m_t \Sigma_S(p^2) \right] \ , \tag{6.19}$$

where the vector and scalar components, $\Sigma_{V,S}$, can be expressed in terms of 2-point loop integrals (see appendix D) as

$$\begin{aligned}
\Sigma_V(p^2) &= -Q_t^2 \left(2B_1(p^2, m_t, \lambda) + 1 \right) \ , \\
\Sigma_S(p^2) &= -Q_t^2 \left(4B_0(p^2, m_t, \lambda) - 2 \right) \ .
\end{aligned} \tag{6.20}$$

[2]The renormalization conditions fix the real parts of the propagators, in this case $\mathrm{Re}\hat{\Sigma} = \hat{\Sigma}$.

The renormalization constants of initial state quarks are determined in analogy with the case of heavy final state quarks, by substituting $m_t \rightarrow m_q$. To obtain the counter terms for the initial state $gq\overline{q}$ vertices (Fig. 6.4), only the renormalization of the quark fields is necessary. Although we neglect the light quark masses whenever possible, it cannot be done here, since they are needed for the derivatives of Eq. (6.17). The role of the parameter λ is discussed below.

As a consequence of the null photon mass, the virtual QED corrections are infrared (IR) divergent. The photonic IR singularities can be regularized by introducing a fictitious photon mass λ, which has to be inserted into the expressions of Eq. (6.20) in order to obtain a finite derivative of the self-energy. The regularization by a photon mass is allowed because the gauge invariance of QED, $U(1)_Q$, is not violated by an explicit mass term for the gauge boson. Obviously, the predictions for physical quantities, such as cross sections, must be free of the parameter λ. To satisfy this condition, also the real photonic corrections have to be taken into account. These will be discussed in the next section.

Following the previous notes on renormalization and regularization of the IR singularities related to photon is sufficient to determine the virtual QED corrections to the gg fusion subprocess. Analytical expressions for the corresponding matrix elements, $\delta\mathcal{M}_{gg}$, are similar to the formulas for the Z and W boson EW corrections, which were calculated in [106]. The results are summarized in appendix E.

Concerning the $q\overline{q}$ annihilation production channel, the singular structure of QED corrections is more complicated. In the vertex correction to the final state, only the photons yield IR singular contributions. Due to negligible masses of initial state quarks, there are, however, additional mass singularities present in the initial state vertex correction. These singularities, proportional to $\ln^2(\hat{s}/m^2)$, are known from QCD as the Sudakov double logarithms. There are also single mass logarithms, $\ln(\hat{s}/m^2)$, originating from the collinear photon emission, as already mentioned in section 5.3. Hence, both the photon mass parameter and the mass of initial state quarks, are needed for the regularization.

The $\mathcal{O}(\alpha\alpha_s)$ box contributions shown in Fig. 6.4 contain besides photons also gluons in the loop. As a result, IR singularities related to the gluons emerge in the loop integrals. Although gluons, unlike photons, do not interact via an Abelian vertex only, it is still possible to perform regularization by giving the gluon a mass. This is a direct consequence of the fact that at $\mathcal{O}(\alpha\alpha_s)$, the box contribution is still Abelian-like and the non-Abelian triple-gluon vertex does not interfere. For this reason the same assumptions are valid for the gluon as for the photon, and for simplicity, the
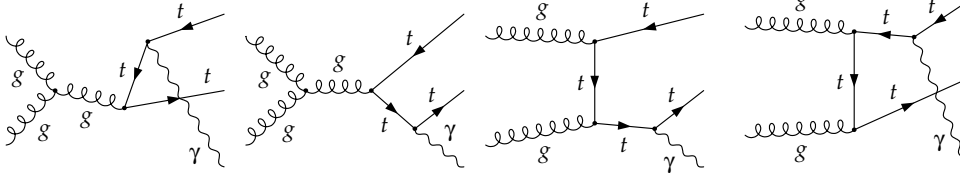
Figure 6.5: Feynman diagrams for the real QED $\mathcal{O}(\alpha\alpha_{\mathrm{s}}^2)$ contributions of photon bremsstrahlung to the gg fusion (u-channel diagrams are not explicitly shown).
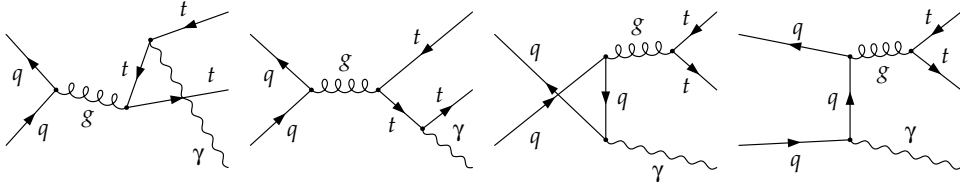

Figure 6.6: Feynman diagrams for the real QED $\mathcal{O}(\alpha\alpha_{\mathrm{s}}^2)$ contributions of photon bremsstrahlung to the $q\bar{q}$ annihilation.

same regularization parameter λ can be used. The calculation of the virtual QED corrections to the $q\bar{q}$ annihilation is analogous to the computation of e^+e^- annihilation to heavy fermion pairs, which was performed in [126]. Just simple replacements of $m_e \to m_q$ and $m_f \to m_t$, and appropriate choices of the coupling constant and of the color factor are needed to deduce explicit analytical formulas. These are presented in appendix E.

6.2.2   Real corrections

According to the Bloch-Nordsieck theorem [127], the IR singularities cancel in the sum of virtual and real corrections. Although single virtual and real contributions contain the IR singular terms of $\ln(\lambda)$, which are necessary to regularize singularites originating from the vanishing photon momentum, these are fully compensated in the sum of photonic corrections. This fact reflects the physical reality that photons with such low momenta cannot be detected in any realistic experiment. Hence, the virtual and real photons cannot be distinguished if they are soft, as a consequence of the finite detector resolution. Obviously, any attempt to split the virtual and real corrections in the soft limit leads to unphysical IR divergent results.

Therefore, we have to add all real photon contributions of the appropriate order to the virtual part in order to obtain an IR finite result. Feynman diagrams for the photon bremsstrahlung off external quarks, which give corrections of $\mathcal{O}(\alpha\alpha_{\mathrm{s}}^2)$, are illustrated in Figs. 6.5 and 6.6.
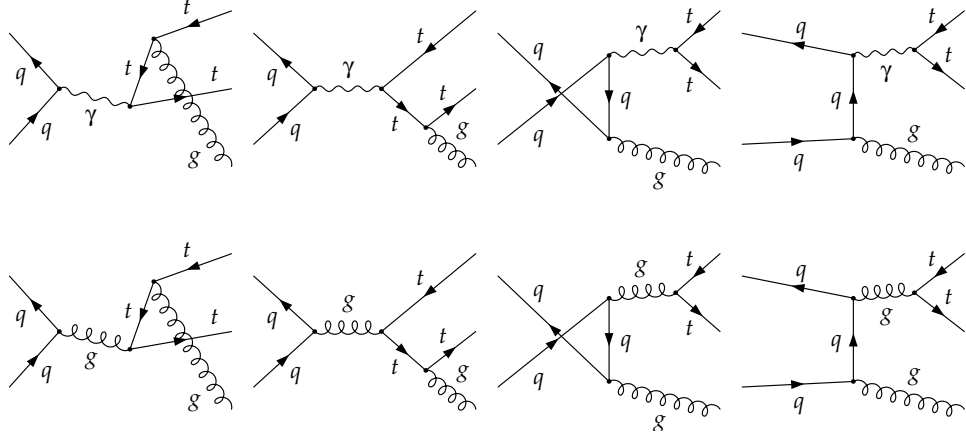
Figure 6.7: Feynman diagrams for the real gluonic contributions to the $q\overline{q}$ annihilation corresponding to gluon bremsstrahlung off the QED-mediated (first row) and off the QCD-mediated tree-level diagram (second row). Only the interference of QED and QCD diagrams yields contributions of the appropriate order.

So far we have included the real corrections that are necessary to eliminate the IR singularities related to the photon. However, there are also gluonic IR singularities in the $\mathcal{O}(\alpha\alpha_{\mathrm{s}})$ box contributions in the $q\overline{q}$ annihilation (see section 6.2.1). For this reason we also need to include the real gluonic corrections. There are two candidate classes of possible Feynman diagrams for the gluon bremsstrahlung. These are either the gluon radiation off the QED-mediated or off the QCD-mediated $q\overline{q}$ annihilation, as illustrated in Fig. 6.7.

In order to compensate the IR singularities in the box corrections of Fig. 6.4, it is necessary to include the gluon bremsstrahlung of $\mathcal{O}(\alpha\alpha_{\mathrm{s}}^2)$. To construct contributions of this order, the two bremsstrahlung processes of Fig. 6.7 are separately not suitable, since they give contributions of $\mathcal{O}(\alpha_{\mathrm{s}}\alpha^2)$ and $\mathcal{O}(\alpha_{\mathrm{s}}^3)$, respectively. Nevertheless, the interference of these two is of the appropriate order, $\mathcal{O}(\alpha\alpha_{\mathrm{s}}^2)$. Still, not all of the QED–QCD interference terms contribute. Due to the color structure of the corresponding matrix elements, the initial state radiation as well as the final state radiation off the QED–QCD tree-level diagrams is zero. Only the interference of the initial and final state gluon radiation off the QED–QCD tree-level diagrams is non-zero. For concreteness, some of the non-zero bremsstrahlung contributions of $\mathcal{O}(\alpha\alpha_{\mathrm{s}}^2)$ are illustrated in Fig. 6.8.

When counting the IR-singular terms in the sum of QED–QCD interference diagrams of Figs. 6.8 and 6.4, uncompensated remnants come out. This indicates that some contributions of $\mathcal{O}(\alpha\alpha_{\mathrm{s}}^2)$ are still missing. In order to identify the necessary ingredient, we have to abandon the naive idea that the QED corrections to QCD tree-level
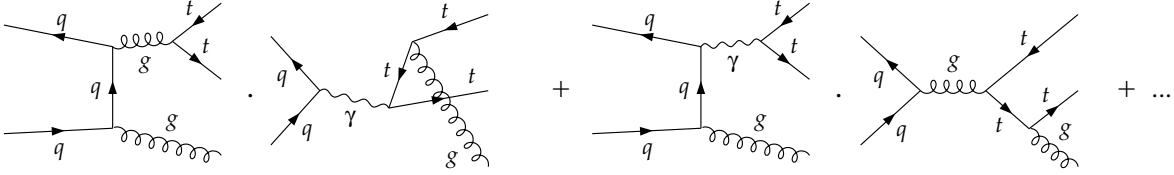
Figure 6.8: Non-zero contributions of $\mathcal{O}(\alpha\alpha_{\mathrm{s}}^2)$ corresponding to the interference of initial and final state gluon radiation off the QED-mediated and QCD-mediated $q\overline{q}$ annihilation.
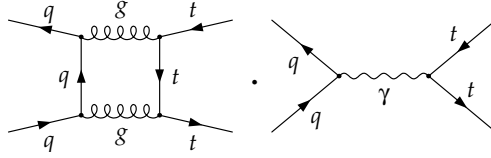

Figure 6.9: Feynman diagrams for the $\mathcal{O}(\alpha\alpha_{\mathrm{s}}^2)$ contributions to the $q\overline{q}$ annihilation corresponding to the interference of the QCD-mediated box diagram (crossed diagram is not explicitly shown), with the QED-mediated Born-level diagram.

processes can be separated from the rest of $\mathcal{O}(\alpha\alpha_{\mathrm{s}}^2)$ contributions. The same color and IR-singular structure is manifested in case of the pure QCD box corrections to the QED-mediated $q\overline{q}$ annihilation (Fig. 6.9), which are the $\mathcal{O}(\alpha\alpha_{\mathrm{s}}^2)$ contributions needed to obtain IR finite results at this order.

In Fig. 6.9, only the QED-mediated Born-level diagram is shown. However, due to the mixing between photon and Z-boson, which occurs in the $q\overline{q}$ annihilation at $\mathcal{O}(\alpha^2)$, also the interference of the QCD box and Z-boson tree-level diagram has to be taken into account. This contribution belongs to the IR-singular gluon–Z corrections, which likewise consist of the gluon–Z box corrections to the QCD-mediated Born diagram and of the gluon bremsstrahlung off the interference of QCD- and EW-mediated tree-level diagrams. The corresponding Feynman diagrams can easily be obtained by replacing the photon by the Z-boson in Figs 6.4, 6.7–6.9. The IR-singular structure of these contributions is simplified by the fact that there are no IR-singularities related to the Z-boson. Therefore, no contributions analogue to the photon bremsstrahlung (Fig. 6.6) are needed. The gluon–Z interference effects have been neglected in the original study of EW corrections performed in [106]. They have been investigated recently in [108], and were found to be less than about 1% of the $\mathcal{O}(\alpha_{\mathrm{s}}^2)$ Born-level $t\overline{t}$ total hadronic cross section.

In order to give a complete description of the NLO QED effects, we also mention the photon radiation off the off-shell top quarks in the gg fusion subprocess (Fig. 6.10). These contributions are of the respective order, $\mathcal{O}(\alpha\alpha_{\mathrm{s}}^2)$, but are of about two orders
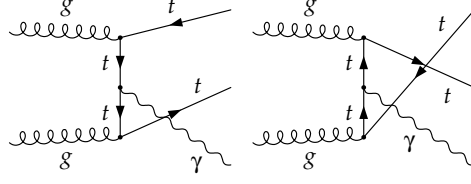
Figure 6.10: Feynman diagrams for the $\mathcal{O}(\alpha\alpha_{\mathrm{s}}^2)$ contributions to the gg fusion corresponding to the photon bremsstrahlung off the off-shell top quarks in t- and u-production channels.
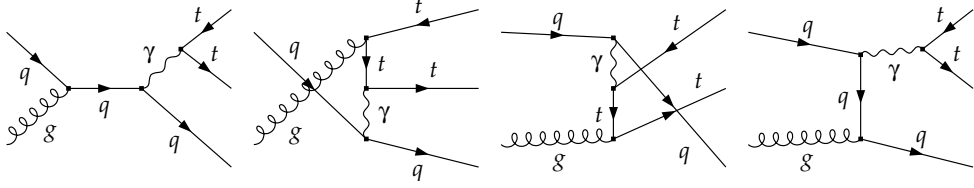

Figure 6.11: Feynman diagrams for the $\mathcal{O}(\alpha_{\mathrm{s}}\alpha^2)$ contributions to the gq partonic subprocess are suppressed with respect to the $\mathcal{O}(\alpha\alpha_{\mathrm{s}}^2)$ contributions.

of magnitude smaller than the IR-singular photon bremsstrahlung (Fig. 6.5). For this reason, they are not essential for the numerical studies and are only presented for completeness.

Up to now we were concentrating on the gg fusion and $q\bar{q}$ annihilation as $t\bar{t}$ production partonic subprocesses. At this point we should also mention the gluon–quark partonic subprocess (Fig. 6.11), which yields a contribution to the same final state as the QED–QCD interference diagrams of Figs. 6.8. However, the lowest order gluon–quark subprocess with QED–QCD interference results in contributions of $\mathcal{O}(\alpha_{\mathrm{s}}\alpha^2)$, and these are suppressed by the factor of $\mathcal{O}(\alpha/\alpha_{\mathrm{s}})$ with respect to the NLO QED contributions in the other two partonic subprocesses.

6.3 Photon-induced $t\bar{t}$ production

In addition to the previously mentioned NLO QED contributions we also have to inspect the photon-induced production channels. These comprise the gluon–photon and the quark–photon processes, which are illustrated in Figs. 6.12 and 6.13, respectively. Although at the partonic level these processes represent a different type of production channels than the $q\bar{q}$ annihilation and the gg fusion channels, they contribute to the same hadronic final state $t\bar{t}X$.

In general, photon-induced partonic processes vanish at the hadronic level unless the NLO QED effects are taken into account. As already mentioned in section 5.3, a
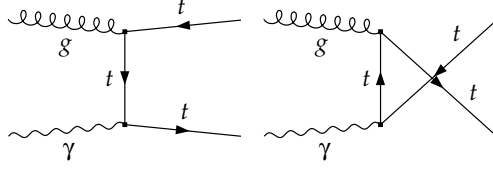
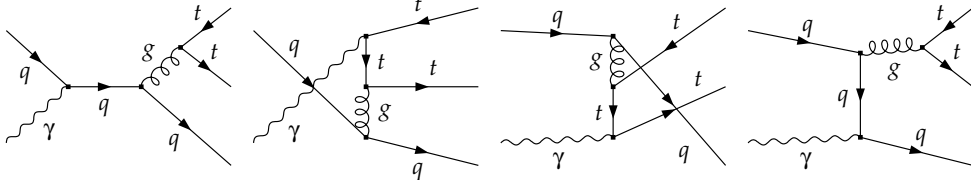Figure 6.12: Feynman diagrams for photon induced $t\bar{t}$ production in the photon–gluon scattering.

Figure 6.13: Feynman diagrams for the photon-induced $t\bar{t}$ production in the quark–photon partonic subprocess.

direct consequence of including these effects into the evolution of parton distribution functions (PDFs) is the non-zero photon density in the proton. This leads then to non-zero photon-induced contributions at the hadronic level.

In our case, convoluting the photon-induced partonic cross sections with the PDFs at NLO QED leads to non-zero contributions to the $pp/p\overline{p} \to t\overline{t}X$ hadronic processes. In the quark–photon channel, the collinear singularities related to the light initial state quarks are already present at the partonic level, whereas in the gluon–photon case, they enter only via PDFs. For this reason, the quark–photon channel represents an NNLO QED contribution and is suppressed with respect to the gluon–photon channel, which contributes to NLO in QED. Therefore, we only include the gluon–photon contribution to our numerical analysis. The corresponding Born-matrix elements can be expressed in analogy with the gluon fusion channel as

$$\mathcal{M}_B^{g\gamma} = (-ig_s e\, Q_t\, T_{jl}^a)\, \epsilon_4^\mu(p_4)\, \epsilon_3^\nu(p_3)\, \bar{u}_t^j(p_2)\, T_{\mu\nu}\, v_{\bar{t}}^l(p_1)\ , \tag{6.21}$$

where ϵ_3 and ϵ_4 are the polarization vectors of the photon and gluon. The tensor notation reads

$$
\begin{aligned}
T_{\mu\nu} \;=\; & \frac{1}{\hat{t}-m_t^2}\, \gamma_\mu(\slashed{p}_3-\slashed{p}_1+m_t)\gamma_\nu \quad : t\text{-channel} \\
& + \frac{1}{\hat{u}-m_t^2}\, \gamma_\nu(\slashed{p}_4-\slashed{p}_1+m_t)\gamma_\mu \quad : u\text{-channel}\ .
\end{aligned}
\tag{6.22}
$$

In the expressions above, we use the same conventions for color indices and momenta of the particles as in section 6.1.1.

As the PDFs at NLO QED became available only recently [92], the photon-induced hadronic processes have not yet been investigated. Here we present the first study of these effects on the top pair production.

6.4 Soft and collinear photon/gluon emission

The soft and collinear photon emission potentially implies numerical problems in the phase space integration of the radiative process. The phase space integral diverges in the soft region where the photon momentum k becomes very small ($k \to 0$), giving rise to IR singularities. If the fermion masses are set to zero, also the mass singularities emerge as a consequence of the collinear photon emission ($pk \to 0$, where p is the fermion momentum).

There are several methods for the treatment of soft and collinear singularities. In the following, we give a brief description of two approaches we used to evaluate the bremsstrahlung contributions: the dipole subtraction and the phase space slicing method. Throughout our calculations the phase space slicing method was adopted, taking advantage of its universality in handling both, the inclusive and non-inclusive quantities. The dipole subtraction method was used to verify numerical results obtained with the slicing method.

As the radiative process of $q\overline{q}$ annihilation is very similar to photon emission in e^+e^- annihilation, we closely followed the approach in [126]. In the case of gg fusion, the use of the dipole subtraction method was based on the study of $\gamma\gamma \to t\overline{t}$ in [128].

The treatment of real corrections is not fully included in *FormCalc* and *LoopTools*, and therefore we have developed and implemented the code necessary for the evaluation of soft and collinear contributions.

6.4.1 Phase space slicing

In the phase space slicing approach, the phase space is divided into regions where the integrand is finite and regions where the singularities occur. In the non-singular regions the integration is performed numerically, whereas in the singular parts it is carried out analytically using approximations for the soft and collinear photon or photon-like gluon (from now on just photon, for simplicity).

To locate the soft and collinear regions, two cut-off parameters, ΔE and $\Delta\theta$, are introduced. The soft cut-off parameter, ΔE, acts as boundary on the photon energy k^0 such that for $k^0 < \Delta E \ll \sqrt{\hat{s}}$, with $\sqrt{\hat{s}}$ being the total energy of the partonic system; the photon is soft. The collinear part is constrained by the angular cut-off, $\Delta\theta$, imposed
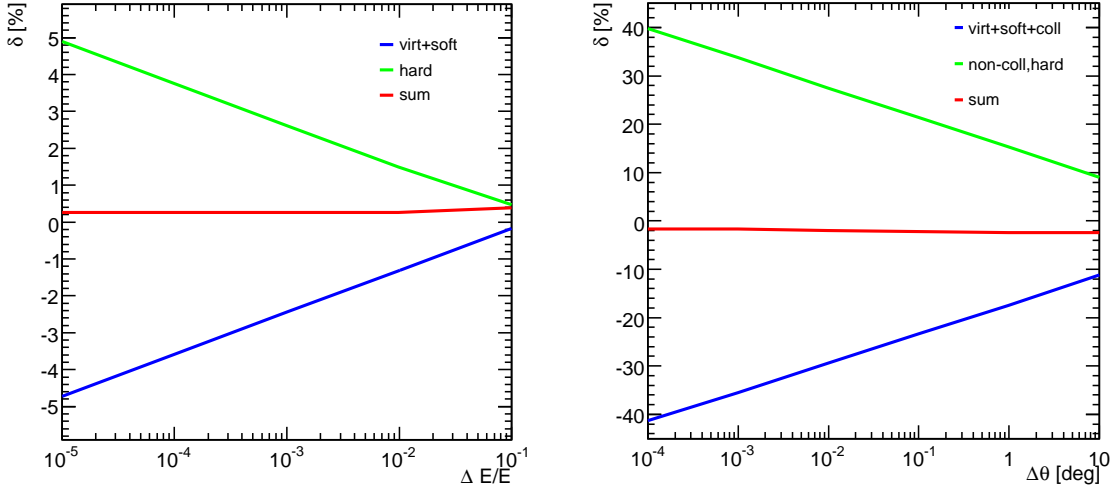
Figure 6.14: Variation of the partial contributions and of the sum of all contributions for different values of the cut-off parameters, ΔE in the gg fusion channel, and $\Delta\delta$ in the $q\bar{q}$ annihilation; at the center-of-mass of the partonic system, $\sqrt{\hat{s}} = 1000$ GeV.

on the angle between the photon and a charged fermion, $\theta_{\gamma f}$, to satisfy the condition $\theta_{\gamma f} < \Delta\theta$. Hence, we can decompose the cross section for the real corrections into the soft, collinear, and finite parts as follows

$$d\hat{\sigma}^a_{real} = d\hat{\sigma}^a_{soft}(\Delta E) + d\hat{\sigma}^a_{coll.}(\Delta E, \Delta\theta) + d\hat{\sigma}^a_{finite}(\Delta E, \Delta\theta)\,, \tag{6.23}$$

where $a = q\bar{q} \to t\bar{t}\gamma$, $gg \to t\bar{t}\gamma$. Note that the collinear contribution is zero in the gg fusion and in the case of the $q\bar{q}$ annihilation, only the initial state radiation contributes, since there are no mass singularities related to the final state bremsstrahlung.

The soft part is combined with the virtual corrections to cancel the IR singularities proportional to $\log\lambda$ and the mass singularities of double logarithms, $\log^2 m_q$. The single logarithms $\log m_q$ are not compensated in the sum of virtual and real corrections and have to be handled by means of factorization (see section 6.5.3).

Single virtual and real contributions obtained within the phase space slicing approach depend on the cut-off parameters ΔE and $\Delta\theta$. If combining all contributions, this dependence must cancel. In order to check the consistency of our results, we examine the dependence of single contributions and of the final result on the cut-off parameters. As shown in Fig. 6.14, this dependence is canceled in the sum of all contributions.

In both singular regions the cross section for the radiative process factorize into the lowest-order cross section and universal factors that contain the singularities. In the case of the $q\bar{q}$ annihilation subprocess, the soft photon bremsstrahlung cross section

can be, as shown e.g. in [78, 126], expressed as

$$
\begin{aligned}
d\hat{\sigma}_{soft} = & -\frac{\alpha}{\pi} d\hat{\sigma}_{Born} \\
\times & \left\{ Q_q^2 \left[2\ln\left(\frac{2\Delta E}{\sqrt{\hat{s}}}\right) + 2\ln\left(\frac{2\Delta E}{\sqrt{\hat{s}}}\right)\ln\left(\frac{m_q^2}{\hat{s}}\right) + \frac{1}{2}\ln^2\left(\frac{m_q^2}{\hat{s}}\right) \right.\right. \\
& \left. + \ln\left(\frac{m_q^2}{\hat{s}}\right) + \frac{\pi^2}{3} \right] \\
& + Q_t^2 \left[2\ln\left(\frac{2\Delta E}{\sqrt{\hat{s}}}\right) + \frac{1}{\beta}\ln\left(\frac{1-\beta}{1+\beta}\right) \right. \\
& + \frac{\hat{s} - 2m_t^2}{\hat{s}\beta} \left[2\ln\left(\frac{2\Delta E}{\sqrt{\hat{s}}}\right)\ln\left(\frac{1-\beta}{1+\beta}\right) \right. \\
& \left.\left. + \frac{1}{2}\ln^2\left(\frac{1-\beta}{1+\beta}\right) + 2\mathrm{Li}_2\left(\frac{2\beta}{1+\beta}\right) \right] \right] \\
& + 2Q_q Q_t \times 3 \left[2\ln\left(\frac{2\Delta E}{\sqrt{\hat{s}}}\right)\ln\left(\frac{m_t^2 - \hat{u}}{m_t^2 - \hat{t}}\right) + \mathrm{Li}_2\left(1 - \frac{\hat{s}(1+\beta)}{2(m_t^2 - \hat{t})}\right) \right. \\
& + \left\{ \mathrm{Li}_2\left(1 - \frac{\hat{s}(1-\beta)}{2(m_t^2 - \hat{t})}\right) - \mathrm{Li}_2\left(1 - \frac{\hat{s}(1+\beta)}{2(m_t^2 - \hat{u})}\right) \right. \\
& \left.\left.\left. - \mathrm{Li}_2\left(1 - \frac{\hat{s}(1-\beta)}{2(m_t^2 - \hat{u})}\right) \right\} \right] \right\},
\end{aligned}
\tag{6.24}
$$

where the relative velocity β is given as $\beta = \sqrt{1 - 4m_t^2/\hat{s}}$, Li_2 denotes the dilogarithm (see appendix D for definition), and the multiplicative factor of 3 in the interference term comes from the sum of photon and gluon radiation contributions. The soft photon factor for the gg fusion can easily be deduced by setting $Q_q = Q_g = 0$.

The cross section for the collinear photon radiation off the initial state $q\bar{q}$ pair, as given e.g. in [129], corresponds to a convolution

$$
\begin{aligned}
d\hat{\sigma}_{coll.}(\hat{s}) = & \frac{Q_q^2 \alpha}{\pi} \int_0^{1 - 2\Delta E/\sqrt{\hat{s}}} dz \, d\hat{\sigma}_{Born}(z\hat{s}) \\
& \times \left\{ \left[\ln\left(\frac{\Delta\theta^2 \hat{s}}{4m_q^2}\right) - 1 \right] P_{q\bar{q}}(z) + (1-z) \right\},
\end{aligned}
\tag{6.25}
$$

with

$$
P_{q\bar{q}}(z) = \frac{1+z^2}{1-z}.
\tag{6.26}
$$

The momentum of the quark that radiates a photon is reduced by the factor z so that the partonic center-of-mass frame of the hard process receives a boost. $P_{q\bar{q}}$ denotes the

splitting function of a photon from a quark or antiquark, and can be determined in analogy to the splitting functions in QCD (see section 5.2.2 and appendix C.1). The integration over all possible reduction fractions z is constrained by the soft cut-off ΔE, to prevent overcounting in the soft region.

6.4.2   Dipole subtraction method

In this work we use the dipole subtraction method which was originally proposed for QCD [130]. We closely follow the formalism worked out in [128] and refer to it for more details.

The idea of the subtraction method is to construct an auxiliary function which contains the same singularities as the real corrections, and subsequently to subtract the auxiliary function from the real contributions. As a result, the integrand becomes finite and can thus be integrated numerically over the whole phase space. The auxiliary function has to be simple enough so that it can be integrated analytically and subsequently added to the virtual contributions. The IR and mass-singular terms in the virtual corrections are then canceled against those in the integrated auxiliary function. The schematic structure of the subtraction approach can be sketched as

$$\int d\Phi_1 \sum_\gamma |M_1|^2 = \int d\Phi_1 \left(\sum_\gamma |M_1|^2 - |M_{\text{sub}}|^2 \right) + \int d\Phi_1 |M_{\text{sub}}|^2 , \qquad (6.27)$$

where $|M_1|^2$ and $|M_{\text{sub}}|^2$ denote the squared matrix elements of the radiative process and the subtraction function, respectively.

The main benefit of the subtraction method is that the integration error is smaller than the corresponding error obtained using the phase space slicing method. In the slicing approach the soft and collinear approximations require the choice of rather small values of the cut-off parameters and the integration error can become very large. The origin of this behaviour is in the integration performed "too close" to the singularity. Typically, the integration error obtained by the application of the dipole subtraction method is smaller by a factor of $10 - 20$ [128]. A comparison of the numerical performance of the subtraction method versus the phase space slicing is given in Tab. 6.1. The best integration results in terms of smallest errors are obtained with the subtraction method. In the phase space slicing approach, the error grows with smaller cut-off parameter. On the other hand, larger cut-off parameters are not suitable for the calculations since the approximation is no longer reliable.

The disadvantage of the subtraction method is in the treatment of non-inclusive quantities. Here the subtraction function which was used for the inclusive calculations

Table 6.1: Comparison of the numerical results for the relative QED corrections in the gg fusion channel, as obtained with the phase space slicing method and the dipole subtraction approach, for various partonic center-of-mass energies $\sqrt{\hat{s}} = 2E$. ΔE denotes the soft cut-off parameter.

$\sqrt{\hat{s}}$	Method	$\Delta E/E$	δ_{QED} [%]
360	Phase space slicing	10^{-2}	2.5483 ± 0.0014
		10^{-3}	2.5415 ± 0.0014
		10^{-4}	2.5407 ± 0.0014
	Dipole subtraction	—	2.5410 ± 0.0014
500	Phase space slicing	10^{-2}	0.35816 ± 0.00037
		10^{-3}	0.34882 ± 0.00061
		10^{-4}	0.3478 ± 0.0011
	Dipole subtraction	—	0.34817 ± 0.00022
1000	Phase space slicing	10^{-2}	0.1254 ± 0.0014
		10^{-3}	0.1121 ± 0.0025
		10^{-4}	0.1107 ± 0.0037
	Dipole subtraction	—	0.11115 ± 0.00020
2000	Phase space slicing	10^{-2}	0.1943 ± 0.0023
		10^{-3}	0.1763 ± 0.0043
		10^{-4}	0.1752 ± 0.0064
	Dipole subtraction	—	0.17472 ± 0.00035

is not suitable anymore and has to replaced by a new function. This difficulty does not arise in the phase space slicing approach and therefore, in the non-inclusive studies we used the phase space slicing method alone.

6.5 Hadronic cross sections for $pp/p\overline{p} \to t\overline{t}X$

In order to provide results independent of the detector setup, we calculate the total as well as differential hadronic cross sections inclusively in the photon, i.e. we add up contributions of the non-radiative and radiative processes. As already mentioned, only the sum of all virtual and real corrections is independent on the cut-off parameters. Therefore, for exclusive calculations we would have to tune the results for specific detector parameters of energy and angular resolution, which would limit the application of our results to a specific detector only. The calculation of the total hadronic cross

section can be performed using *FormCalc* where the parton densities are provided via the Les Houches Accord (LHA) library. Before the numerical results can be evaluated, the factorization of the remaining mass singularities has to be worked out. For this reason, we have extended *FormCalc* to handle the mass factorization.

6.5.1 Integrated hadronic cross sections

The observable hadronic cross section is obtained by convoluting the short distance partonic cross sections $\hat{\sigma}_{gg}$ and $\hat{\sigma}_{q\overline{q}}$ with the universal scale dependent parton distribution functions (PDFs). For hadrons carrying the momentum P_1 and P_2 with the center-of-mass (CM) energy squared equal to $S = (P_1 + P_2)^2$, the hadronic cross section can be expressed as [80]

$$\sigma(S) = \int_{\frac{4m_t^2}{S}}^{1} d\tau \left(\frac{d\mathcal{L}_{q\overline{q}}}{d\tau} \, \hat{\sigma}_{q\overline{q}}(\hat{s}, \alpha_s(\mu)) + \frac{d\mathcal{L}_{gg}}{d\tau} \, \hat{\sigma}_{gg}(\hat{s}, \alpha_s(\mu)) \right) \, , \qquad (6.28)$$

with $\tau = x_1 x_2 = \hat{s}/S$, where x_1 and x_2 are the momentum fractions of partons within the hadrons, and $\hat{s}$ is the partonic center-of-mass energy, $\sqrt{\hat{s}} = \sqrt{\tau S}$. Masses of the partons as well as of the hadrons are neglected with respect to the CM energies. The parton luminosities are defined as follows,

$$\frac{d\mathcal{L}_{ij}}{d\tau} = \frac{1}{1 + \delta_{ij}} \int_{\tau}^{1} \frac{dx_1}{x_1} \left[\Phi_i(x_1, \mu_f)\Phi_j(\frac{\tau}{x_1}, \mu_f) + (1 \leftrightarrow 2) \right] \, , \qquad (6.29)$$

with $\Phi_i = q_i, g$. The factorisation scale, μ_f, and the renormalization scale, μ, are chosen to be equal and set to $\mu_f = \mu = 2m_t$.

Expressions analogous to Eqs. (6.28), (6.29), also apply to the gluon–photon hadronic process.

6.5.2 Differential hadronic cross sections

In addition to the fully integrated hadronic cross section it is plausible to define hadronic cross sections differential in one or more parameters. Typically, the variables are chosen to be Lorentz invariant quantities or quanitities with simple transformation properties. In our study we inspect the differential hadronic cross sections with respect to the invariant mass of the final state $t\overline{t}$ pair and with respect to the transverse momentum of top quark.

The invariant mass of a process is equivalent to the partonic CM energy $\sqrt{\hat{s}} = \sqrt{\tau S}$, and corresponds to the sum of the momenta of the outgoing particles. The invariant

mass distribution of the hadronic cross section has the following form:

$$\frac{d\sigma_{pp\to fin}}{d\sqrt{\hat{s}}} = 4\pi \frac{\sqrt{\hat{s}}}{S} \sum_{\{m,n\}} \frac{d\mathcal{L}}{d\tau}\bigg|_{\tau=\frac{\hat{s}}{S}} \hat{\sigma}_{mn\to fin} , \tag{6.30}$$

where fin is label of a general partonic final state, and mn denotes the initial state partons.

The differential hadronic cross section with respect to the transverse momentum of one of the final state particles (top quark in this case), $p_{\mathrm{T}} = \sqrt{p_x^2 + p_y^2}$, can be defined for a $2 \to 2$ process as follows,

$$\frac{d\sigma}{dp_{\mathrm{T}}} = \int_{\tilde{\tau}_0}^1 d\tau \frac{d\mathcal{L}}{d\tau} \frac{d\hat{\sigma}}{dc_{\tilde{\theta}}} \frac{\partial c_{\tilde{\theta}}}{\partial p_{\mathrm{T}}} , \tag{6.31}$$

with $c_{\tilde{\theta}}$ denoting cosine of the angle between the direction of the top quark and the beam axis. The lower limit on the τ-integration $\tilde{\tau}_0$ corresponds to the threshold of the partonic interaction, and therefore must be adjusted according to the respective p_{T} as

$$\tilde{\tau}_0 = \frac{\left(\sqrt{m_1^2 + p_{\mathrm{T}}^2} + \sqrt{m_2^2 + p_{\mathrm{T}}^2}\right)^2}{S} , \tag{6.32}$$

where f_1 and f_2 stand for the two final state particles with the respective masses m_1 and m_2, which both have the same p_{T} as a consequence of the momentum conservation and Lorentz invariance.

Real photonic corrections are three-particle final state processes. Therefore, we also need expression for the differential hadronic cross section with respect to the transverse momentum of one of the final state particles (top quark), for a $2 \to 3$ process:

$$\frac{d\sigma}{dp_{\mathrm{T}}} = \int_{\tilde{\tau}_0}^1 d\tau \frac{d\mathcal{L}}{d\tau} \int dk_1^0 \int dk_3^0 \int d\tilde{\eta} \frac{d\hat{\sigma}}{dk_1^0 dk_3^0 d\tilde{\eta} dc_{\tilde{\theta}}} \frac{\partial c_{\tilde{\theta}}}{\partial p_{\mathrm{T}}} , \tag{6.33}$$

where k_1^0 and k_3^0 denote energies of the two independent final state particles (the momentum of the third particle is not independent, but is fixed by the momentum conservation), $c_{\tilde{\theta}}$ is cosine of the angle between the direction of $\vec{k}_1$ and the beam axis. $\tilde{\eta}$ is the angle between the projection of $\vec{k}_3$ into the plan formed by $\vec{k}_1$ and axis, which is perpendicular to $\vec{k}_1$ and to the beam direction, and this axis. The threshold of the $2 \to 3$ partonic interaction, determined with respect to particle f_1, corresponds to

$$\tilde{\tau}_0 = \frac{\left(\sqrt{m_1^2 + p_{\mathrm{T}}^2} + \sqrt{(m_2 + m_3)^2 + p_{\mathrm{T}}^2}\right)^2}{S} . \tag{6.34}$$

Here m_3 corresponds to the photon mass, which is zero. For a consistent treatment in case of the IR-singular processes it has to be replaced by the soft cut-off parameter.

6.5.3   Mass factorization

The mass-singular logarithmic terms proportional to $\ln m_q$ are not canceled in the sum of virtual and real corrections. They originate from collinear photon emission off the incoming light quarks. In analogy to the factorization of collinear gluon contributions, they have to be absorbed into the parton densities (see section 5.2).

This can be formally achieved by replacing the bare quark distributions $q(x)$ by the appropriate scale dependent distributions $q(x, Q^2)$ according to [131] in the following way,

$$
\begin{aligned}
q_i(x, Q^2) \;=\; & q_i(x) \\
& + \frac{\alpha}{\pi} Q_i^2 q_i(x) \left\{ 1 - \ln \delta_s - \ln^2 \delta_s + \left(\ln \delta_s + \frac{3}{4} \right) \ln \left(\frac{Q^2}{m_i^2} \right) \right. \\
& \left. - \frac{1}{4} \lambda_{FC} f_{v+s} \right\} \\
& + \int_x^{1-\delta_s} \frac{dz}{z} q_i \left(\frac{x}{z} \right) \frac{\alpha}{2\pi} Q_i^2 \left\{ \frac{1+z^2}{1-z} \ln \left(\frac{Q^2}{m_i^2} \frac{1}{(1-z)^2} \right) \right. \\
& \left. - \frac{1+z^2}{1-z} + \lambda_{FC} f_c \right\} ,
\end{aligned}
\tag{6.35}
$$

with

$$
f_{v+s} = 9 + \frac{2\pi^2}{3} + 3 \ln \delta_s - 2 \ln^2 \delta_s \; ,
\tag{6.36}
$$

and

$$
f_c = \frac{1+z^2}{1-z} \ln \left(\frac{1-z}{z} \right) - \frac{3}{2(1-z)} + 2z + 3 \; .
\tag{6.37}
$$

The expressions for the PDFs are given in both DIS and $\overline{\text{MS}}$ factorization schemes, which corresponds to $\lambda_{FC} = 1$ and $\lambda_{FC} = 0$, respectively.

For a consistent treatment of the collinear singularities at $\mathcal{O}(\alpha)$, it is necessary to use an appropriate set of PDFs that was extracted from the data and evolved by DGLAP equations with the NLO QED effects included. Otherwise, it would lead to an overestimation of the scale dependence. Therefore, we used the PDFs from the MRST collaboration [92] which were determined at NLO QCD and NLO QED (see section 5.3). The authors do not explicitly state which factorization scheme is relevant for NLO QED. We follow the reasonning given in [132] and use the DIS scheme in our calculation and set the scale $Q = \mu_f = \mu = 2m_t$.

After performing the factorization of mass singularities, the results become free of the mass logarithms, proportional to $\ln m_q$, which we checked numerically. Still, the scale dependence cannot be checked in a consistent way owing to the NLO QCD effects in the parton densities, as these are not included in our calculation. For this reason we do not present a study of the scale dependence.

6.6   Numerical results

In the following we discuss numerical results for the total hadronic cross sections, as well as for the differential hadronic cross sections with respect to the invariant mass of the $t\bar{t}$ pair and the transverse momentum of the top quark.

In order to provide a result independent of the detector setup, we treat the photon inclusively, i.e. we integrate over the whole photon phase space. The IR singularities are handled by means of the phase space slicing method. In the $q\bar{q}$ annihilation channel, effects of the initial state radiation are included with factorization of the mass singularities, as discussed in the previous section. The partonic cross sections are convoluted with the NLO QED PDF set, provided by the MRST group [92] and the factorization and renormalization scales are set to $\mu_f = \mu = 2m_t$.

To investigate the numerical impact of the NLO QED corrections on the total hadronic top pair production cross section we introduce a relative correction δ, defined as

$$\delta = \frac{\sigma_{\text{1-loop}}(S) - \sigma_B(S)}{\sigma_B(S)} \, , \tag{6.38}$$

where S is the total energy of the hadronic system, (2 TeV at the Tevatron and 14 TeV at the LHC). As the one-loop cross section can be written as

$$\sigma_{\text{1-loop}}(S) = \sigma_B(S) + \delta\sigma(S) \, , \tag{6.39}$$

the relative correction δ is given as the ratio of the sum of $\mathcal{O}(\alpha\alpha_{\text{s}}^2)$ contributions $\delta\sigma(S)$, and the Born-level cross section σ_B.

We also use δ to inspect the effects of NLO QED corrections on the differential hadronic cross sections. For this purpose, we redefine the Eq. (6.38) by substituting the total cross sections σ by the differential cross sections $d\sigma$. In this way we obtain variations of δ as a function of the total partonic energy, equivalent to the invariant mass of the $t\bar{t}$ pair, and of the transverse momentum of the top quark.

In order to avoid numerical instabilities related to the $t\bar{t}$ production threshold we introduce kinematical cuts on the top quark system. These are necessary for the

identification of $t\bar{t}$ pairs in experiment and are used in the event reconstruction. As the top quarks have a very short lifetime, they decay practically immediately and can only be identified and reconstructed via their decay products. Typically, the top decay products have large transverse momenta and this fact is used as event selection criterium, as imposing a transverse momentum cut reduces the background originating from other QCD processes.

Also the detector setup gives constraints on the data analysis. Particles can only be reconstructed in certain angular regions around the interaction point according to the detector geometry. For convenience, a spatial coordinate describing the angle of a particle relative to the beam axis, the pseudorapidity η, is used to describe the detector geometry. It is defined as

$$\eta = -\ln\left[\tan\left(\frac{\theta}{2}\right)\right] , \tag{6.40}$$

where θ is the angle relative to the beam axis. In the limit of ultra-relativistic hadrons and partons, η is the same as the rapidity y:

$$y = \frac{1}{2}\ln\frac{p^0 + p_L}{p^0 - p_L} \tag{6.41}$$

defined in the center-of-mass (CM) frame of a particle with momentum p, energy p^0, and longitudinal momentum p_L, parallel to the beam axis. The rapidity has an additive character under Lorentz transformations and receives a Lorentz boost from the hadronic to the partonic CM frame:

$$y_H \rightarrow y_P = y_H - y_{\text{boost}} . \tag{6.42}$$

Using the ultrarelativistic approximation, we can deduce that

$$y_{\text{boost}} = \frac{1}{2}\log\frac{x^2}{\tau} , \tag{6.43}$$

with x being the momentum fraction of the parton from the corresponding hadron and τ being the ratio of total energies of the partonic and hadronic systems.

In order to match the experimental conditions we introduce constraints on the transverse momentum p_T and on the pseudorapidity η of the top quark and top anti-quark, and study the impact on the NLO QED corrections. Since we do not include the top quark decay in our calculations, we choose p_T for the top quark to correspond to p_T of the total system of decay products. In the case of LHC we apply kinematical cuts as follows,

$$p_T > 100 \text{ GeV} \quad \text{and} \quad |\eta| < 2.5 . \tag{6.44}$$

Table 6.2: Total hadronic cross section for $t\bar{t}$ production at NLO QED at the LHC in different production subprocesses without and with the cuts. The relative precision of the corrections achieved in the numerical integration is 10^{-3}.

Process	σ_{tot} without cuts [pb]		σ_{tot} with cuts [pb]	
	Born	correction	Born	correction
$u\bar{u}$	34.25	-1.41	18.64	-0.770
$d\bar{d}$	21.61	-0.228	11.54	-1.68
$s\bar{s}$	4.682	-0.0410	2.253	-0.0304
$c\bar{c}$	2.075	-0.0762	0.9630	-0.0446
gg	407.8	2.08	213.6	0.524
$g\gamma$		4.45		2.29
pp	470.4	4.78	247.0	1.80

For the Tevatron, the cuts are

$$p_{\text{T}} >\ 25\,\text{GeV} \quad \text{and} \quad |\eta| < 2.5\,. \tag{6.45}$$

Concerning the hard, non-collinear bremsstrahlung, it is possible to construct more elaborate selection criteria, e.g. to combine the photon with one of the top quarks and impose cuts on this system. Nevertheless, we have found that the impact on the relative corrections is small, since only the hard part of the NLO contributions is slightly modified. Therefore we do not consider such criteria in our analysis.

In Tabs. 6.2, and 6.3, we present the numerical results for the total hadronic cross sections at the LHC and at the Tevatron, respectively. The values of σ_{tot} are given at the Born-level and for the NLO QED corrections. They are obtained with the relative accuracy of 10^{-3}. The contributions of all production channels are shown separately, as well as combined to the total correction.

At the LHC, the largest correction comes from the photon–gluon production channel which contributes at NLO. It has the same sign as the contribution to the gg fusion which is the dominant $t\bar{t}$ production channel at the LHC. However, in case of the $q\bar{q}$ annihilation, the corrections have opposite signs which leads to a reduction of the overall NLO QED correction. In total, the relative correction δ is about 1% and is slightly reduced if the cuts are applied.

At the Tevatron, the largest contributions to the total hadronic cross section come from the $u\bar{u}$ subprocess. The photon–gluon subprocess yields the second largest con-

Table 6.3: Total hadronic cross section for $t\bar{t}$ production at NLO QED at the Tevatron in different production subprocesses without and with the cuts. The relative precision of the corrections achieved in the numerical integration is 10^{-3}.

Process	σ_{tot} without cuts [pb]		σ_{tot} with cuts [pb]	
	Born	correction	Born	correction
$u\bar{u}$	3.411	-0.117	3.189	-0.118
$d\bar{d}$	0.5855	-2.89×10^{-3}	0.5432	-2.91×10^{-3}
$s\bar{s}$	8.063×10^{-3}	-1.21×10^{-5}	7.343×10^{-3}	-1.79×10^{-5}
$c\bar{c}$	2.044×10^{-3}	-5.06×10^{-5}	1.857×10^{-3}	-5.00×10^{-5}
gg	0.4128	3.17×10^{-3}	0.3803	2.69×10^{-3}
$g\gamma$		0.0154		0.0143
$p\bar{p}$	4.420	-0.102	4.121	-0.104

tribution but with opposite sign. In total, the relative correction δ is about 2.3% and is slightly enhanced by the cuts to 2.5%.

From now on, we focus on the differential hadronic cross sections. In Fig. 6.15 the p_T and $\sqrt{\hat{s}}$ distributions of the differential hadronic cross sections are shown (left), as well as the relative QED corrections with respect to the Born-level cross sections (right), at the LHC. Here we compare the two production channels, which contribute at the Born-level without applying the cuts. The gg fusion contribution dominates over the $q\bar{q}$ channel, owing to large gluon densities at low x, which is characteristic for the top quark production at the LHC energies.

The impact of the NLO QED corrections on the gg fusion channel is rather small less than 1% over most of the p_T range (up right) and also over most of the $\sqrt{\hat{s}}$ range (down, right). The relative correction δ reaches above 1% only close to the production threshold, which is a direct consequence of the threshold effects. In contrast to the gg channel, the $\mathcal{O}(\alpha\alpha_\text{s}^2)$ contributions in the $q\bar{q}$ annihilation subprocess are negative and much larger. The relative correction δ grows with increasing p_T and $\sqrt{\hat{s}}$ and gets to the 5% level for $p_\text{T} \gtrsim 400$ GeV and $\sqrt{\hat{s}} \gtrsim 1200$ GeV.

In case of the Tevatron, as shown in Fig. 6.16, the $q\bar{q}$ annihilation dominates over the gg fusion (left). The impact of $\mathcal{O}(\alpha\alpha_\text{s}^2)$ corrections on both channels is similar to the LHC. Again, in the gg fusion, the relative correction δ is smaller than 1% for most of the p_T and $\sqrt{\hat{s}}$ ranges, except for the low p_T and threshold regions where it reaches about 2% (up right). In the $q\bar{q}$ annihilation channel, the relative corrections
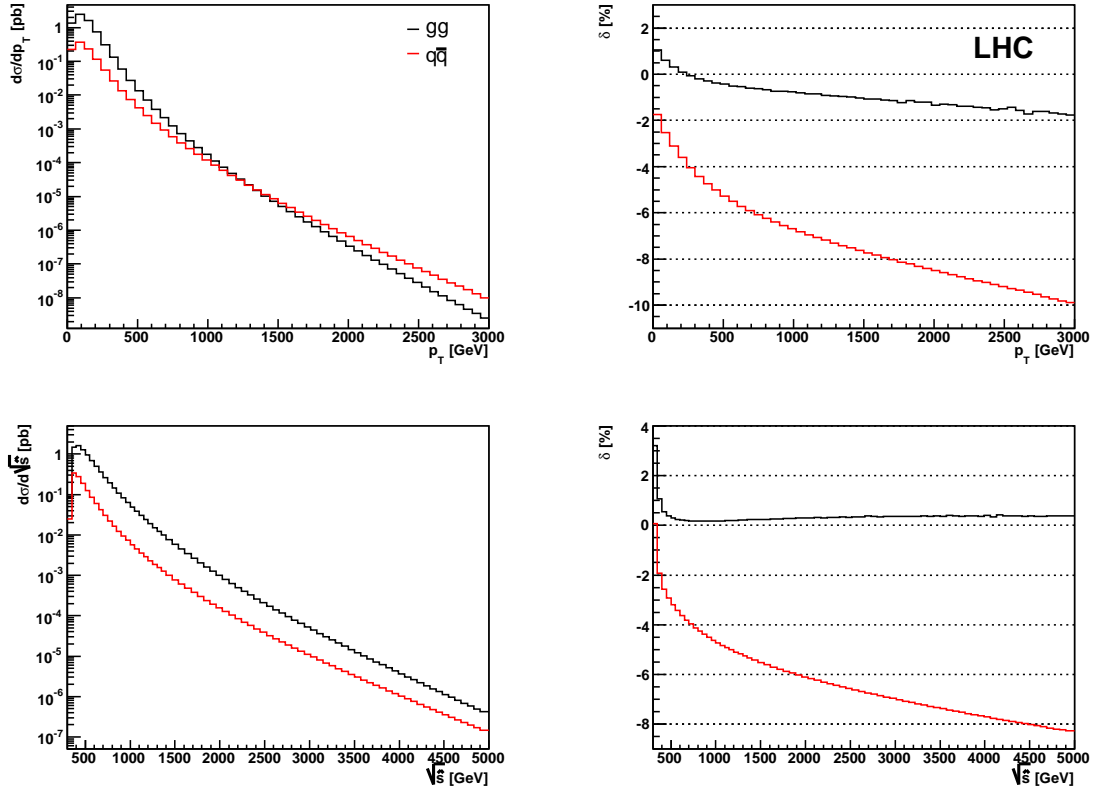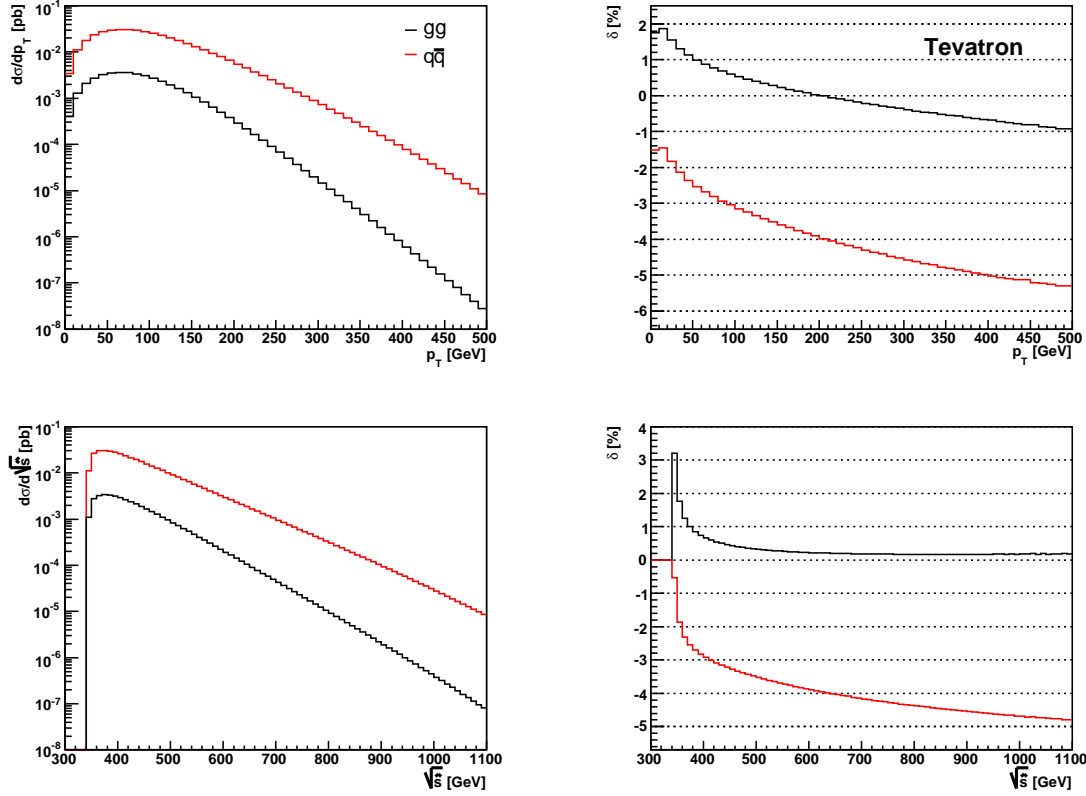
Figure 6.15: Differential hadronic cross sections (left), and variation of the relative correction δ (right), as functions of the transverse momentum of the top quark (up) and of the total energy of the partonic system (down), at the LHC ($S = 14$ TeV), with no cuts applied, for both production channels.

are negative and at a few per cent level already near the threshold. They grow futher with increasing p_T and $\sqrt{\hat{s}}$.

Figures 6.17 and 6.18 show the impact of applying the cuts on both production channels at the LHC and at the Tevatron, respectively. At the LHC, the cuts slightly reduce the differential cross sections as well as the relative corrections but these effects are very small over most of the p_T and $\sqrt{\hat{s}}$ ranges. A sizeable reduction is only visible near the threshold where the relatively large contributions related to threshold effects are removed.

At the Tevatron, imposing the relatively weak cut on the transverse momentum does not change the distributions of the differential hadronic cross section at one-loop significantly (Fig. 6.18 left). In the gg fusion, the impact of the cuts on the relative corrections (Fig. 6.18 up right) is only visible in the low p_T and threshold regions, similarly as for the LHC, but here the reduction is smaller because of smaller p_T cut.

Figure 6.16: Differential hadronic cross sections (left), and variation of the relative correction δ (right), as functions of the transverse momentum of the top quark (up) and of the total energy of the partonic system (down), at the Tevatron ($S = 2$ TeV), with no cuts applied, for both production channels.

Much more interesting observation can be done in the $q\overline{q}$ annihilation case (Fig. 6.18 down right), where applying the cuts increases the size of relative corrections in the low p_{T} region to almost 3%. We can therefore deduce that the cuts reduce the Born-level cross section more than the NLO QED contributions. The relative corrections are negative and reach about 5% for $p_{\mathrm{T}} \gtrsim 350$ GeV and $\sqrt{\hat{s}} \gtrsim 800$ GeV. They further grow with increasing p_{T} and $\sqrt{\hat{s}}$.

As previously discussed, also the photon-induced hadronic processes represent contributions of NLO in QED, owing to higher order effects included in the PDFs. In Figs. 6.19 and 6.20, we therefore include the photon–gluon $t\overline{t}$ production subprocess into our analysis and compare the numerical results with the gg and $q\overline{q}$ production channels. This is done for the LHC as well as for the Tevatron.

We can see that at the LHC (Fig. 6.19), the photon-induced contributions are larger than the corrections to both Born-level processes. This is due to the fact that the partonic cross section for the $\mathcal{O}(\alpha\alpha_{\mathrm{s}}^2)$ corrections is reduced by a factor of $\mathcal{O}(\alpha_{\mathrm{s}})$
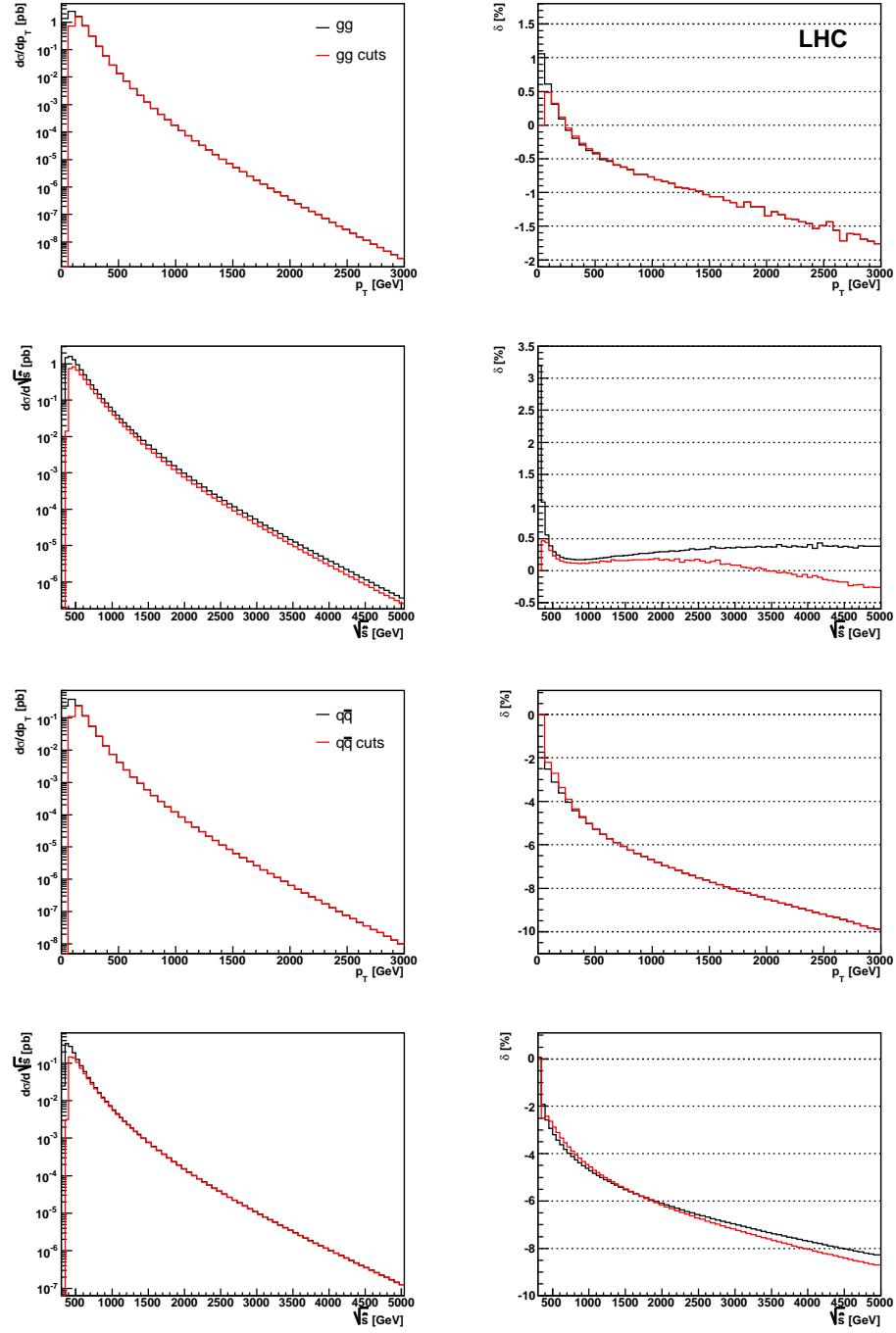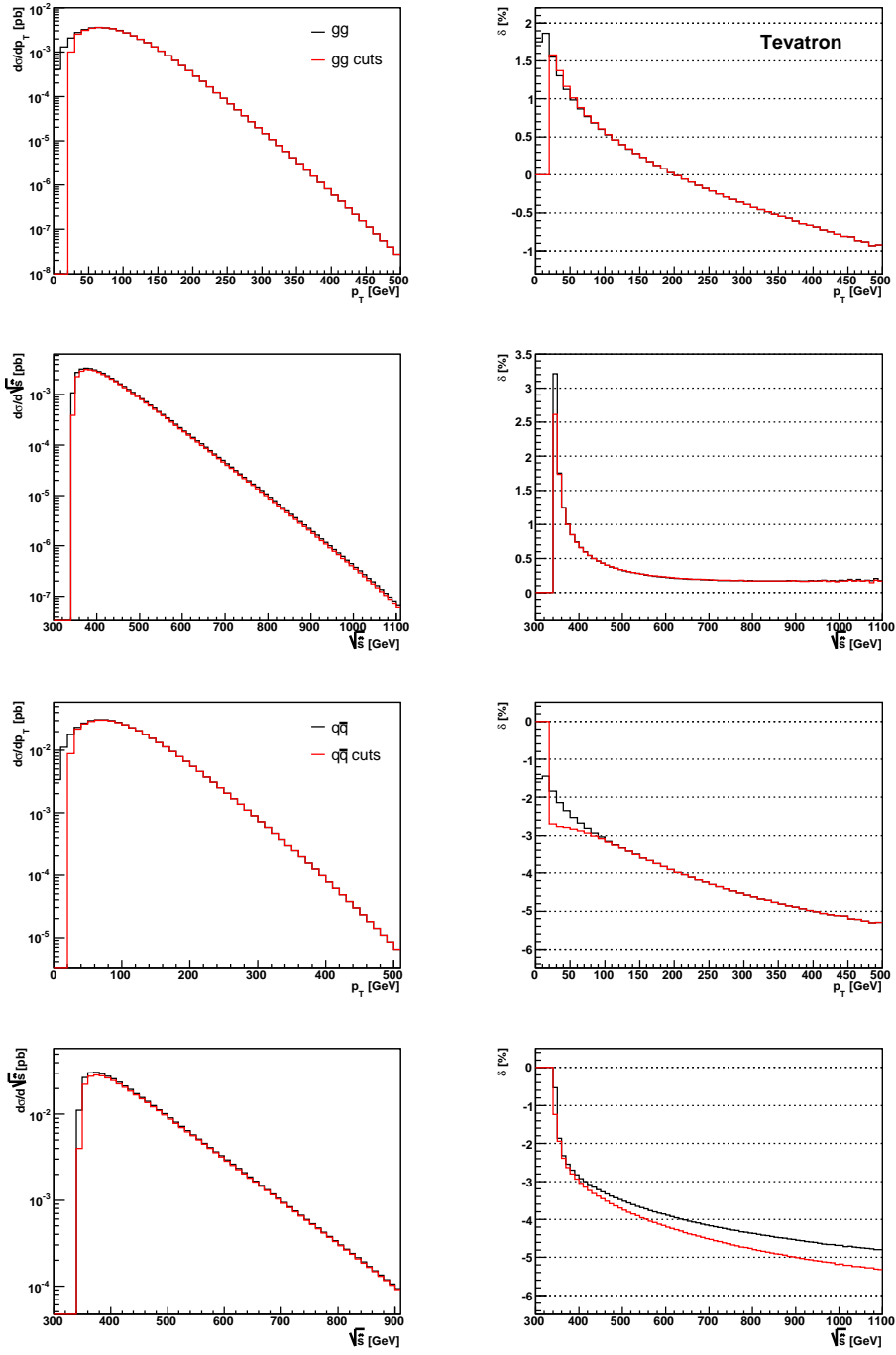
Figure 6.17: Differential hadronic cross sections (left) and relative correction δ (right), as functions of the transverse momentum of the top quark (1st and 3rd row), and of the total partonic energy (2nd and 4th row), at the LHC ($S = 14$ TeV). The gg fusion and $q\bar{q}$ annihilation channels are investigated separately. The impact of cuts on the transverse momentum and on the pseudorapidity of the top quarks, $p_T > 100$ GeV and $|\eta| < 2.5$, is also shown.
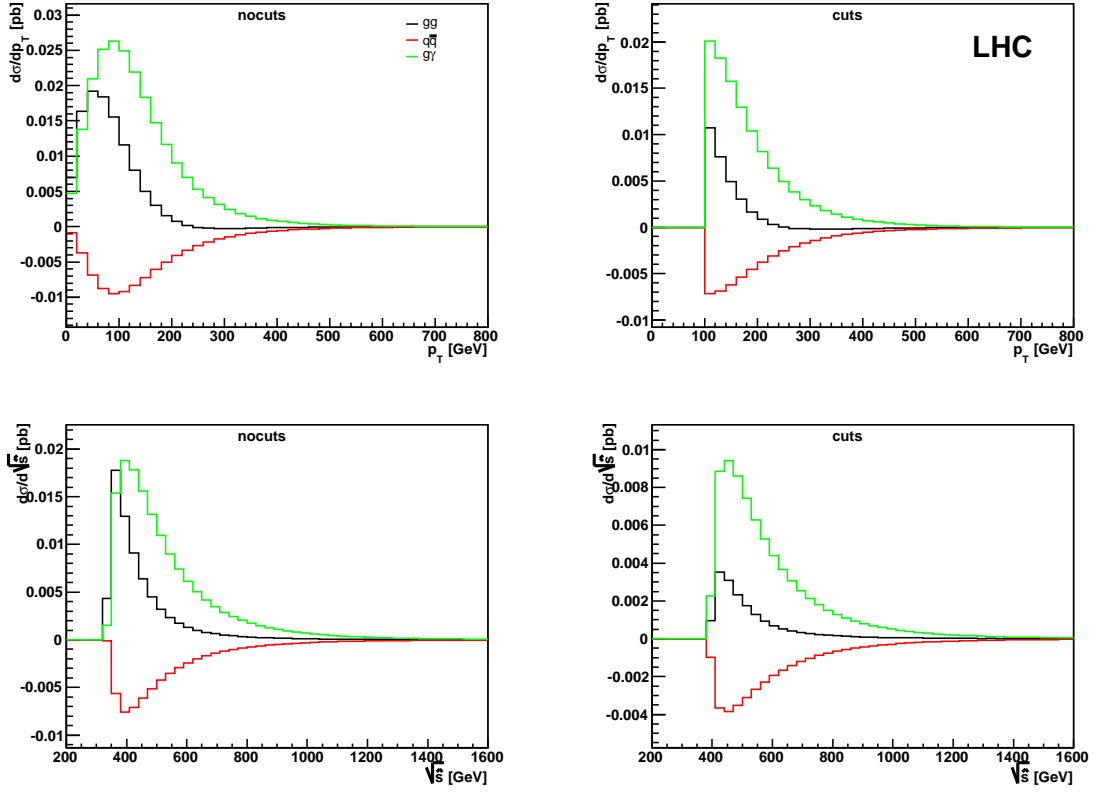
Figure 6.18: Differential hadronic cross sections (left) and relative correction δ (right), as functions of the transverse momentum of the top quark (1st and 3rd row), and of the total partonic energy (2nd and 4th row), at the Tevatron ($S = 2$ TeV). The gg fusion and $q\bar{q}$ annihilation channels are investigated separately. The impact of cuts on the transverse momentum and on the pseudorapidity of the top quarks, $p_T > 25$ GeV and $|\eta| < 2.5$, is also shown.

Figure 6.19: NLO QED effects in the gg, $q\bar{q}$ and $g\gamma$ production channels at the LHC ($S = 14$ TeV). Differential hadronic cross sections for the NLO QED contributions with respect to the transverse momentum of the top quark (up), and with respect to the total partonic energy (down), are shown, without and with applying the cuts.

with respect to the $\mathcal{O}(\alpha\alpha_s)$ tree-level process, and moreover, the combination of gluon and photon parton densities can become quite large. As the sign of $g\gamma$ hadronic cross section is the same as the sign of the NLO QED contributions to the gg fusion channel, this tends to enhance the size of the overall NLO QED contributions. The $\mathcal{O}(\alpha\alpha_s^2)$ corrections to the $q\bar{q}$ channel are negative and thus tend to reduce the size of overall corrections. Applying cuts just slightly reduces contributions from the $q\bar{q}$ channel as well as from the photon–gluon channel, whereas in the gg case, the reduction is much bigger. It is clearly visible that after applying the cuts, the photon–gluon channel becomes the largest NLO QED contribution.

The situation is different at the Tevatron (Fig. 6.20). Due to dominant parton densities of valence quarks, the $q\bar{q}$ annihilation channel is much larger than the other two. Still, the photon-induced contribution is larger in size than the NLO QED corrections to the gg fusion channel. However, as a consequence of opposite signs, these two tend to reduce the contribution from the $q\bar{q}$ channel. As already observed in Fig. 6.18,
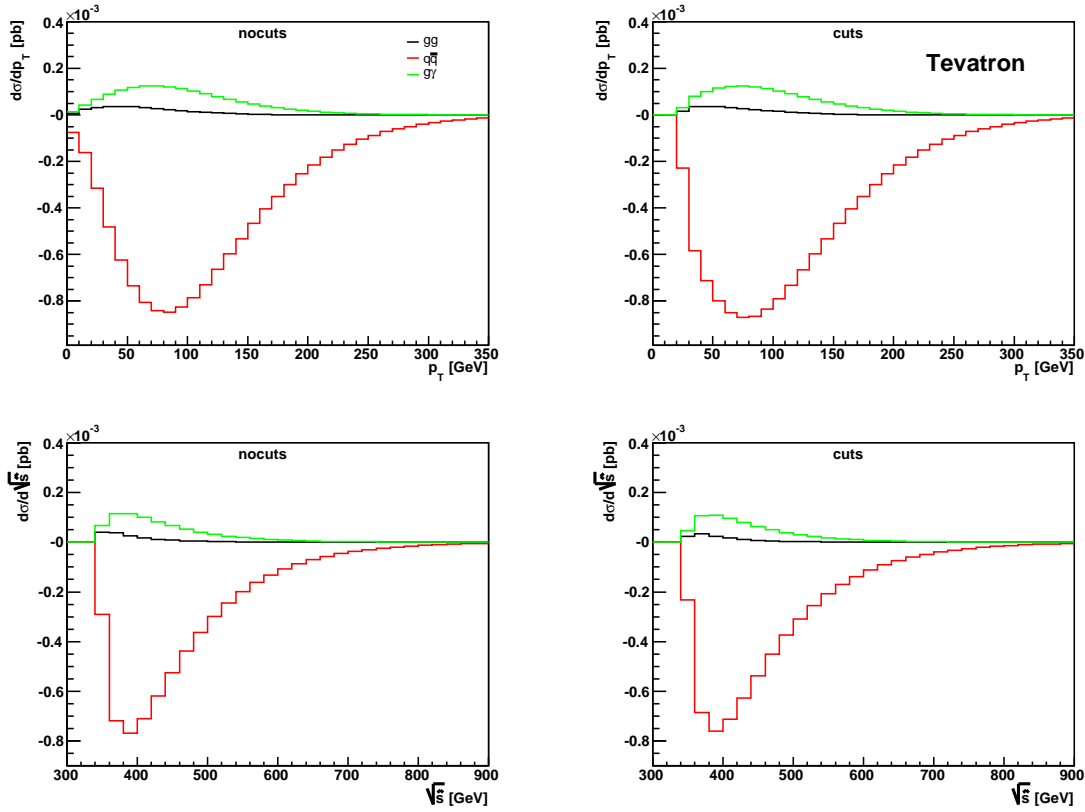
Figure 6.20: NLO QED effects in the gg, $q\bar{q}$ and $g\gamma$ production channels at the Tevatron ($S = 2$ TeV). Differential hadronic cross sections for the NLO QED contributions with respect to the transverse momentum of the top quark (up), and with respect to the total partonic energy (down), are shown, without and with applying the cuts.

applying the cuts slightly enhance the $q\bar{q}$ contribution, whereas it has almost no effect on the other two channels.

The combination of partial results for all production subprocesses, including the photon–gluon channel, is shown in Fig. 6.21 for the pp collisions at the LHC. As a consequence of the dominant gg production channel, the overall relative NLO QED corrections are positive and rather small in the low p_{T} region and over a large $\sqrt{\hat{s}}$ range. For large p_{T}, which corresponds to high x, the $q\bar{q}$ channel becomes important. This makes the relative correction negative and further increasing in size. The photon-induced contribution enhances the overall corrections for low p_{T} and low $\sqrt{\hat{s}}$, but the enhancement is only of about 0.5%. Once the corrections become negative, this slight enhancement changes to a slight reduction. Applying the cuts excludes large portions of the low p_{T} and threshold regions, where the corrections were quite large. In the p_{T} and $\sqrt{\hat{s}}$ ranges shown in Fig. 6.21, the relative corrections remain very small, about 1%. Nevertheless, the behavior of the p_{T} distribution indicates that for extremely high
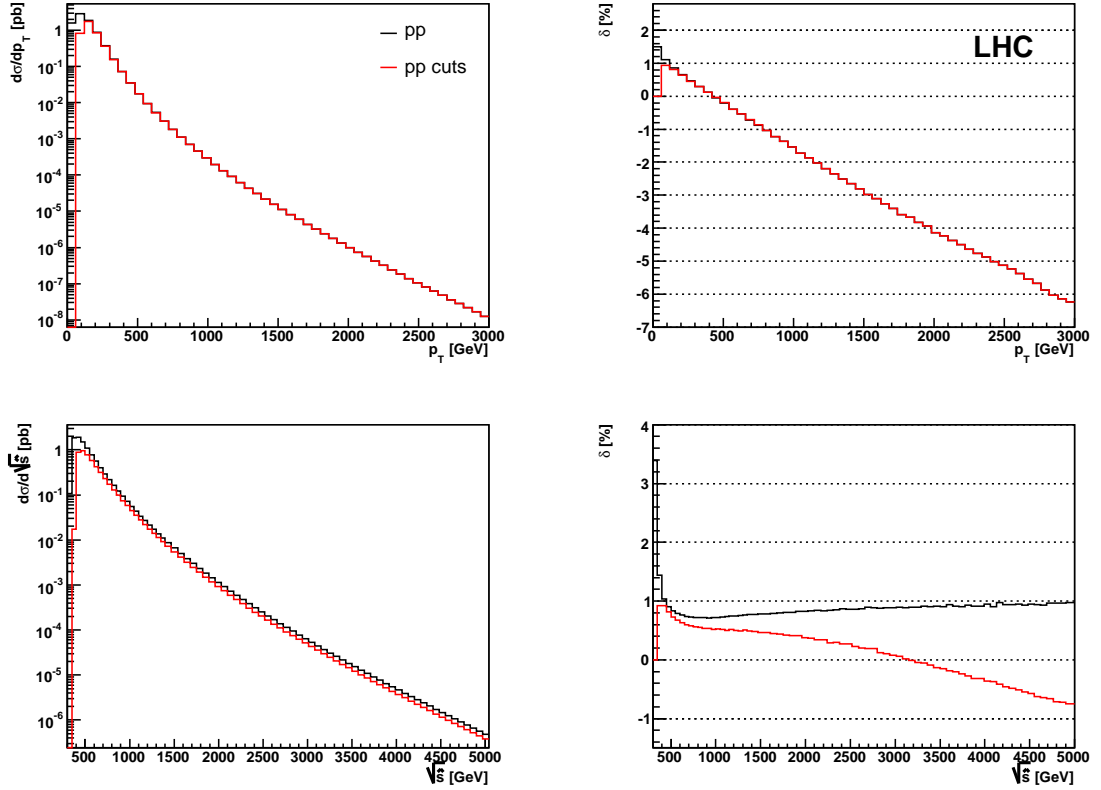
Figure 6.21: Overall NLO QED effects in the *pp* collisions at the LHC ($S = 14$ TeV). Differential hadronic cross sections with respect to the transverse momentum of the top quark (up), and with respect to the total partonic energy (down), are shown, without and with applying the cuts.

p_{T} range the relative correction reaches several per cent. We will come back to this point at the end of this section.

In Fig. 6.22 we show the overall NLO QED effects on the $p\bar{p} \to t\bar{t}X$ process at the Tevatron. Again, the results are obtained by combining all production subprocesses. In this case, the photon–gluon contribution slightly reduces the overall corrections as a result of opposite sign of the dominant $q\bar{q}$ channel contributions. However, applying the cuts enhances the size of relative correction δ in the low p_{T} region. This enhancement is also manifested in the $\sqrt{\hat{s}}$ distribution and becomes larger with increasing $\sqrt{\hat{s}}$. The overall NLO QED relative corrections with all $\mathcal{O}(\alpha\alpha_{\mathrm{s}}^2)$ and $\mathcal{O}(\alpha\alpha_{\mathrm{s}})$ contributions are negative with size about 2% for low p_{T} and low $\sqrt{\hat{s}}$. They further grow in size with increasing p_{T} and $\sqrt{\hat{s}}$ and reach up to 4% for $p_{\mathrm{T}} \gtrsim 250$ GeV and about 5% for $\sqrt{\hat{s}} \gtrsim 800$ GeV.

As seen on previous plots, the QED corrections have a much larger impact on the $q\bar{q}$ annihilation channel owing to subtleties of the QED–QCD interference, which is not
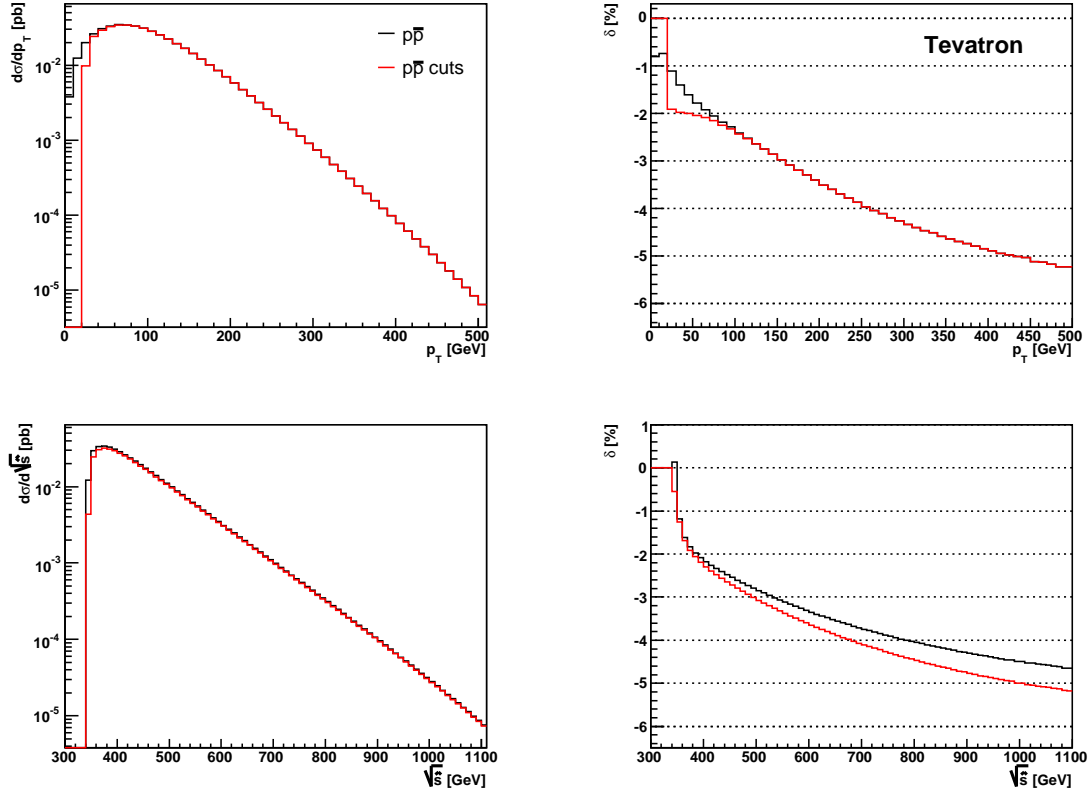
Figure 6.22: Overall NLO QED effects in the $p\overline{p}$ collisions at the Tevatron ($S = 2$ TeV). Differential hadronic cross sections with respect to the transverse momentum of the top quark (up), and with respect to the total partonic energy (down), are shown, without and with applying the cuts.

present in the Born-level result. Also the initial state radiation contributes with terms proportional to $\ln\left(\mu^2/\hat{s}\right)$, which result from the factorization of mass singularities. Moreover, the NLO QED effects lead to the non-zero photon-induced $t\bar{t}$ production contribution which is comparable in size with the rest of the NLO QED corrections.

The NLO QED contributions form together with the non-photonic EW corrections a complete set of the full EW effects at one-loop level. The numerical studies of the non-photonic EW corrections in [106, 108] show that the impact on the total cross section is negligible, which is consistent with our findings. The NLO non-photonic EW effects in p_{T} and invariant mass distributions of the differential cross section were examined in [109–111]. At the LHC, the non-photonic EW corrections are negative and very small near threshold. They grow in size with increasing $\sqrt{\hat{s}}$ and p_{T} and reach 10% level for very high values of p_{T} and $\sqrt{\hat{s}}$ ($p_{\mathrm{T}} \gtrsim 800$ and $\sqrt{\hat{s}} \gtrsim 3000$ [111]). This means that at low p_{T} and low $\sqrt{\hat{s}}$, combinig QED and non-photonic EW contributions results in a cancellation and their effect is negligible. At very high p_{T} and high $\sqrt{\hat{s}}$,

however, the QED and non-photonic EW effects add up and become significantly large and have to be taken into account.

In p_T and $\sqrt{\hat{s}}$ ranges accessible at the Tevatron, the non-photonic EW corrections are negative and about 4–5%. Unlike the LHC case where the QED corrections were much smaller than the non-photonic EW contributions except for very high p_T and high $\sqrt{\hat{s}}$, the QED corrections are comparable in size to the non-photonic EW contributions at the Tevatron. This means that although each set of corrections separately remains well below 10%, combining these two might easily lead up to the 10% level.

We can therefore conclude that the QED corrections, together with the rest of EW corrections, should be taken into account in the predictions for the precision measurements at the Tevatron since they can have significantly large impact on the distributions already for relatively low p_T and low $\sqrt{\hat{s}}$. The same applies to the the high p_T and high $\sqrt{\hat{s}}$ analysis at the LHC.

Chapter 7

SUSY-EW corrections to stop pair production

Within supersymmetric theories top-squarks are the supersymmetric partners of the top quarks. The two states $\tilde{t}_L$ and $\tilde{t}_R$, which appear in the chiral supermultiplets $\hat{Q}$ and $\hat{T}$, mix to produce the two mass eigenstates $\tilde{t}_1$ and $\tilde{t}_2$ (see section 3.4.2). In many supersymmetric models, the lighter top-squark $\tilde{t}_1$, is expected to become the lightest squark [133].

There are two effects which determine the values of the top-squark masses. Both are induced by the large top–stop Yukawa coupling. On one hand, the soft SUSY breaking parameters decrease the squark masses for the third generation while running from the GUT scale to a low-energy scale via the renormalization group equations (RGEs) much more than for the first and second generation. [31]. On the other hand, the large mixing in the stop and sbottom sector leads to substantial splitting between the two stop or sbottom mass eigenstates [134]. As a result, top and bottom squarks acquire potentially small masses. These effects can combine in such a way that the lighter top-squark becomes the lightest squark.

7.1 Top-squark pair production

At hadron colliders, top-squarks can be produced in pairs via strong interactions. As a consequence, the top-squark production cross section in case of relatively small top-squark mass $m_{\tilde{t}_1}$ could be significant. For this reason, the top-squarks $\tilde{t}_1$ are of particular interest for collider experiments.

Current experimental limits on top-squark pair production include searches performed at LEP [135] reviewed e.g in [136], and at the Tevatron, done by the CDF and DØ collaborations in approximately 90 pb^{-1} of Run I data [137].
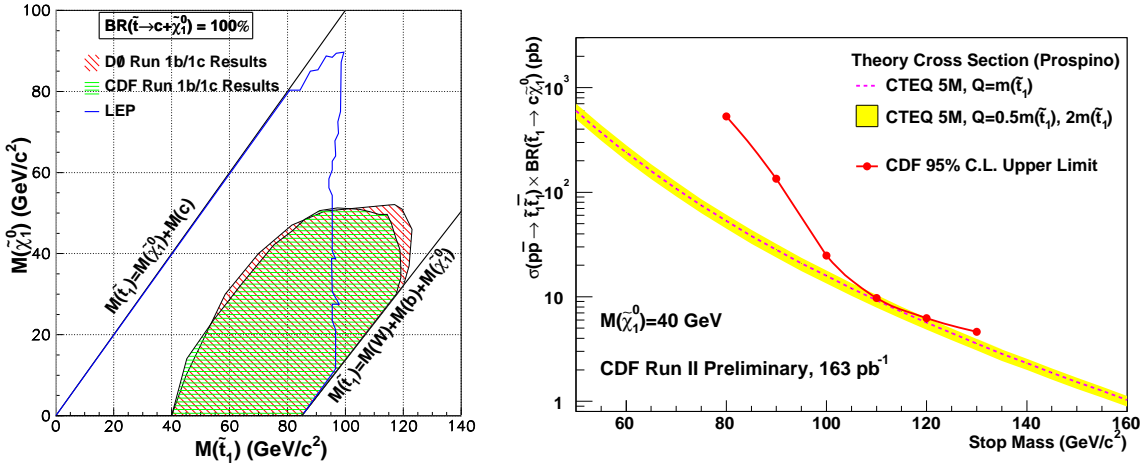
Figure 7.1: Exclusion limits from the searches for top-squarks in the decay $\tilde{t}_1 \rightarrow c\tilde{\chi}_1^0$ [138]. On the left: 95% C.L. exclusion region as function of the masses of the top-squark and of the lightest neutralino, $M_{\tilde{t}}$ and $M_{\tilde{\chi}_1^0}$. On the right: cross section limit for the $\tilde{t}\tilde{t}^+$ pair production for assumed $M_{\tilde{\chi}_1^0} = 40\,\text{GeV}$ compared to NLO prediction.

The CDF collaboration also performed a preliminary measurement based on 163 pb^{-1} of the Run II data [138]. The latest limits for the top-squark mass in relation with the mass of the lightest neutralino are shown in Fig. 7.1 (left). The CDF collaboration also provides a comparison of the upper limit for the pair production cross section with the theoretical prediction (Fig. 7.1 right).

Experimental searches for the top-squarks have also been done in ep collisions at HERA [139]. Here the top-squark could be kinematically accessible as a resonance only, and therefore constraints can be imposed on the *R-parity* violating class of supersymmetric models where a single top-squark can be produced.

Concerning the theoretical predictions, the cross sections for the production of squarks and gluinos in hadron collisions have been calculated at the Born-level in [140]. The currently used predictions have been improved by including NLO corrections in supersymmetric QCD (SUSY-QCD). These were worked out in [141] with the restriction of the final state squarks to the light quark sector. The analysis for the stop sector requires proper treatment of the large mixing effects and was supplemented in [142]. The production of top-squark pairs is diagonal at lowest order. Also, at $\mathcal{O}(\alpha_s^3)$ the cross sections are still diagonal in the stop sector. The non-diagonal production is suppressed as the cross section becomes non-zero only at $\mathcal{O}(\alpha_s^4)$. The production of non-diagonal top-squark pairs can also proceed at $\mathcal{O}(\alpha^2)$ via Z-exchange in e^+e^- annihilation [143], or $q\bar{q}$ annihilation [144], but is suppressed at hadron colliders.

The cross sections for the diagonal top-squark pair production depend essentially

only on the mass of the produced stop particles, $m_{\tilde{t}_1}$ or $m_{\tilde{t}_2}$. The dependence on other supersymmetric parameters, like the mixing angle, the gluino mass, the masses of other squarks, etc., is very weak, since these parameters affect only the higher order corrections and are not relevant at leading order. As a consequence, bounds on the $\tilde{t}_1 \tilde{t}_1^+$ production cross section can easily be translated into lower bounds on the lightest stop mass, without reference to other supersymmetric parameters. Furthermore, once the top-squarks are discovered, their masses can directly be determined from the cross section measurement.

In the following, we study the EW-like corrections to the top-squark pair production within the MSSM. We assume MSSM with real parameters and *R-parity* conservation.

7.1.1 Partonic cross sections at lowest order

At hadron colliders, diagonal pairs of top-squarks can be produced at lowest order QCD in gluon–gluon fusion and quark–antiquark annihilation:

$$gg \rightarrow \tilde{t}_1 \tilde{t}_1^+ \qquad \text{and} \qquad \tilde{t}_2 \tilde{t}_2^+$$
$$q\overline{q} \rightarrow \tilde{t}_1 \tilde{t}_1^+ \qquad \text{and} \qquad \tilde{t}_2 \tilde{t}_2^+$$

As already mentioned, mixed pairs cannot be produced in lowest order since the $g\tilde{t}\tilde{t}^+$ and $gg\tilde{t}\tilde{t}^+$ vertices are diagonal in the chiral as well as in the mass basis.

The top-squark pair production within the MSSM has many similar features to top quark pair production in the SM, which was studied in the previous chapter. Many procedures and partial results obtained for top quarks are therefore applicable to top-squarks. The differences originate from the fact that top-squark is a scalar, while the top quark is a fermion. As shown in Fig. 7.2, the same topologies of $\mathcal{O}(\alpha_{\mathrm{s}}^2)$ tree-level diagrams are present as for the top quark production (Fig 6.2), just with the fermions replaced by the scalars. However, there is an extra contribution from the $gg\tilde{t}\tilde{t}^+$ interaction vertex, which does not exist in the SM, but can be derived from the MSSM Lagrangian.

The corresponding cross sections for the partonic subprocesses can be expressed as given in [142],

$$\hat{\sigma}_{LO}[gg \rightarrow \tilde{t}_k \tilde{t}_k^+] = \frac{\alpha_s^2 \pi}{\hat{s}} \left\{ \beta_k \left(\frac{5}{48} + \frac{31 m_{\tilde{t}_k}^2}{24\hat{s}} \right) + \left(\frac{2 m_{\tilde{t}_k}^2}{3\hat{s}} + \frac{m_{\tilde{t}_k}^4}{6\hat{s}^2} \right) \ln \left(\frac{1-\beta_k}{1+\beta_k} \right) \right\},$$

$$\hat{\sigma}_{LO}[q\overline{q} \rightarrow \tilde{t}_k \tilde{t}_k^+] = \frac{\alpha_s^2 \pi}{\hat{s}} \frac{2}{27} \beta_k^3. \tag{7.1}$$

Here $\hat{s}$ is the partonic center-of-mass energy, and β_k is the relative velocity, given by $\beta_k = \sqrt{1 - 4m_{\tilde{t}_k}^2/\hat{s}}$, with $k = 1, 2$.
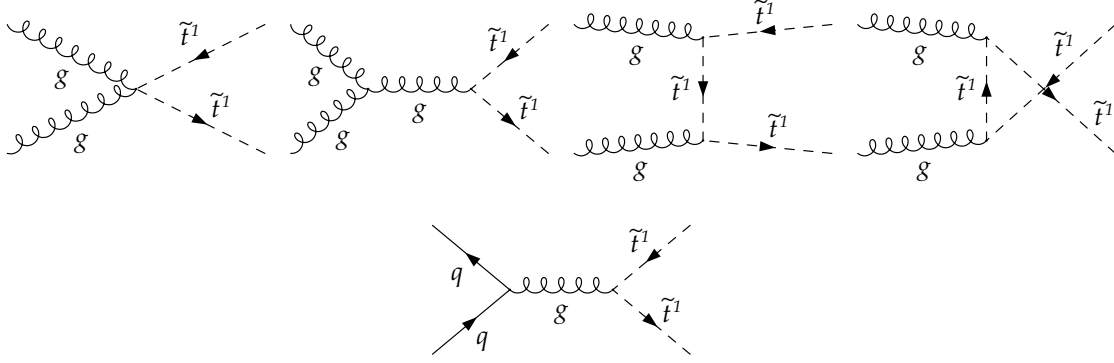
Figure 7.2: Feynman diagrams for the $\tilde{t}_1\tilde{t}_1^+$ production at lowest order in QCD, for the gluon–gluon fusion (up) and quark–antiquark annihilation (down) subprocesses.

7.2   General aspects of NLO SUSY-EW corrections

In the following we investigate the SUSY-EW corrections to top-squark pair production at one-loop level, including the IR divergent photonic contributions. While within the SM it was possible to separate the IR divergent QED corrections from the rest of EW corrections which were IR finite, this is no longer the case in the MSSM. Except for the gauge bosons of the SM sector, also their supersymmetric partners, gauginos, are necessary to obtain gauge-invariant and UV finite results.

Hypothetically, the treatment of IR singularities related to massless photons could be performed within a supersymmetric analogue of QED. To build such a theory, the photon and its superpartner, photino, are required. However, the photino itself is not a mass eigenstate of the theory, but it mixes with other neutral gauginos to form the neutralinos (see section 3.4.4). As a consequence, it is not possible to take the photino apart from the rest of gauginos. On the other hand, leaving out the photon spoils the balance of fermionic and bosonic degrees of freedom in supersymmetry, and thus leads to UV-divergent results. For these reasons the QED contributions and the rest of the SUSY-EW corrections do not form two independent subsets within the MSSM.

Concerning the renormalization procedure which is necessary to obtain UV finite production cross sections, only the top-squark mass and the wave functions of external quark and top-squark fields have to be renormalized. In analogy to our calculation of the NLO QED corrections to top pair production, neither the gluon fields nor the strong coupling need to be renormalized. Again, this originates from the non-existence of an $\mathcal{O}(\alpha)$ coupling of the gluon field.

In order to determine counter terms for the NLO SUSY-EW corrections, the bare parameters of the MSSM Lagrangian have to be replaced by the renormalized quantities. Subsequently, the renormalization constants are fixed within a renormalization
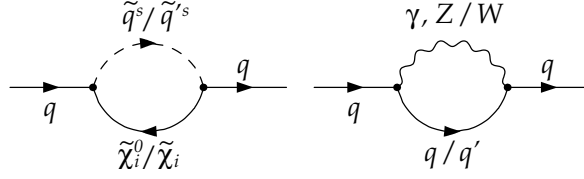
Figure 7.3: Feynman diagrams for the SUSY-EW contributions to the self-energy of incoming quarks. Only light quarks are considered. The Higgs boson contributions are neglected (the sfermion index is $s = 1, 2$, the neutralino and chargino indices are $i = 1, \ldots, 4$ and $i = 1, 2$, respectively).

scheme by imposing conditions on the renormalized self-energies of incoming and outgoing particles.

7.2.1   Quark and squark self-energies at one-loop level

In the case of incoming quarks, the renormalized self-energies of $\mathcal{O}(\alpha)$ have already been discussed in section 6.2.1, where expressions for the photonic contributions were explicitly given. Here we consider the full SUSY-EW corrections which include the gauge bosons γ, Z and W, as well as the neutralinos $\tilde{\chi}_i^0$ with $i = 1, \ldots, 4$, and the charginos $\tilde{\chi}_i^+$ with $i = 1, 2$ (Fig. 7.3). Masses of the initial light quarks are set to zero whenever possible, i.e. except for the mass singular photonic corrections. The contributions of the Higgs bosons h^0, H^0, A^0 and H, and of the Goldstone bosons G^0 and G vanish, since they are proportional to the quark masses. The IR singularities related to the photon are regularized by the mass parameter λ as in our previous computation.

To derive the renormalized quark self-energies, we replace the bare parameters in the Lagrangian by the renormalized quantities[1] (see section 4.2 and 6.2.1)

$$
\begin{aligned}
\Psi_{L,R} \quad &\to \quad \left(1 + \frac{1}{2}\delta Z_{L,R}^q\right)\Psi_{L,R} \, , \\
m_q \quad &\to \quad m_q - \delta m_q \, ,
\end{aligned}
\tag{7.2}
$$

where $\Psi_{L,R}$ are the left- and right-handed components of the quark fields. The renormalized self-energies $\hat{\Sigma}$ can be then expressed as the sum of the unrenormalized self-energies Σ and the correspoding counter terms as

$$
\begin{aligned}
\hat{\Sigma}_L^q(p^2) \quad &= \quad \Sigma_L^q(p^2) + \delta Z_L^q \, , \\
\hat{\Sigma}_R^q(p^2) \quad &= \quad \Sigma_R^q(p^2) + \delta Z_R^q \, , \\
\hat{\Sigma}_S^q(p^2) \quad &= \quad \Sigma_S^q(p^2) - \frac{1}{2}\left(\delta Z_L^q + \delta Z_R^q\right) + \frac{\delta m_q}{m_q} \, ,
\end{aligned}
\tag{7.3}
$$

---

[1]Here we keep the quark masses and the mass renormalization constants explicitly.

with the decomposition of the renormalized self-energy analogous to the unrenormalized self-energy

$$\Sigma^q(p) = \not{p}\,\omega_-\Sigma_L^q(p^2) + \not{p}\,\omega_+\Sigma_R^q(p^2) + m_q\Sigma_S^q(p^2) \ . \tag{7.4}$$

Here $\omega_\pm$ are the projection operators defined in appendix B.2.2.

Renormalization of the squark self-energy requires counter terms with the renormalization constants of the squark masses and external squark fields. The squark masses can be parametrized by the mass matrix $M_{\tilde{q}}$, which was defined in general in Eqs. (3.20–3.23). In the following, we focus on the top-squark sector. It is convenient to rewrite the top-squark mass matrix in terms of the mass eigenvalues $m_{\tilde{t}_1}$, $m_{\tilde{t}_2}$ and the mixing angle $\theta_{\tilde{t}}$ as

$$M_{\tilde{t}} = \begin{pmatrix} \cos^2\theta_{\tilde{t}}\,m_{\tilde{t}_1}^2 + \sin^2\theta_{\tilde{t}}\,m_{\tilde{t}_2}^2 & \sin\theta_{\tilde{t}}\cos\theta_{\tilde{t}}\left(m_{\tilde{t}_1}^2 - m_{\tilde{t}_2}^2\right) \\ \sin\theta_{\tilde{t}}\cos\theta_{\tilde{t}}\left(m_{\tilde{t}_1}^2 - m_{\tilde{t}_2}^2\right) & \sin^2\theta_{\tilde{t}}\,m_{\tilde{t}_1}^2 + \cos^2\theta_{\tilde{t}}\,m_{\tilde{t}_2}^2 \end{pmatrix} \ . \tag{7.5}$$

The counter term for the mass matrix can be introduced by

$$M_{\tilde{t}} \to M_{\tilde{t}} + \delta M_{\tilde{t}} \ , \tag{7.6}$$

and in general contains counter terms for all relevant parameters, $\delta m_{\tilde{t}_1}$, $\delta m_{\tilde{t}_2}$, $\delta\theta_{\tilde{t}}$.

In analogy with the renormalization of external quark fields, we can substitute the external squark fields by the renormalized squark fields and corresponding Z-factors:

$$\begin{pmatrix} \tilde{t}_L \\ \tilde{t}_R \end{pmatrix} \to (\mathbb{1} + \tfrac{1}{2}\delta\mathcal{Z}_{\tilde{t}})\begin{pmatrix} \tilde{t}_L \\ \tilde{t}_R \end{pmatrix} \quad \text{with} \quad \delta\mathcal{Z}_{\tilde{t}} = \begin{pmatrix} \delta Z_{\tilde{t}_L} & 0 \\ 0 & \delta Z_{\tilde{t}_R} \end{pmatrix} \ . \tag{7.7}$$

In order to obtain the counter terms for the squark fields in the basis of mass eigenstates $(\tilde{t}_1, \tilde{t}_2)$, we perform the following transformation

$$\begin{pmatrix} \tilde{t}_L \\ \tilde{t}_R \end{pmatrix} \to U_{\tilde{t}}^+(\mathbb{1} + \tfrac{1}{2}\delta\tilde{\mathcal{Z}}_{\tilde{t}})\begin{pmatrix} \tilde{t}_1 \\ \tilde{t}_2 \end{pmatrix} \ , \tag{7.8}$$

with

$$\delta\tilde{\mathcal{Z}}_{\tilde{t}} = U_{\tilde{t}}\delta\mathcal{Z}_{\tilde{t}}U_{\tilde{t}}^+ - \delta\mathcal{Z}_{U_{\tilde{t}}} = \begin{pmatrix} \delta Z_{\tilde{t}_{11}} & \delta Z_{\tilde{t}_{12}} \\ \delta Z_{\tilde{t}_{21}} & \delta Z_{\tilde{t}_{22}} \end{pmatrix} \ . \tag{7.9}$$

Using the previous relations we can express the renormalized top-squark self-energy as

$$\hat{\Sigma}_{\tilde{t}}(k^2) = \Sigma_{\tilde{t}}(k^2) + \frac{1}{2}k^2(\delta\tilde{\mathcal{Z}}_{\tilde{t}}^+ + \delta\tilde{\mathcal{Z}}_{\tilde{t}}) - \frac{1}{2}(\delta\tilde{\mathcal{Z}}_{\tilde{t}}^+\mathcal{D}_{\tilde{t}} + \mathcal{D}_{\tilde{t}}\delta\tilde{\mathcal{Z}}_{\tilde{t}}) - U_{\tilde{t}}\delta M_{\tilde{t}}U_{\tilde{t}}^+ \ , \tag{7.10}$$

where $\hat{\Sigma}_{\tilde{t}}$, $\Sigma_{\tilde{t}}$ denote the renormalized and unrenormalized self-energies, respectively, and $\mathcal{D}_{\tilde{t}}$ is the diagonalized mass matrix of Eq. (3.24) with $\tilde{f} = \tilde{t}$.
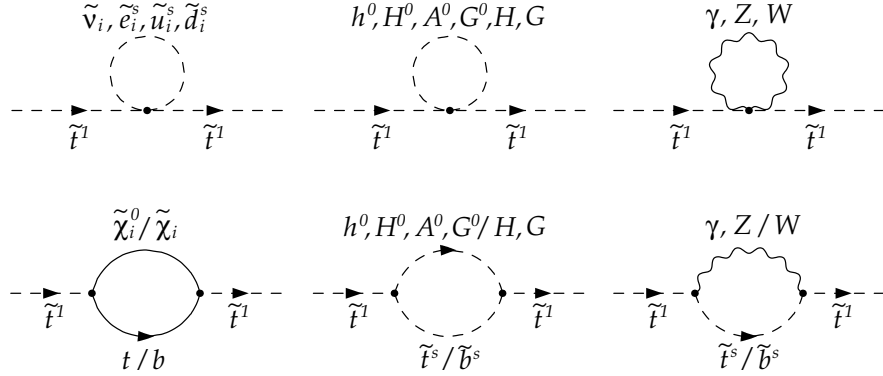
Figure 7.4: Feynman diagrams for the SUSY-EW contributions to the self-energy of the light top-squark (the sfermion index is $s = 1, 2$, the generation index is $i = 1, \ldots, 3$ and in case of the neutralinos and charginos the indices are $i = 1, \ldots, 4$ and $i = 1, 2$, respectively).

For convenience, we define

$$\delta m^2_{\tilde{t}_{ii}} = \left(U_{\tilde{t}} \, \delta M_{\tilde{t}} U_{\tilde{t}}^+ \right)_{ii} \, , \qquad \delta m^2_{\tilde{t}_{ij}} = \left(U_{\tilde{t}} \, \delta M_{\tilde{t}} U_{\tilde{t}}^+ \right)_{ij} \, . \tag{7.11}$$

In the case of diagonal top-squark pair production, only the diagonal terms $\hat{\Sigma}_{\tilde{t}_{ii}}$ (with $i = 1, 2$) of the self-energy matrix are relevant:

$$\hat{\Sigma}_{\tilde{t}_{ii}}(k^2) = \Sigma_{\tilde{t}_{ii}}(k^2) + k^2 \delta Z_{\tilde{t}_{ii}} - m^2_{\tilde{t}_{ii}} \delta Z_{\tilde{t}_{ii}} - \delta m^2_{\tilde{t}_{ii}} \, . \tag{7.12}$$

For the light top-squark pair production $i = 1$, and the contributing Feynman diagrams are shown in Fig. 7.4. They consist of tadpole insertions of the gauge and Higgs bosons, and of all sfermions. Only the $\mathcal{O}(\alpha)$ part of the squark quartic coupling is taken into account. The tadpole corrections yield contributions to the mass renormalization constant only, while the 2-point loop contributions that contain the Higgs, Goldstone and gauge bosons, as well as the neutralinos and charginos, contribute to the renomalization constants of the mass and of external squark fields.
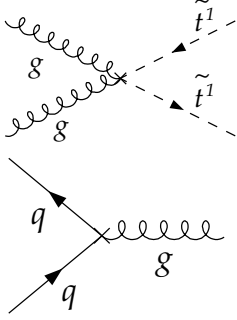
Counter terms for the self-energy, quark and squark vertex and squark quartic interaction at NLO are given by[2]

$$i\delta\Sigma_{\tilde{t}_{ii}} = i\left(k^2 \, \delta Z_{\tilde{t}_{ii}} - m^2_{\tilde{t}_{ii}} \, \delta Z_{\tilde{t}_{ii}} - \delta m^2_{\tilde{t}_{ii}} \right) \, , \tag{7.13}$$

$$i\delta\Lambda_{\mu_{ii}} = -ig_s T^c \left(k + k' \right)_\mu \delta Z_{\tilde{t}_{ii}} \, , \tag{7.14}$$
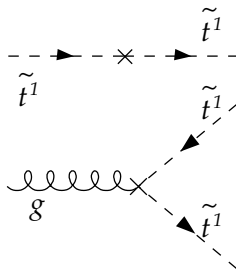
[2]Feynman diagrams are shown for $i = 1$, but the same applies to $i = 2$.

$$i\delta\Lambda^{SSVV}_{\mu_{ii}} = \frac{1}{2}ig_s^2\left(\frac{1}{3}\delta_{ab} + d_{abc}T^c\right)g_{\mu\nu}\,\delta Z_{\tilde{t}_{ii}}\,, \quad (7.15)$$

$$i\delta\Lambda^q_\mu = -ig_sT^c\gamma_\mu\left(\omega_-\delta Z^q_L + \omega_+\delta Z^q_R\right)\,, \quad (7.16)$$

where k, k' denote the momenta of top-squarks (in the direction of arrows), a, b and c are the gluonic color indices and T^c and d_{abc} are the color factors (we skip the fermionic and sfermionic color indices). In Fig. 7.5 we summarize all the counter terms that are needed for the NLO SUSY-EW corrections to both partonic subprocesses.

7.2.2 On-shell renormalization conditions

Imposing the on-shell renormalization conditions on the renormalized quark self-energies (see section 6.2.1) fixes the renormalization constants of initial quark fields $\delta Z^q_{L,R}$:

$$\delta Z^q_L = -\Sigma_L(p^2 = m_q^2) - m_q^2\frac{\partial}{\partial p^2}(\Sigma_L + \Sigma_R)\big|_{p^2=m_q^2} - 2m_q^2\frac{\partial}{\partial p^2}\Sigma_S\big|_{p^2=m_q^2}\,,$$

$$\delta Z^q_R = -\Sigma_R(p^2 = m_q^2) - m_q^2\frac{\partial}{\partial p^2}(\Sigma_L + \Sigma_R)\big|_{p^2=m_q^2} - 2m_q^2\frac{\partial}{\partial p^2}\Sigma_S\big|_{p^2=m_q^2}\,. \quad (7.17)$$

In the top-squark sector, we impose the following on-shell renormalization condition on the diagonal terms of the self-energy matrix $\hat{\Sigma}_{\tilde{t}_{ii}}$ (with $i = 1, 2$)

$$\mathrm{Re}\hat{\Sigma}_{\tilde{t}_{ii}}(m_{\tilde{t}_i}^2) = 0\,, \quad (7.18)$$

to fix the renormalization constants for the top-squark masses $\delta m^2_{\tilde{t}_{ii}}$ as

$$\delta m^2_{\tilde{t}_i} = \left(U_{\tilde{t}}\,\delta M_{\tilde{t}}\,U^+_{\tilde{t}}\right)_{ii} = \mathrm{Re}\Sigma_{\tilde{t}_{ii}}(m_{\tilde{t}_i}^2)\,. \quad (7.19)$$

As discussed in section 7.1, the lowest order production cross sections are diagonal in the stop sector. Mixing enters explicitly only through higher order diagrams. For this reason the mixing angle $\theta_{\tilde{t}}$ does not need to be renormalized [145] and thus no restrictions on the off-diagonal self-energy terms are needed.

The on-shell renormalization condition for the residue of the squark propagators

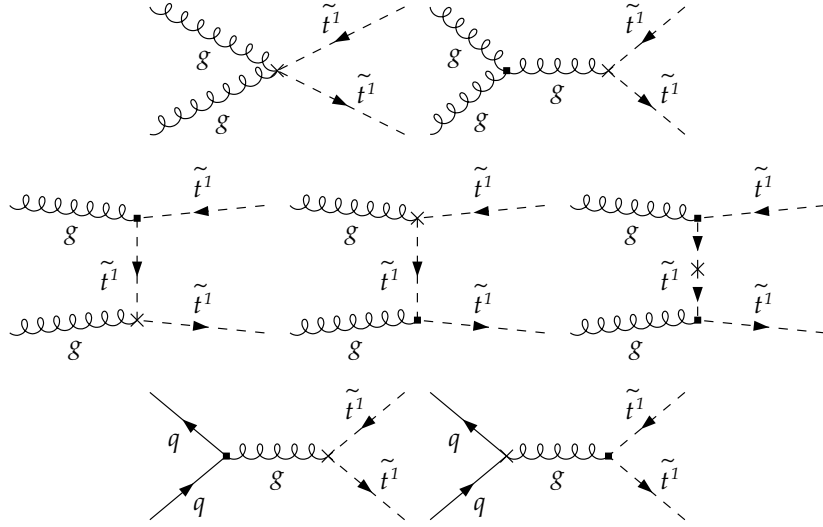$$\frac{d}{dk^2}\mathrm{Re}\,\hat{\Sigma}_{ii}(k^2)\bigg|_{k^2=k_i^2} = 0\,, \quad (7.20)$$

Figure 7.5: Feynman diagrams for the counter terms to the SUSY-EW contributions to both partonic subprocesses of the light top-squark pair prodution (*u*-channel diagrams in the *gg* fusion channel are not explicitly shown).

fixes the renormalization constants of the squark fields

$$\delta Z_{\tilde{t}_{ii}} = -\frac{d}{dk^2} \text{Re} \Sigma_{\tilde{t}_{ii}}(k^2) \bigg|_{k^2 = m_{\tilde{t}_i}^2} . \tag{7.21}$$

In analogy to the top pair production, it is not necessary to renormalize the gluon field as there is no gluon coupling of $\mathcal{O}(\alpha)$. Also, the strong coupling constant does not need to be renormalized, since the Ward Identity preserves the cancellation of UV singularities in the sum of three-point functions and corresponding counter terms with renormalization of external quark and squark fields.

7.3   Classification of NLO SUSY-EW corrections

7.3.1   Virtual corrections

Due to the extended SUSY-EW sector, the number of contributing diagrams grows very large in the MSSM in contrast to the SM. To give an idea, there are more than 450 diagrams for the gluon fusion subprocess, while in the $q\bar{q}$ annihilation, the number of diagrams is ~ 50 for each light flavor. These are already reduced numbers by the approximation that the CKM matrix is an identity matrix, i.e. we neglect the mixing between flavors of different generations. Under these circumstances, fully automated tools for handling the Feynman diagrams and the corresponding amplitudes become a necessity.
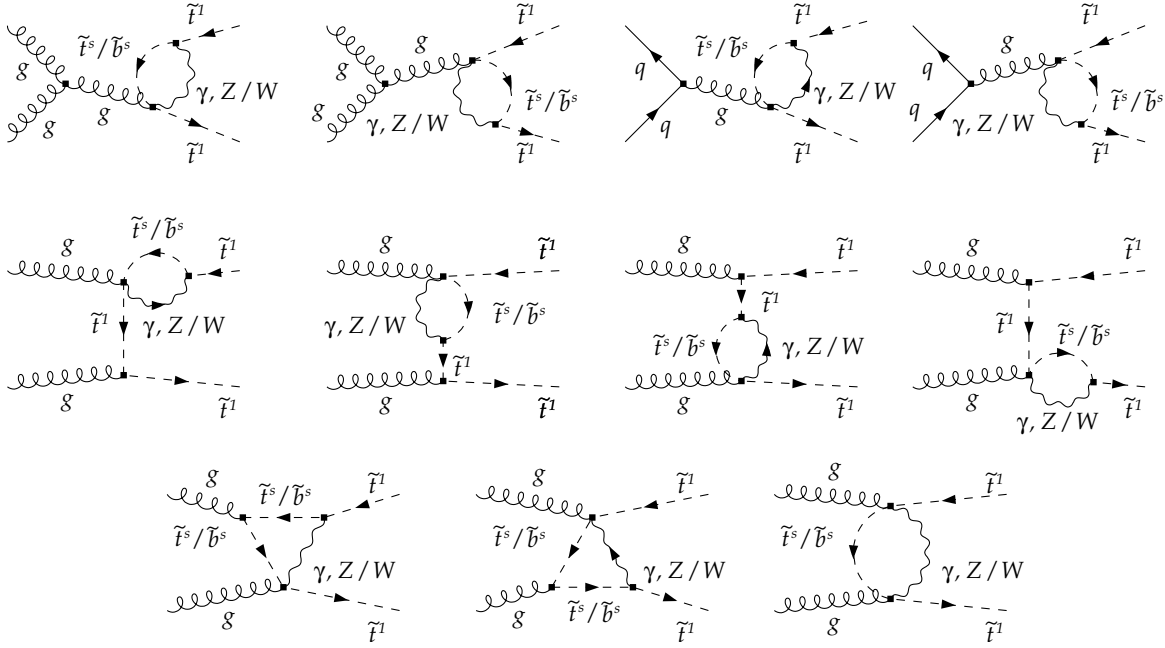
Figure 7.6: Feynman diagrams for the gluon–$\gamma/Z/W$–stop–stop contributions to both production subprocesses (the sfermion index is $s = 1, 2$ except for the case of photon where $s = 1$, the u-channel contributions are not explicitly shown).

We use the same techniques for the generation of Feynman diagrams and of the corresponding amplitudes as in the previous calculation (see section 6.2.1). The packages *FeynArts* and *FormCalc* have been extended for calculations within the MSSM. For basic notations about the treatment of loop integrals we again refer to appendix D. The partonic level cross sections with NLO SUSY-EW corrections can be obtained using the prescription of Eq. (6.8).

In analogy with the SM classification of Feynman diagrams, we divide the full set of virtual SUSY-EW corrections into several groups according to their topology. Except for the standard topologies, such as self-energy, vertex and box diagrams, new topologies emerge from the four-particle interaction terms present in the MSSM Lagrangian. The topologies which are analogous to the Standard Model can easily be derived from the NLO QED corrections to the top quark pair production by simply replacing the top quarks by the top-squarks and inserting all the Higgs, gauge and Goldstone bosons and their supersymmetric partners into the loops (Figs. 6.3, 6.4, for the gluon fusion and $q\bar{q}$ annihilation channel, respectively).

In the following we present new topologies which are not present in the Standard Model. Nevertheless, these do not form any finite subclass and cannot be treated separately from the SM-like part. We give a brief overview of different types of contributing topologies. Figure 7.6 illustrates diagrams which originate from the gluon–$\gamma/Z/W$–
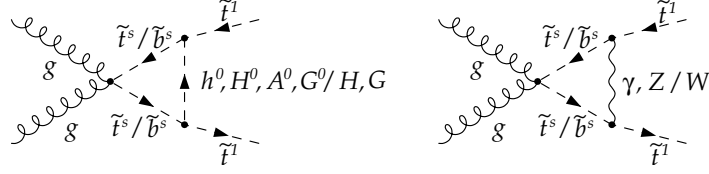
Figure 7.7: Feynman diagrams for the Higgs, gauge and Goldstone boson corrections to the gluon–gluon–squark–squark tree-level diagram (the sfermion index is $s = 1, 2$ except for the case of photon where $s = 1$).
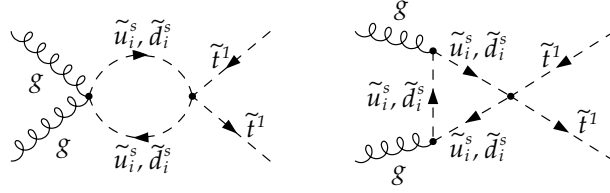

Figure 7.8: Feynman diagrams for the squark-loop contributions to the gluon–gluon–squark–squark tree-level diagram.

squark–squark interaction. These contribute to s-, t- and u-channnel gg fusion and to the $q\bar{q}$ annihilation. There is no such one-loop contribution to the four-particle $gg\tilde{t}\tilde{t}^+$ Born-level diagram. On the contrary, the gluon–$\gamma/Z/W$–squark–squark interaction itself represents a Born-level diagram which contributes to the photon-induced top-squark production (see section 7.4).

New two- and three-point topologies which correspond to the SUSY-EW corrections to the gluon–gluon–squark–squark tree-level diagram are shown in Figs. 7.7 and 7.8. The first set of diagrams consists of Higgs, gauge and Goldstone boson contributions and requires appropriate counter terms to obtain UV finite results. On the other hand, the second class of diagrams, composed of squark-loop corrections only, is UV finite even without renormalization.

Figure 7.9 shows the squark-loop contributions to the s-channel Higgs exchange. The sum of these contributions is UV finite and thus renormalization is not required. Concerning the quark loop contributions, the same triangle topology is only present
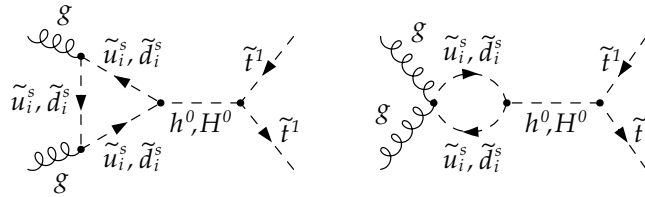

Figure 7.9: Feynman diagrams for the squark-loop contributions to the s-channel Higgs exchange.
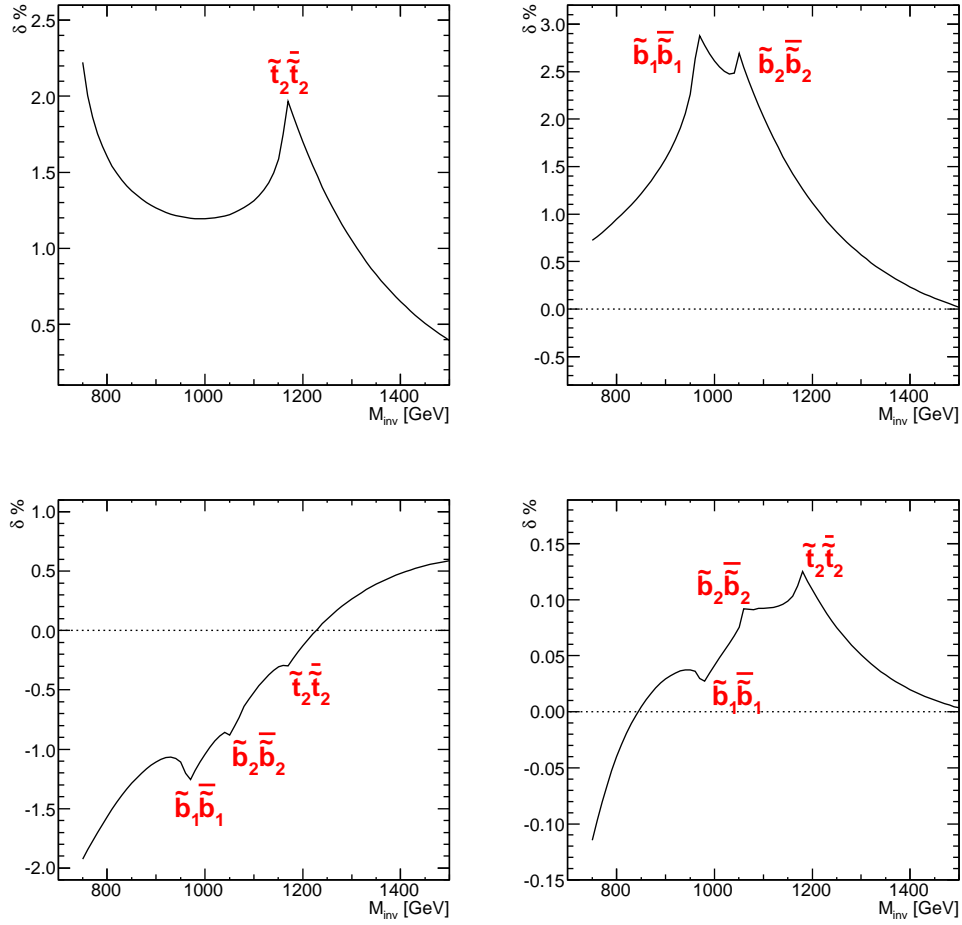
Figure 7.10: Threshold effects in the gg fusion channel manifested in the contributions of previously shown diagrams: up – Fig. 7.7 (neutral bosons – left, charged bosons – right), down left – Fig. 7.8, down right – Fig. 7.9. Main sources are the production thresholds of the heavy top-squark and the two bottom-squark pairs. We show the relative correction δ at the partonic level as function of the invariant mass of the top-squark pair.

for the top quark, since other quarks have negligible Yukawa couplings.

Figure 7.10 shows the threshold effects in the invariant mass distribution of the relative virtual correction δ, which is defined as a ratio of the NLO SUSY-EW corrections and the Born-level cross section. For simplicity, the results are given at the partonic level. Main sources of the threshold behavior can be deduced from the structure of loop insertions of Fig. 7.7. In the case of the neutral Higgs, gauge and Goldstone boson contributions, only one peak is visible (Fig. 7.10 up left), while for charged bosons two peaks are present (Fig. 7.10 up right). This is a direct consequence of the stop–stop coupling to neutral bosons and stop–sbottom coupling to charged bosons, respectively.
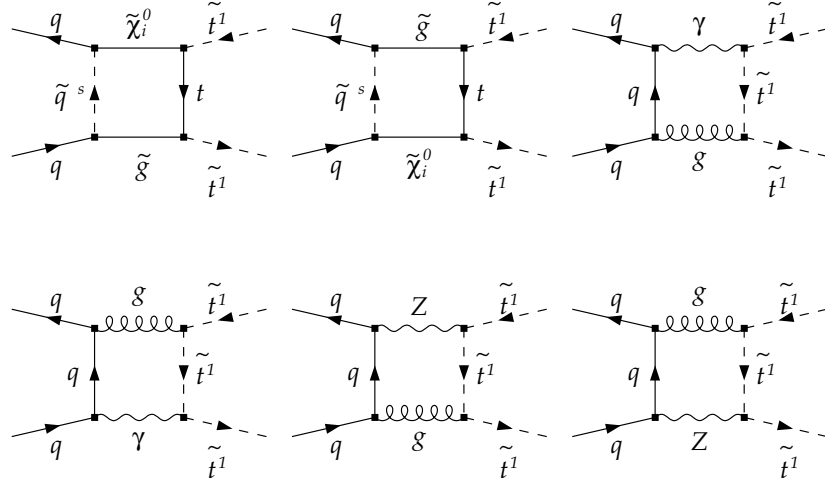
Figure 7.11: Feynman diagrams for the box contributions to $q\overline{q}$ annihilation, the crossed diagrams are not explicitly shown (the sfermion index is $s = 1, 2$, the neutralino index is $i = 1, \ldots, 4$).

The peaks correpond to the production thresholds of heavy stop pair and two sbottom pairs, respectively. No peak is present in the case of photonic correction, since photon couples to diagonal top-squark pairs only, i.e. to light stop pairs in our case. The two lower plots of Fig. 7.10 show that all three production thresholds are manifested if taking into account the squark-loop corrections of Figs. 7.8 and 7.9. A precise study indicates that there are threshold effects related to the squark pairs of the first two generations as well. However, due to several reasons, such as very large masses, degeneracy and small Yukawa couplings, these effects are suppressed by more than a factor of 100 and thus completely smeared out in the invariant mass spectrum.

Although we cannot separate the photonic corrections from the rest of SUSY-EW contributions, the treatment of IR and mass singularities is the same as in the top quark calculation, i.e. we introduce a fictitious photon mass λ to regularize the IR singularities and we keep the initial state quark masses when necessary.

In the gg fusion channel, the IR singularities originate from photon radiation exclusively, and mass singularities do not occur. In the $q\overline{q}$ annihilation subprocess, the IR singular structure is extended by the contributions related to the gluons which appear in the four-point UV finite loop integrals. There are two types of IR singular box contributions (Fig. 7.11). The first group is formed by the gluon–photon box diagrams with two sources of IR singularities, one related to the photons, the other to the gluons. The second group consists of the gluon–Z box diagrams with IR singularities originating from the gluons only. There is also an IR finite group of $\mathcal{O}(\alpha\alpha_{\mathrm{s}})$ box diagrams which consists of gluino–neutralino loops.
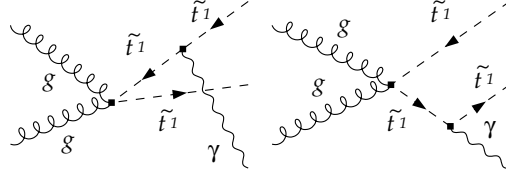
Figure 7.12: Feynman diagrams for real photon radiation off the quartic gluon–gluon–squark–squark contributions.
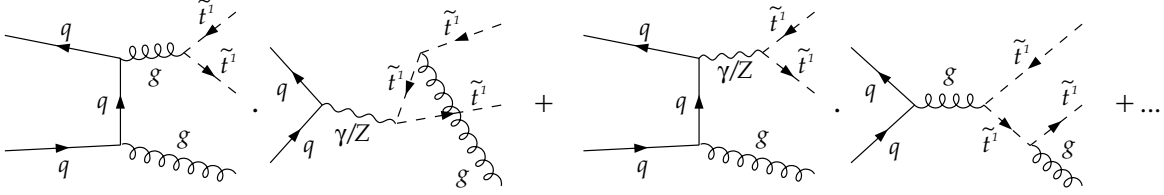

Figure 7.13: Non-zero contributions of $\mathcal{O}(\alpha\alpha_{\mathrm{s}}^2)$ corresponding to the interference of initial and final state gluon radiation off the $\mathcal{O}(\alpha)$ and $\mathcal{O}(\alpha_{\mathrm{s}})$ Born-level diagrams in the $q\bar{q}$ annihilation channel.

Due to collinear photon radiation off the light initial state quarks, mass singular logarithms $\ln m_q^2$ appear. The structure of mass singularities is related to the initial state only and thus it is identical to the top quark case.

7.3.2 Real corrections

To compensate IR singularities in the virtual SUSY-EW corrections, real photonic and gluonic contributions are required. In the case of gg fusion, only the photon bremsstrahlung is needed and the respective diagrams for the s-, t- and $u-$channel contributions can be deduced from Fig. 6.5 by inserting the top-squarks as final state particles. In addition, photon radiation off the gluon–gluon–squark–squark Born-level diagram is illustrated in Fig. 7.12.

In the $q\bar{q}$ annihilation channel, also the gluon bremsstrahlung contributions are necessary. In analogy to the top quark calculations, the interference of photon and gluon bremsstrahlung has to be taken into account in order to compensate the IR singularities in the gluon–photon box diagrams. These were discussed in detail in section 6.2.2. The corresponding Feynman diagrams can be deduced from Figs. 6.7 and 6.8 by the appropriate replacements. For the gluon–Z box contributions, only the gluon bremsstrahlung contributes since there are no IR singularities related to Z boson. Similarly as for the photon–gluon box corrections, the gluon bremsstrahlung of $\mathcal{O}(\alpha\alpha_{\mathrm{s}}^2)$ corresponds to the interference of the initial and final state gluon bremsstrahlung off the QCD-mediated and Z-mediated tree-level diagrams (Fig. 7.13).
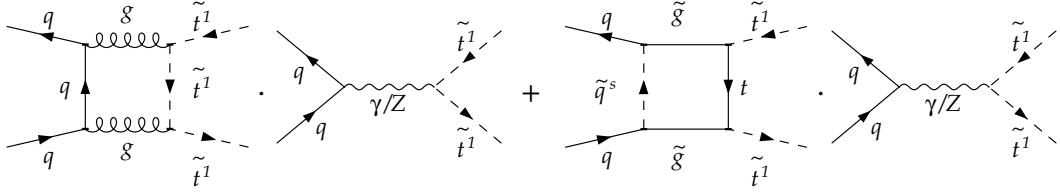
Figure 7.14: Feynman diagrams for the pure QCD box contributions, interfering with $\mathcal{O}(\alpha)$ photon and Z tree-level diagrams (crossed diagrams are not explicitly shown).
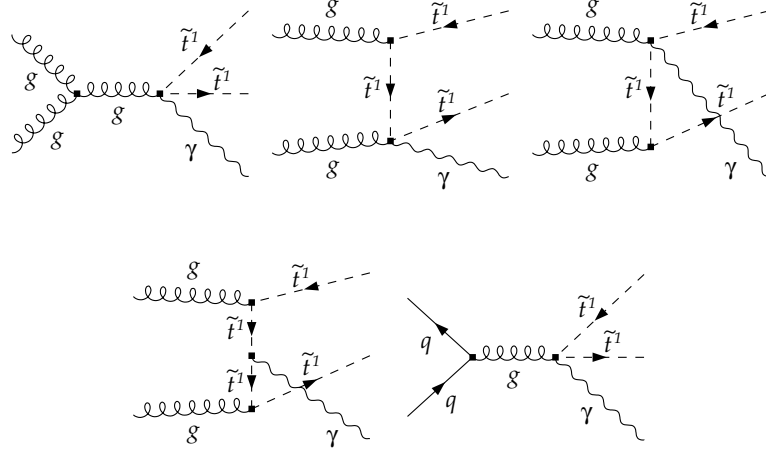

Figure 7.15: Feynman diagrams for the finite real photon corrections to both production subprocesses (u-channel contributions are not explictly shown).

Including the QED–QCD interference of real corrections does not yet lead to an IR finite result. Also the IR singular QCD-mediated box corrections interfering with the $\mathcal{O}(\alpha)$ photon and Z tree-level diagrams are needed. These are shown in Fig.7.14. Besides the gluonic corrections there are also the IR finite QCD-mediated box corrections, which contain gluinos in the loop. Interfered with the $\mathcal{O}(\alpha)$ tree-level diagrams, these also give contributions of the respective order of $\mathcal{O}(\alpha\alpha_{\mathrm{s}}^2)$.

So far we have mentioned only the IR singular bremsstrahlung contributions. However, there are also IR finite real corrections to both gluon fusion and $q\bar{q}$ annihilation processes. In addition to the photon radiation off the off-shell top-squark, which is analogous to the case of top quark, there are photon radiation contributions originating from the gluon–photon–squark–squark coupling. These contributions do not have to be regularized since they are not singular (Fig. 7.15).

The treatment of IR singular bremsstrahlung is the same as in chapter 6 and we refer to section 6.4 for more details. For simplicity, we again apply the phase space slicing method for the numerical analysis. Single virtual and real contributions, which are dependent on the cut-offs ΔE and $\Delta\theta$ (as introduced in section 6.4.1), have to
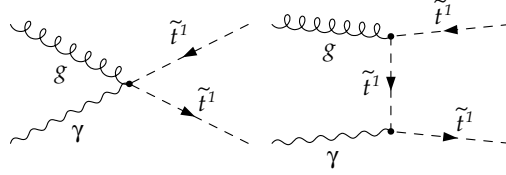
Figure 7.16: Feynman diagrams for the finite real photon corrections to both production subprocesses (the u-channel contributions are not explictly shown).

provide in total a fully independent result. We have performed analogous numerical checks as for the top quark case.

7.4   Photon-induced top-squark production

In analogy to the top pair production we also have to consider the photon-induced production mechanism in case of the top-squarks. At the hadronic level, these processes vanish at leading order owing to the non-existence of a photon distribution inside the proton and therefore represent contributions of higher order in QED. As already discussed in section 6.3, the photon–gluon partonic process is of NLO in QED, whereas the quark–photon process represents a contribution of even higher order. This is a direct consequence of collinear singularities present not only in the PDF but already in the partonic cross section. We therefore include only the photon–gluon process to the numerical analysis.

Feynman diagrams corresponding to the photon–gluon partonic process are illustrated in Fig. 7.16. Apart from the standard topology analogous to the top quark case, an additional four-particle topology contributes that arises from the gluon–photon–squark–squark interaction.

7.5   Numerical results

The hadronic cross section is obtained by convoluting the partonic cross sections with the parton distribution functions (PDFs), according to the prescription of Eq. (6.28). We use the NLO QED set of PDFs provided by the MRST group [92] with the factorization and renormalization scales chosen to be $\mu_f = \mu = 2\,m_{\tilde{t}_1}$. The factorization of mass singularities is done in the same way as in the $t\bar{t}$ calculation (see section 6.5.3). We also calculate the differential hadronic cross sections with respect to the invariant mass of the $\tilde{t}_1\tilde{t}_1^+$ pair and with respect to the transverse momentum of the top-squark. The respective formulae are given in Eq. (6.30) and Eq. (6.31).

The choice of supersymmetric parameters is done within the SPS 1a benchmark point, which is detailed in appendix A.2. In this scenario, relatively heavy top-squark mass eigenstates are obtained, with $m_{\tilde{t}_1} = 376.5$ GeV. Therefore we only present numerical analysis for the lighter top-squark pair which is of interest as the lightest squark pair within this scenario.

Concerning the treatment of IR singularities, we follow the phase space slicing method and split the real photonic and gluonic corrections into IR singular soft and IR finite hard bremsstrahlung part. The cancellation of IR singularities is then obtained by combining the soft bremsstrahlung with the virtual corrections. In the case of $q\bar{q}$ annihilation, the hard part of the photon phase space has to be split further into a collinear and a non-collinear part, in order to handle the mass singularities related to the initial state quarks. The values of cut-off parameters are chosen in the same way as for the top quark calculations, i.e. $\Delta E = 0.001\sqrt{\hat{s}}$ and $1 - \cos\Delta\theta = 0.01$ (see section 6.4.1).

In order to investigate the numerical impact of the NLO SUSY-EW corrections on the total hadronic stop pair production cross section we introduce a relative correction δ as the ratio of the NLO corrections $\delta\sigma$ and the Born-level cross section σ_B:

$$\delta = \frac{\sigma_{\text{1-loop}}(S) - \sigma_B(S)}{\sigma_B(S)} = \frac{\delta\sigma(S)}{\sigma_B(S)}\,, \tag{7.22}$$

where S is the total energy of the hadronic system, which is 14 TeV at the LHC. Due to the relatively large top-squark mass within the SPS1a scenario, the stop pair production cross section is very small at the Tevatron. Therefore, we only present a full numerical analysis for the case of LHC and postpone the discussion about the Tevatron to the next section.

We also use the relative correction δ to define the ratio of the differential hadronic cross sections in the same way as for the total cross sections, by substituting σ with the differential cross section $d\sigma$. In this way we obtain variations of δ as a function of the total partonic energy, equivalent to the invariant mass of the $\tilde{t}_1\tilde{t}_1^+$ pair, and of the transverse momentum of the top-squark.

In order to avoid numerical instabilities related to the $\tilde{t}_1\tilde{t}_1^+$ threshold and to match the experimental conditions we introduce, as in the top quark calculation, constraints on the transverse momentum, p_{T}, and on the pseudorapidity, η, of the top-squarks. At large scattering angles, the decay products of the top-squarks are better distinguishable from the background and the kinematical cuts thus serve to improve the signal over background ratio. We apply the following kinematical cuts:

$$p_{\text{T}} > 200\,\text{GeV} \quad \text{and} \quad |\eta| < 2.5\,. \tag{7.23}$$

Table 7.1: Total hadronic cross section for $\tilde{t}_1 \tilde{t}_1^+$ production at NLO SUSY-EW at the LHC in different production subprocesses without and with the cuts. The relative precision of the corrections achieved in the numerical integration is 10^{-3}.

Process	σ_{tot} without cuts [pb]		σ_{tot} with cuts [pb]	
	Born	correction	Born	correction
$u\bar{u}$	0.1319	-5.12×10^{-3}	0.1146	-4.88×10^{-3}
$d\bar{d}$	0.07572	-3.82×10^{-3}	0.06546	-3.48×10^{-3}
$s\bar{s}$	8.778×10^{-3}	-4.05×10^{-4}	7.260×10^{-3}	-3.56×10^{-4}
$c\bar{c}$	3.135×10^{-3}	-9.66×10^{-5}	2.549×10^{-3}	-9.15×10^{-5}
gg	1.437	-0.0147	0.6076	9.57×10^{-3}
$g\gamma$		0.0289		0.0132
pp	1.657	4.77×10^{-3}	0.7974	-5.18×10^{-3}

Table 7.1 shows numerical results for the total hadronic cross sections. The LO results and the SUSY-EW corrections are shown separately. The values of σ_{tot} are given for each production subprocess, and also combined to a complete result for $pp \to \tilde{t}_1 \tilde{t}_1^+ X$ at the LHC. Besides the gg fusion and $q\bar{q}$ annihilation production channels, we also investigate the gluon–photon channel which contributes at NLO. We can see that the gluon–photon contribution is of about the same size as the correction to the gg channel, but the opposite sign leads to a decrease in the overall correction. Applying the cuts reduces the Born-level cross sections more than the corrections and increases therefore the relative corrections. However, the numerical values still remain below 1% and the NLO SUSY-EW effects have thus negligible impact on the total hadronic cross section.

The same is not true for the differential hadronic cross sections. We investigate the distributions of the total center-of-mass energy of the partonic system, which is equivalent to the invariant mass of the top-squark system, and of the transverse momentum of the top-squark. Figure 7.17 shows the differential hadronic cross sections for the gg fusion and $q\bar{q}$ annihilation channels, without applying the cuts. It can be seen that the $q\bar{q}$ annihilation subprocess is suppressed at the hadronic level in low p_{T} and low $\sqrt{\hat{s}}$ regions, owing to dominant gluon densities at low x. However, for very high p_{T} and $\sqrt{\hat{s}}$, the $q\bar{q}$ channel takes over, since the valence quark densities dominate at high x. When looking at the relative size of SUSY-EW corrections (right), we can see that these are much larger in the $q\bar{q}$ channel owing to the subtleties of QED–QCD interference, which is not present at the Born-level.
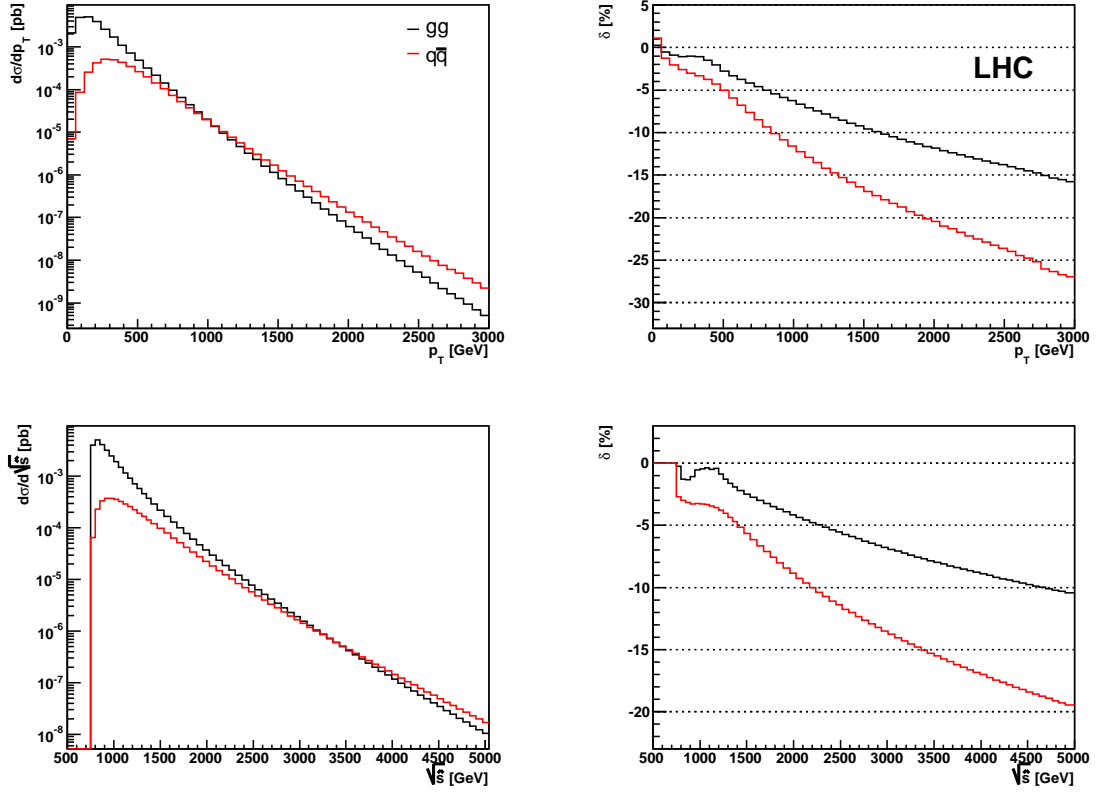
Figure 7.17: Differential hadronic cross sections (left), and variation of the relative correction δ (right), as functions of the transverse momentum of the top-squark (up) and of the total energy of the partonic system (down), at the LHC ($S = 14$ TeV), with no cuts applied, for both $\mathcal{O}(\alpha_s^2)$ production channels.

In the small region close to the production threshold the $\mathcal{O}(\alpha)$ corrections are positive and can become very large, as visible in the p_T distribution for the $q\overline{q}$ channel. Apart from this region, the SUSY-EW corrections are negative and reduce the LO cross sections the more the larger p_T and $\sqrt{\hat{s}}$. We can also observe the effects originating from the production thresholds of the third generation squark pairs, which were already discussed at the partonic level (Fig. 7.10). These are visible mainly in the invariant mass distribution of the relative correction in the gg channel. In this channel, the relative correction reaches more than 5% in size only for very large p_T and $\sqrt{\hat{s}}$, whereas in the $q\overline{q}$ channel, the relative corrections grow rapidly and reach more than 5% in size for $p_T \gtrsim 500$ GeV and $\sqrt{\hat{s}} \gtrsim 1300$ GeV.

The impact of applying the cuts is shown in Fig. 7.18. The results are presented separately for the gg and $q\overline{q}$ channels. In the gg case, the cuts have stronger impact on the differential cross sections (left) than in the $q\overline{q}$ channel. Concerning the relative
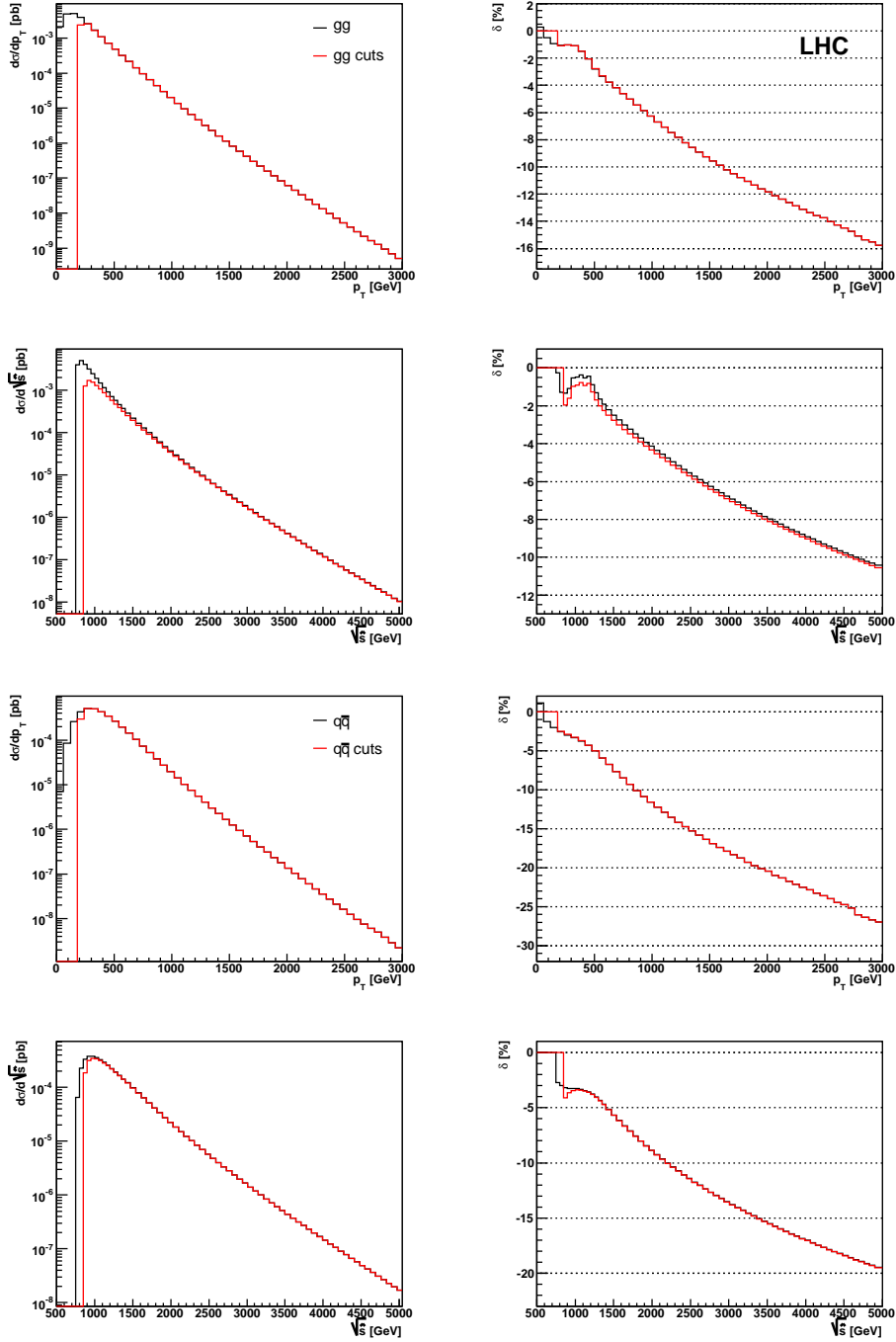
Figure 7.18: Differential hadronic cross sections (left) and relative correction δ (right), as functions of the transverse momentum of the top-squark (1st and 3rd row) and of the total partonic energy (2nd and 4th row), at the LHC ($S = 14$ TeV). The gg fusion and $q\bar{q}$ annihilation channels are investigated separately. The impact of cuts on the transverse momentum and on the pseudorapidity of the top-squarks, $p_T > 200$ GeV and $|\eta| < 2.5$, is also shown.
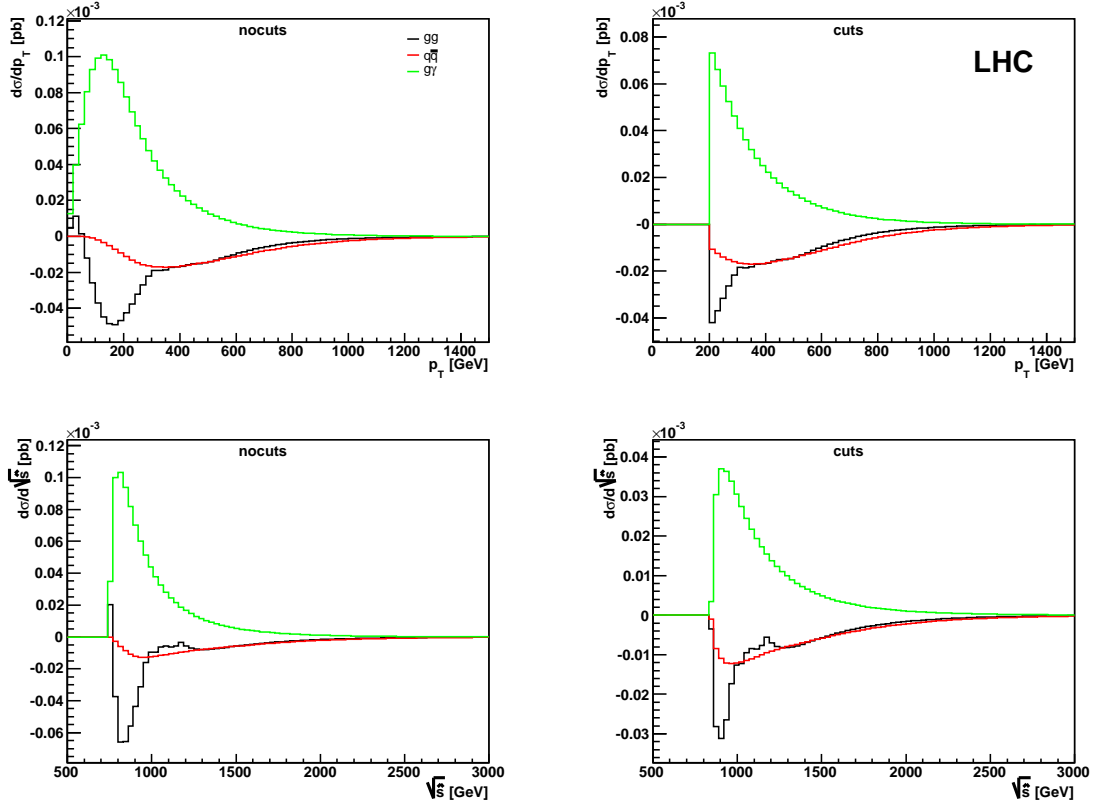
Figure 7.19: NLO SUSY-EW effects in the gg fusion, $q\bar{q}$ annihilation and $g\gamma$ production channels at the LHC ($S = 14$ TeV). Differential hadronic cross sections with respect to the the transverse momentum of the top-squark (up) and of the total energy of the partonic system (down) are shown without (left) and with (right) applying the cuts, $p_T > 200$ GeV and $|\eta| < 2.5$.

corrections (right) we can observe that although the large positive contributions at the threshold have been cut out, the cuts increase the size of the relative corrections, since they mainly reduce the Born-level contributions.

In Fig. 7.19 we investigate the impact of the photon-induced hadronic contribution to the $\tilde{t}_1\tilde{t}_1^+$ production. The $g\gamma$ contribution is shown in comparison with NLO SUSY-EW corrections in the gg fusion and $q\bar{q}$ annihilation channels. We can see that the photon-induced corrections are largest in size. This is due to the fact that the size of the $\mathcal{O}(\alpha\alpha_s^2)$ corrections is reduced by a factor of $\mathcal{O}(\alpha_s)$ with respect to the $\mathcal{O}(\alpha\alpha_s)$ tree-level process and the convolution with the gluon and photon parton densities can become quite large. As the sign of $g\gamma$ contribution is positive, whereas the other corrections are negative, this tends to reduce the size of the overall SUSY-EW contributions. Applying the cuts slightly reduces the photon–gluon hadronic cross section, as well as the gg fusion contribution, but the correction to the $q\bar{q}$ channel does not change much.
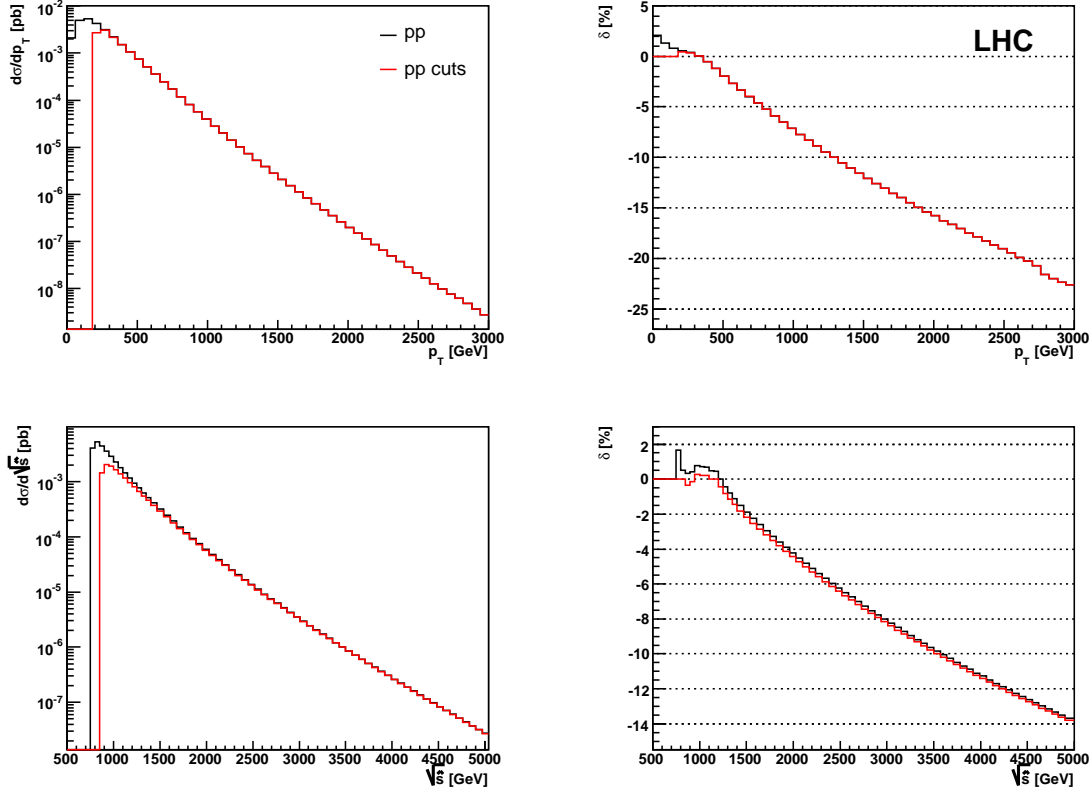
Figure 7.20: NLO SUSY-EW effects in pp collisions at the LHC ($S = 14$ TeV). Differential hadronic cross sections (left), and variation of the relative correction δ (right), as functions of the transverse momentum of the top-squark (up) and of the total energy of the partonic system (down), at the LHC ($S = 14$ TeV), with and without the cuts, $p_{\mathrm{T}} > 200$ GeV and $|\eta| < 2.5$. Also the contributions of the $g\gamma$ production channel are included.

In Fig. 7.20 we show the complete result for the top-squark production at NLO SUSY-EW in pp collisions at the LHC. All production subprocesses are combined including the photon-induced channel. The interplay between the negative corrections to the gg and $q\bar{q}$ channels and the positive and significantly large contribution of the $g\gamma$ production channel, which is visible in Fig. 7.19, leads to a reduction of the overall NLO SUSY-EW corrections, mostly in the low p_{T} and low $\sqrt{\hat{s}}$ regions.

Applying the cuts removes the positive corrections near the threshold, and a slight enhancement in size in the invariant mass spectrum of the relative correction is visible. In the low p_{T} and low $\sqrt{\hat{s}}$ regions, the overall relative NLO SUSY-EW corrections are negative and they further grow in size with increasing p_{T} and $\sqrt{\hat{s}}$ owing to the $q\bar{q}$ channel, which becomes important at high x. The relative corrections reach more than 5% in size for $p_{\mathrm{T}} \gtrsim 700$ GeV and $\sqrt{\hat{s}} \gtrsim 1800$ GeV. For $p_{\mathrm{T}} \gtrsim 1200$ GeV they become
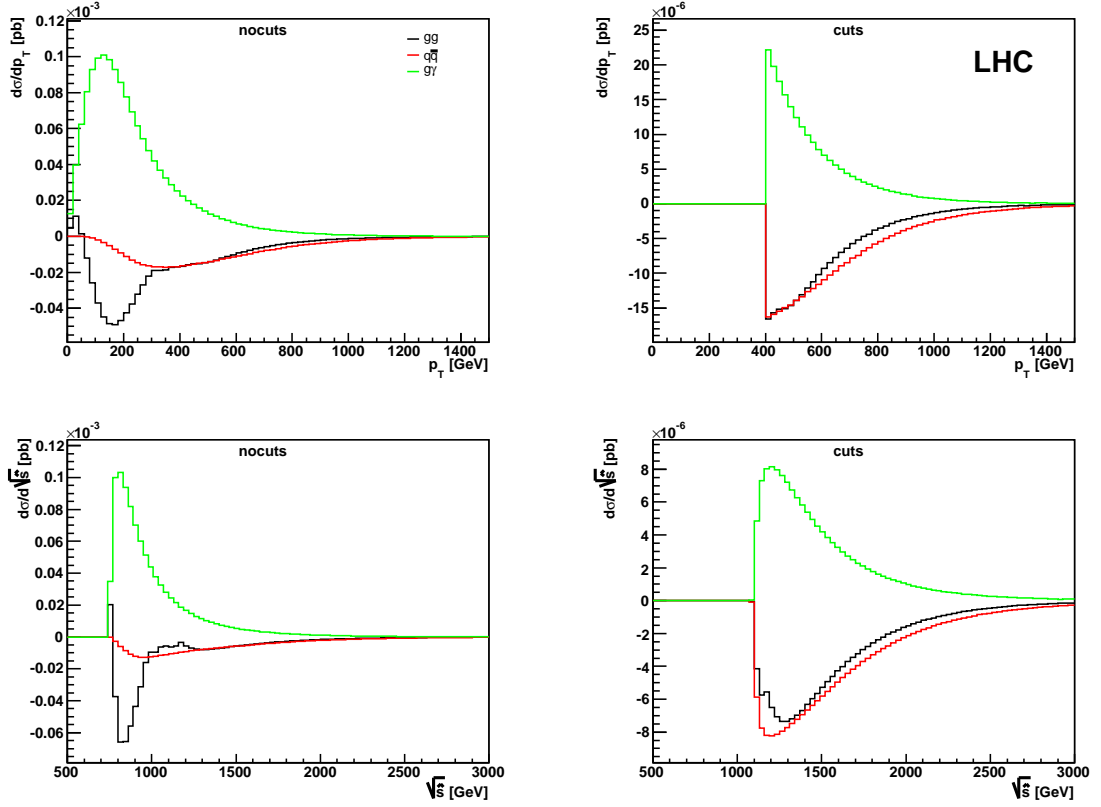
Figure 7.21: NLO SUSY-EW effects in the gg fusion, $q\bar{q}$ annihilation and $g\gamma$ production channels at the LHC ($S = 14$ TeV). Differential hadronic cross sections with respect to the the transverse momentum of the top-squark (up) and of the total energy of the partonic system (down) are shown without (left) and with (right) applying the cuts, $p_{\mathrm{T}} > 400$ GeV and $|\eta| < 2.5$.

larger than 10% in size and reach the current precision limits of the parton densities. If such a high p_{T} region will be considered in the LHC top-squark analysis, the NLO SUSY-EW contributions cannot be ignored.

We have observed that the SUSY-EW corrections become significantly large for high p_{T} and high $\sqrt{\hat{s}}$. In the following we therefore provide a deeper insight into this region by applying a much higher cut on the transverse momentum of the top-squark. In Fig. 7.21 we show the differential hadronic cross sections for the NLO SUSY-EW corrections in all production channels. The results (right) are obtained with the kinematical cuts:

$$p_{\mathrm{T}} > 400 \, \mathrm{GeV} \quad \text{and} \quad |\eta| < 2.5 \,, \tag{7.24}$$

and for comparison, also the results with no cuts applied are shown (left). As we have seen in Fig. 7.19, applying cuts reduces the contributions in the gg and $g\gamma$ channels
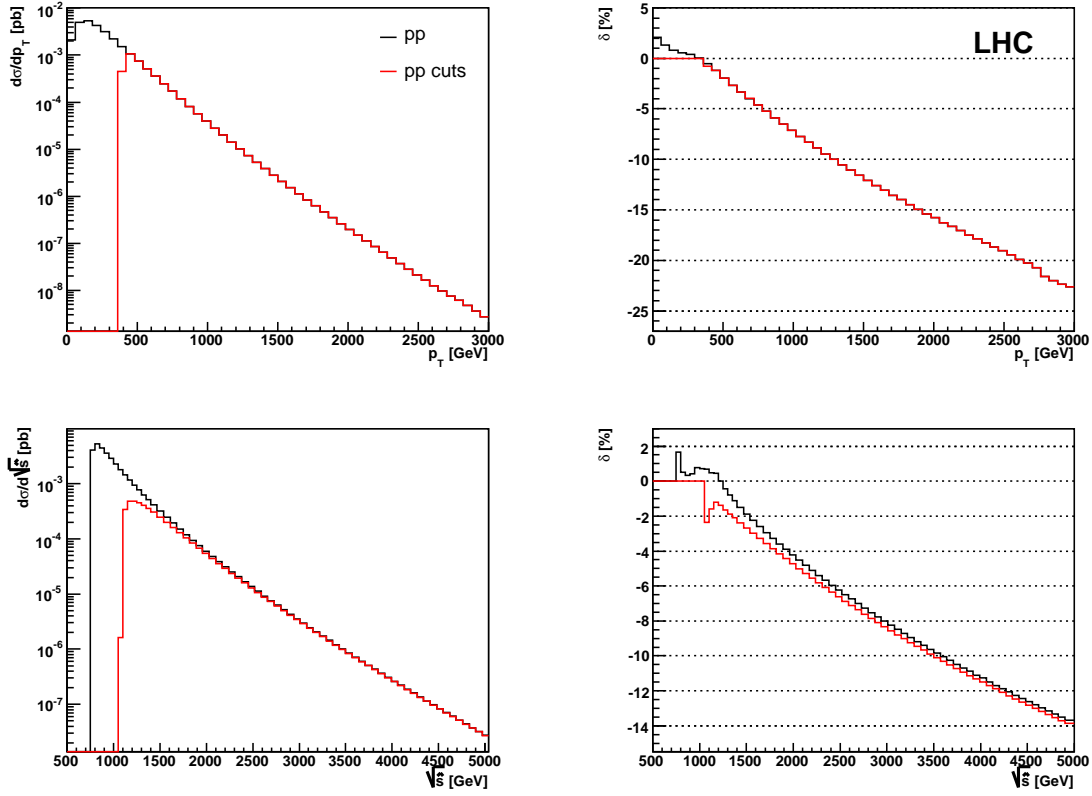
Figure 7.22: NLO SUSY-EW effects in the *pp* collisions at the LHC ($S = 14$ TeV). Differential hadronic cross sections (left), and variation of the relative correction δ (right), as functions of the transverse momentum of the top-squark (up) and of the total energy of the partonic system (down), at the LHC ($S = 14$ TeV), with and without the cuts, ($p_\mathrm{T} > 400$ GeV and $|\eta| < 2.5$). Also the photon–gluon hadronic corrections are included.

more than the $q\bar{q}$ contribution. This effect becomes stronger if a higher cut on p_T is applied (Fig. 7.21). Due to opposite signs, the *gg* and *gγ* contributions practically compensate each other.

The impact of higher cuts on the overall SUSY-EW corrections to the top-squark pair production in *pp* collisions at the LHC is shown in Fig. 7.22. Applying the cuts reduces the Born-level contributions more than the SUSY-EW corrections. As a result, an enhancement in the size of the overall relative corrections can be observed. We can see that as the SUSY-EW corrections become larger in size for high p_T and high $\sqrt{\hat{s}}$, they are further enhanced by imposing high p_T cuts.

We can conclude that although the SUSY-EW corrections have small impact on the total hadronic cross sections, they can become sizeable for the distributions. Within the high p_T and high $\sqrt{\hat{s}}$ regions that are going to be explored at the LHC, the NLO
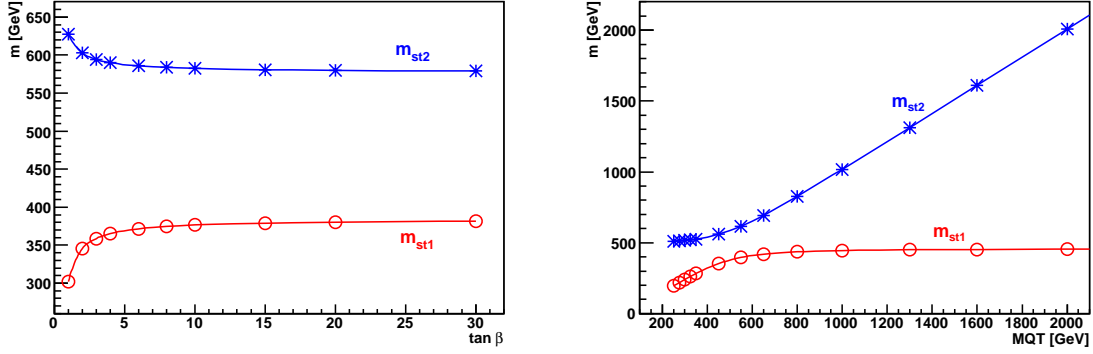
Figure 7.23: Dependence of the physical top-squark masses $m_{\tilde{t}_1}$ and $m_{\tilde{t}_2}$ on the variation of $\tan\beta$ (left) and $M_{\tilde{q}_T}$ (right).

SUSY-EW corrections are significant in size and thus essential for the studies.

7.6   Analysis of parameter dependence

In this section we analyse the dependence of the NLO SUSY-EW corrections on the various supersymmetric parameters. By varying the parameters typical for different sectors of the MSSM we can estimate the impact of these corrections on the top-squark production cross section. For simplicity, we do not vary more than one parameters at a time and the rest is fixed within the SPS 1a parameter set.

In the case of the gaugino mass parameters M_1, M_2 and M_3 their impact on the SUSY-EW corrections is straightforward, since these parameters only influence the higher order contributions.

The situation is more complicated in the sfermion sector. Here the soft-breaking parameters as well as $\tan\beta$ and μ directly determine the top-squark masses and thus enter already at Born-level. It is therefore not possible to clearly distinguish between the impact on the NLO corrections and on the kinematics of the Born-level cross section. Still we can get an idea about the dependence of the size of the corrections on these parameters.

To clarify the corelations between parameters in the sfermion sector, in Fig. 7.23 we show the dependence of the physical top-squark masses on the variation of $\tan\beta$ as well as on the variation of one of the soft-breaking parameters for the third generation of squarks, $M_{\tilde{q}_T}$. We can see that $m_{\tilde{t}_1}$ has similar behavior in both cases. For small values of the parameters, $m_{\tilde{t}_1}$ increases, then remains practically unchanged. The heavy top-squark mass $m_{\tilde{t}_2}$ also increases with $M_{\tilde{q}_T}$, although mainly for large values of the parameter. However, it decreases with $\tan\beta$. This is a consquence of the fact
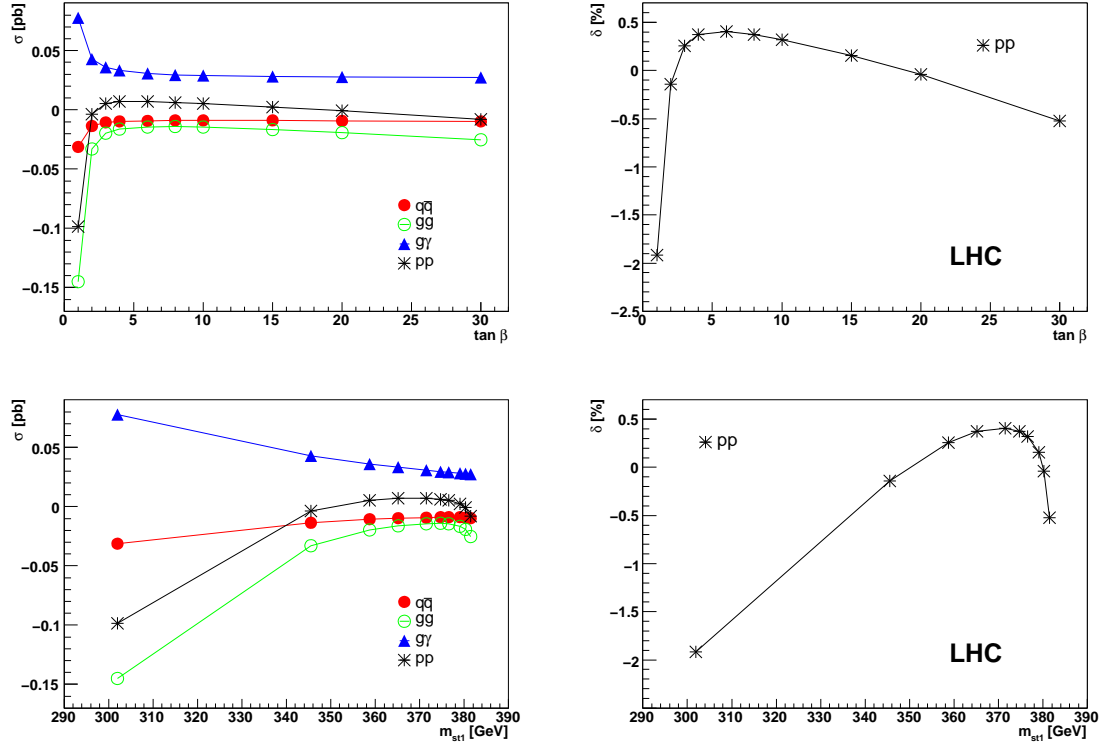
Figure 7.24: Dependence of the NLO SUSY-EW contributions on the variation of $\tan\beta$ (up) and the respective $m_{\tilde{t}_1}$ distribution (down). Integrated hadronic cross sections are shown for the corrections in all production channels separately and also combined (left). The overall relative correction for pp collisions at the LHC is also given (right).

that $\tan\beta$ contributes to the off-diagonal entries of the squark mass matrix and thus determines the splitting between the two physical masses, whereas $M_{\tilde{q}_T}$ appears as a diagonal entry.

We start our investigation of the parameter dependence in the sfermion sector since it is clear that here the effects will be largest. Figure 7.24 (up) shows the impact of the variation of $\tan\beta$. As mentioned above, the rest of the MSSM parameters is fixed at the SPS 1a point. We also study the variation of the SUSY-EW corrections as a function of the physical top-squark mass $m_{\tilde{t}_1}$ (Fig. 7.24 down). Plots on the left show the SUSY-EW corrections for all contributing channels as well as in total for pp collisions at the LHC. We also show the variation of the overall correction δ relative with respect to the Born-level cross section (Fig. 7.24 right).

As we can see, the corrections become largest in size for very small $\tan\beta$, (about 2%). As a consequence of the opposite signs, certain cancellation between the contributions in gg, $q\bar{q}$ and $g\gamma$ channels occurs. The strong increase in size of the relative correction at small $\tan\beta$ is mainly related to the kinematics of the process, since the
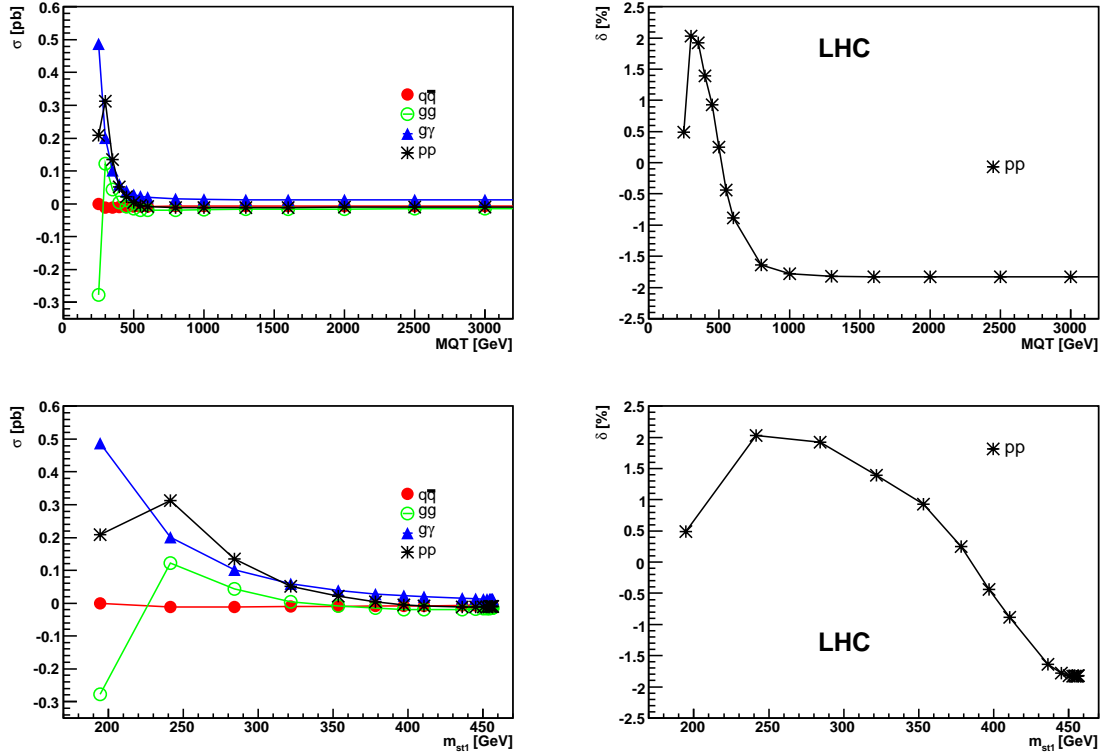
Figure 7.25: Dependence of the NLO SUSY-EW contributions on the variation of the diagonal soft-breaking parameter of the third squark generation $M_{\tilde{q}_T}$ (up) and the respective $m_{\tilde{t}_1}$ distribution (down). Integrated hadronic cross sections are shown for the corrections in all production channels separately and also combined (left). The overall relative correction for pp collisions at the LHC is also given (right).

cross section increases for small masses of the produced particles. At large $\tan\beta$, the distributions of corrections are flat except for the gg channel where an increase towards largest $\tan\beta$ is visible. This is also present in the variation of the relative correction with $\tan\beta$, as well as in the distribution of $m_{\tilde{t}_1}$.

Figure 7.25 shows the impact of the soft-breaking mass parameter of the third squark generation $M_{\tilde{q}_T}$ on the SUSY-EW corrections. Similar to $\tan\beta$, this parameter also influences the kinematics of the process as well as the corrections.

The gg channel contribution shows a similar behavior as previously. A sharp increase in size is visible for very low mass range. The same can be observed in the $g\gamma$ channel. Due to opposite signs the overall correction is reduced (Fig. 7.25 right). The relative correction is positive for small mass ranges and reaches a maximum of 2% for $m_{\tilde{t}_1}$ of 250–300 GeV. Varying $M_{\tilde{q}_T}$ towards very large values yields a negative overall correction which reduces the Born-level cross section. For very large $M_{\tilde{q}_T}$ δ saturates at 2% level. This corresponds to a maximum of $m_{\tilde{t}_1}$ of about 450 GeV that can be reached
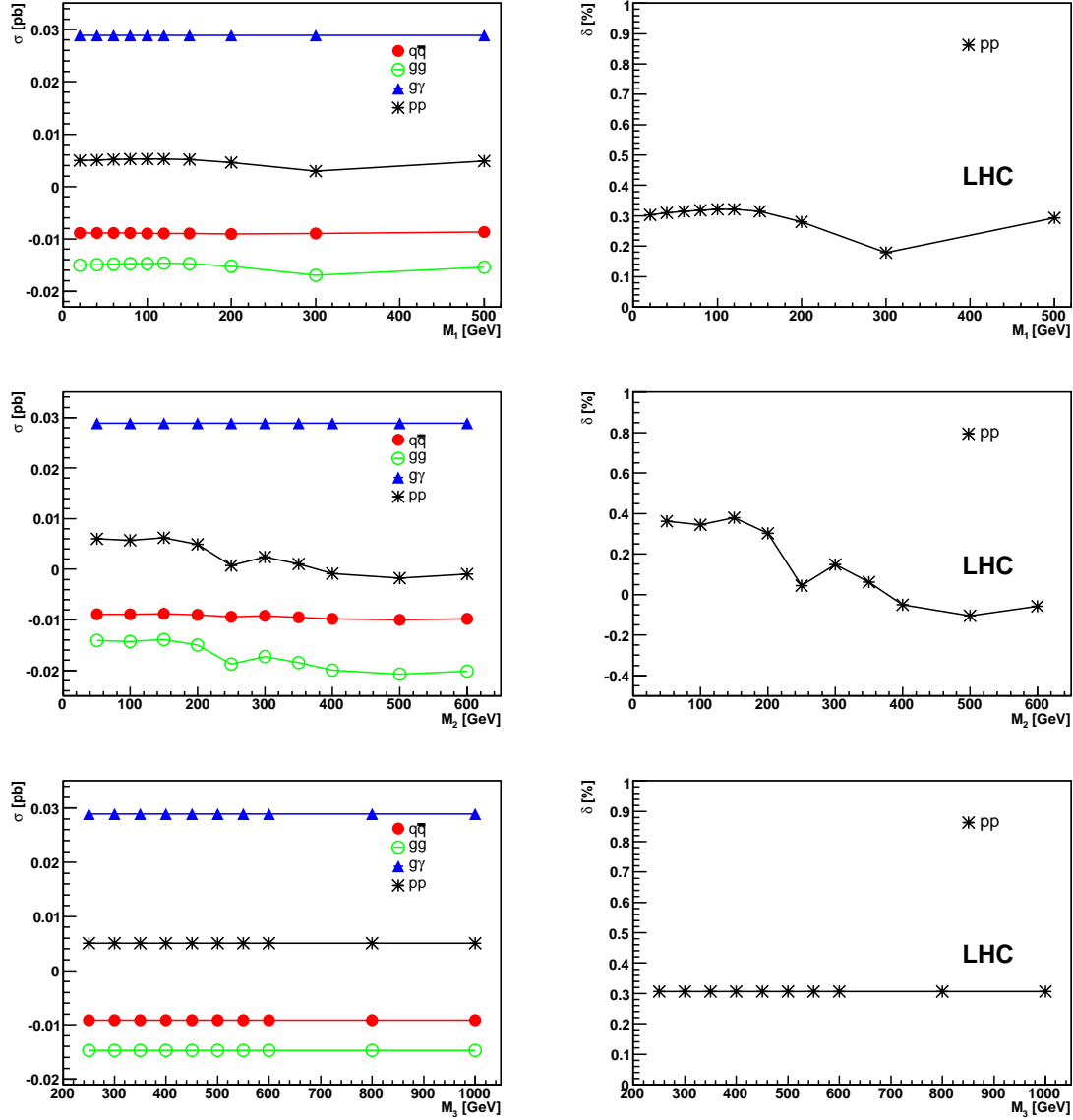
Figure 7.26: Dependence of the NLO SUSY-EW contributions on the variation of the gaugino mass parameters M_1 (top) and M_2 (middle) and the gluino mass M_3 (bottom). Integrated hadronic cross sections for the corrections are shown for all production channels separately and also combined (left). The overall relative correction for pp collisions at the LHC is also given (right).

within this specific scenario. Further increase in $M_{\tilde{q}_T}$ does not have any impact.

In the neutralino and chargino sector (Fig. 7.26), the gaugino mass parameters M_1 and M_2 only enter via loop contributions. For this reason, the variation of the correction is completely flat in $g\gamma$ case and almost flat in the other two channels. The largest impact is visible in the gg channel, again as a result of many loop contributions within this sector. For both parameters, a local minimum is occures near their values
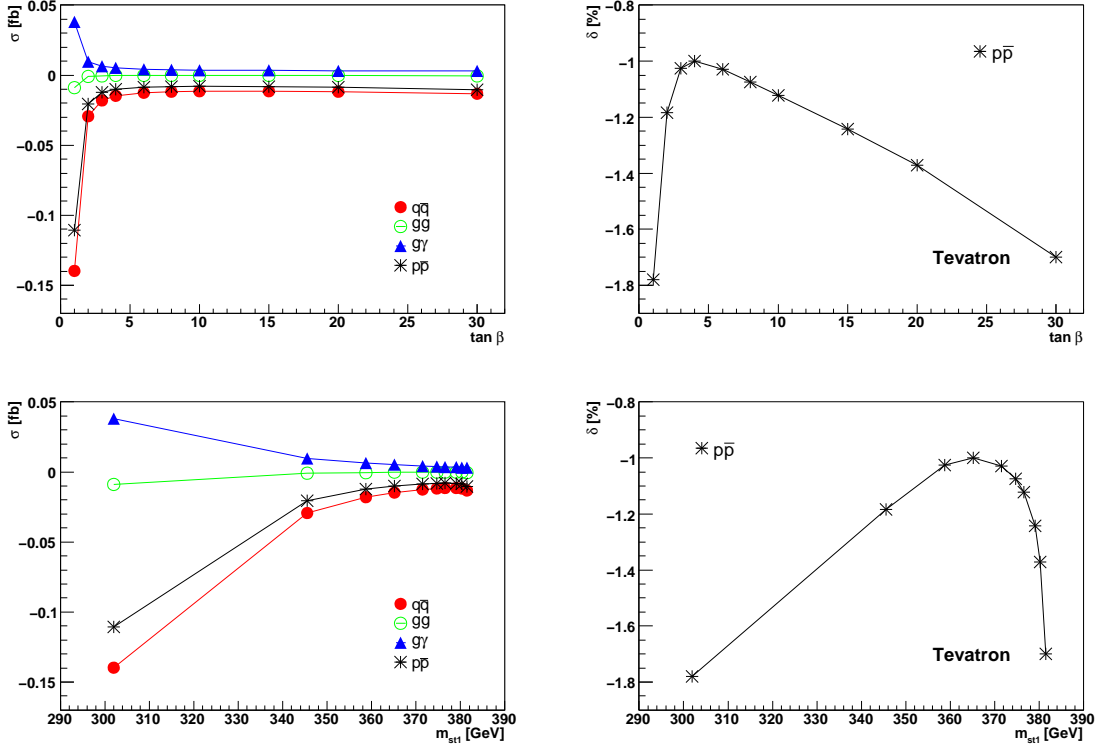
Figure 7.27: Dependence of the NLO SUSY-EW contributions on the variation of $\tan\beta$ (up) and the respective $m_{\tilde{t}_1}$ distribution (down). Integrated hadronic cross sections for the corrections are shown for all production channels separately and also combined (left). The overall relative correction for $p\bar{p}$ collisions at the Tevatron is also given (right).

at the SPS 1a point.

We also study the total hadronic cross section as a function of the gluino mass parameter M_3 (Fig. 7.26 bottom). We can see that there is no dependence since gluinos only contribute to the $\mathcal{O}(\alpha\alpha_{\rm s})$ and $\mathcal{O}(\alpha_{\rm s}^2)$ box diagrams (Figs. 7.11 and 7.14), which vanish in the total cross section.

Figures 7.27 and 7.28 show numerical results obtained for the Tevatron. As the SPS 1a benchmark point yields a relatively heavy top-squark $\tilde{t}_1$, the cross sections are small. We therefore concentrate on the analysis of the parameter dependence since this allows to vary the top-squark masses towards lower values (Fig. 7.23).

Unlike the LHC, the SUSY-EW corrections are negative at the Tevatron and reduce the Born-level cross section. The contribution of $q\bar{q}$ channel is largest here, owing to dominant valence quark densities. It is slightly compensated by the $g\gamma$ contribution, which has opposite sign. The gg channel is suppressed. For small $\tan\beta$, which corresponds to $m_{\tilde{t}_1} \sim 300$ GeV, δ is largest in size ($\sim 1.8\%$). Similar behavior can be
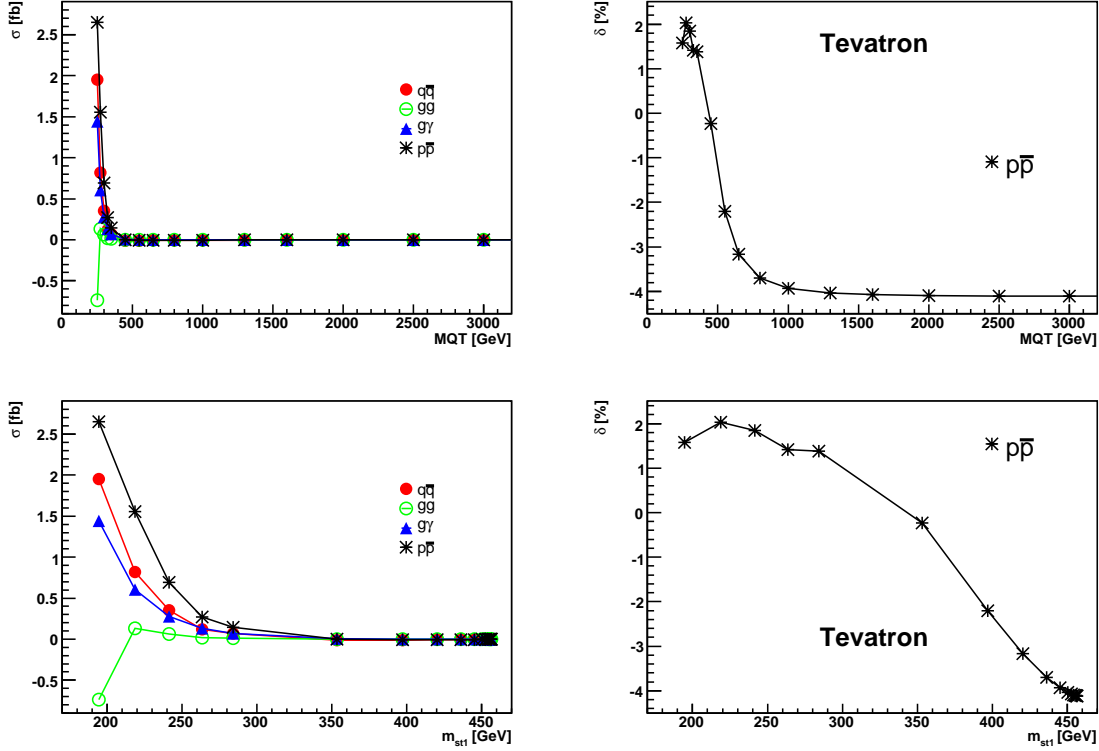
Figure 7.28: Dependence of the NLO SUSY-EW contributions on the variation of the diagonal soft-breaking parameter in the mass matrix of the third squark generation $M_{\tilde{q}_T}$ (up) and the respective $m_{\tilde{t}_1}$ distribution (down). Integrated hadronic cross sections for the corrections are shown for all production channels separately and also combined (left). The overall relative correction for $p\overline{p}$ collisions at the Tevatron is also given (right).

observed for large $\tan\beta$ (Fig. 7.27).

The variation of $M_{\tilde{q}_T}$ allows to go to small values of top-squark mass of about 200 GeV. In this range, δ is positive and enhances the total cross section to about 2%. The cross section decreases for larger masses and, as expected, it is small already at the value corresponding to the SPS 1a point ($m_{\tilde{t}_1} = 376.5$ GeV). Although the saturation at very high $M_{\tilde{q}_T}$ ($m_{\tilde{t}_1} \sim 450$ GeV) corresponds to δ of about 4% in size, the cross section is strongly suppressed by the kinematics.

We can conclude that the most important parameters for the top-squark production studies are those which determine the masses of the third generation of squarks. The overall relative correction becomes of about 2% in size for those values of parameters which yield light $m_{\tilde{t}_1}$.

Chapter 8

Conclusions

Higher order calculations are an important tool for precise theoretical predictions. They allow for testing the Standard Model (SM) as well as its numerous extension candidates. In the searches for new physics the SM processes act as background and in this context, precise understanding of the SM predictions is crucial. Currently, many measurements performed at the Tevatron are already limited to a large extent by the systematics uncertainties. The envisaged high precision at the LHC opens a new rich field in collider phenomenology.

Besides the QCD corrections, which are essential at hadron colliders, also contributions from the electroweak (EW) sector might play some role. In this thesis we have studied the impact of the $\mathcal{O}(\alpha)$ contributions on the cross sections for the top-quark pair production within the SM and for the top-squark pair production within the MSSM. Typically, cross section measurements serve to extract important parameters of the model such as masses of the particles.

In the first part of the thesis we have investigated the top-quark pair production. The measurement of top pair production cross section is a significant test of the SM. The observations of deviations from the SM prediction could indicate a new non-standard production or decay mechanism. Due to higher production rate the measurements in the top quark sector are expected to be more accurate at the LHC than at the Tevatron. Previous theoretical studies of the $t\bar{t}$ production cross section were concentrated on the higher order contributions from the QCD sector, as well as from the weak part of the EW sector. By calculating the photonic part of the EW sector we have completed the SM picture at one-loop level.

QED corrections form a substantial subclass of the complete EW contributions and can be treated separately, independent of the weak part. Due to null photon mass, IR singularities occur in virtual corrections and have to be compensated by including the real corrections. At $\mathcal{O}(\alpha\alpha_{\mathrm{s}}^2)$ also singularities related to gluons have to be

treated in analogy to the photon case. The QED–QCD interference yields additional contributions which are zero at Born-level. Because of negligible masses of initial state quarks, also collinear singularities occur. These have to be handled by means of factorization. For a consistent treatment, parton distribution functions (PDFs) at NLO QED are required. Including the NLO QED effects into the PDFs leads to interesting effects, such as the non-zero photon density in the proton. For this reason, also the photon-induced $t\bar{t}$ production contributes at this order, although it is a completely different process at the partonic level.

We have seen that the QED corrections have negligible impact on the total $t\bar{t}$ cross section since they are at the level of 1%. However, in the case of the differential cross sections, which can be determined with respect to the invariant mass of the $t\bar{t}$ pair $\sqrt{\hat{s}}$, or with respect to the transverse momentum of the top quark p_{T}, the QED corrections are not that small. While the NLO QED effects become important at the LHC only for very high p_{T} and very high $\sqrt{\hat{s}}$, at the Tevatron they are much larger. This is a consequence of the dominant $q\bar{q}$ annihilation subprocess, in which the NLO QED contributions are enhanced by the subleties of QED–QCD interference. At $\sqrt{\hat{s}}$ and p_{T} ranges accessible at the Tevatron, the QED corrections reach above 4% for $\sqrt{\hat{s}} \gtrsim 650$ GeV and $p_{\mathrm{T}} \gtrsim 250$ GeV. As they are negative, they add up with the rest of the EW corrections which are also negative and show similar behavior. Combining our results with the non-photonic EW corrections shows that the complete EW corrections, including the QED part, might reach the level of 10% for high $\sqrt{\hat{s}}$ and high p_{T}, which are still within the range of Tevatron. At the LHC, the QED corrections become negative only for very high $\sqrt{\hat{s}}$ and very high p_{T} and grow much more slowly than the non-photonic EW corrections. Therefore, here they do not represent a significant contribution and only lead to slight enhancement of the non-photonic EW corrections.

In the second part of the thesis, we have focused on the predictions within the minimal supersymmetric extension of the SM, the MSSM. We have analysed the impact of the full set of EW-like contributions on the production cross section of top-squark pairs. Being the superpartner of the top quark, the top-squark is a candidate for the lightest squark in many supersymmetric models, and as such is of particular interest at colliders. The fact that the top-squark pair production cross section depends essentially only on the top-squark mass, and very little on other supersymmetric parameters, allows for direct determination of $m_{\tilde{t}_1}$ from the cross section measurement, in the case of a discovery.

The structure of the SUSY-EW sector is more extended than in the SM leading to a large number (several hundred) of contributing diagrams. Unlike the SM, in the MSSM

the photonic contributions cannot be separated from the rest of the EW contributions owing to the mixing in the gaugino–higgsino sector. IR singularities can, however, be handled in analogy to the SM. We have therefore combined the virtual and real photonic and gluonic corrections in order to compensate the IR singularities. The contibutions from the EW–QCD interference are also considered. The collinear singularities related to the light initial state quarks are factorized and for consistency the PDFs at NLO QED are used. Also the non-zero photon-induced production processes have been included into our analysis. The numerical results are presented for the SPS 1a scenario.

The impact of the SUSY-EW corrections on the total hadronic cross section for the top-squark pair production is only about 1% and thus negligible. Nevertheless, in the differential cross sections, the SUSY-EW corrections relative to the Born-level cross section grow with increasing p_T and $\sqrt{\hat{s}}$ and they are further enhanced by imposing high cuts on p_T. In the very high p_T region, for $p_\mathrm{T} \gtrsim 1200$ GeV, they become larger than 10% and should be taken into account.

We have also studied the soft-breaking parameter dependence of the total hadronic cross section. We have seen that the relative corrections vary mostly with parameters, which directly determine the top-squark mass, such as $\tan\beta$ and $M_{\tilde{q}_T}$. The mass dependence enters not only via the higher order contributions but mostly through the kinematics of the process. The largest effects are therefore related to small values of $\tan\beta$ and $M_{\tilde{q}_T}$, which correspond to small values of $m_{\tilde{t}_1}$. The effects of gaugino mass parameter variation are very small, as they only contribute to SUSY-EW corrections.

We can summarize our results for the EW corrections in the following way: Although the effects on the total hadronic cross sections are very small in both the SM and the MSSM, the situation is different for the differential cross sections. The impact of EW corrections increases with both $\sqrt{\hat{s}}$ and p_T. The photon-induced production rates are comparable in size with other NLO EW contributions and have to be considered. At high p_T and high $\sqrt{\hat{s}}$ the NLO EW corrections cannot be ignored and should therefore be included in the numerical analysis.

Zusammenfassung

Rechnungen in höherer Ordnung Störungstheorie sind ein wichtiges Werkzeug für genaue theoretische Vorhersagen. Sie ermöglichen die Validierung des Standardmodells (SM) und dessen zahlreichen Erweiterungen. Die Messung von Wirkungsquerschnitten dient dazu, wichtige Modell-Parameter wie beispielsweise die Massen von Elementarteilchen zu bestimmen. Abgesehen von QCD-Korrekturen, die an Hadron-Beschleunigern eine tragende Rolle spielen, können auch elektroschwache (EW) Beiträge von Bedeutung sein. In dieser Doktorarbeit wurde der Einfluß der $\mathcal{O}(\alpha)$ Korrekturen auf die Top-Quark Paarproduktion untersucht. Dies geschah im SM und seiner minimal supersymmetrischen Erweiterung, dem MSSM.

Im ersten Teil dieser Arbeit wurde die Top-Quark Produktion in next-to-leading-order (NLO) QED betrachtet. Die Messung des Wirkungsquerschnittes der Top-Quark Produktion ist ein aussagekräftiger Test des SM. Abweichungen von der SM-Vorhersage könnten auf neue Physik, sprich auf eine Erweiterung des SM hindeuten. Bisher waren die Berechnungen der theoretischen Vorhersagen auf den QCD-Sektor und nicht-photonische EW Korrekturen beschränkt.

In dieser Arbeit wurden nun erstmals auch QED-Korrekturen betrachtet. Diese bilden eine Untermenge der EW Korrekturen und können getrennt behandelt werden. Typischerweise treten mit den QED Korrekturen IR-Singularitäten auf, die durch Bremsstrahlungsbeiträge kompensiert werden. Weiter sind auf $\mathcal{O}(\alpha\alpha_{\mathrm{s}}^2)$ QED–QCD Beiträge zu beachten, die auf Born Niveau nicht vorhanden sind. Die NLO Beiträge werden durch solche Korrekturen weiter verstärkt. Für ein konsistentes Vorgehen ist aber auch die Berücksichtigung der NLO QED-Effekte in den Parton-Verteilungsfunktionen von Nöten. Als Folge ist die Photon-Dichte in Protonen ungleich Null und führt zu von Photonen hervorgerufener $t\bar{t}$-Produktion.

Der zweite Teil der Arbeit beschäftigt sich mit dem Einfluß der vollen Klasse von EW Korrekturen zum Wirkungsquerschnitt der Stop-Paarproduktion im Rahmen des MSSM. Stop-Squarks sind die supersymmetrischen Partner-Teilchen der Top-Quarks. Sie sind von besonderem Interesse, da sie ein guter Kandidat für ein mögliches leichtes-tes Squark sind. Der Wirkungsquerschnitt der Paarproduktion von Top-Squarks hängt

hauptsächlich von der Masse der Top-Squarks ab. Somit ist die direkte Bestimmung der Top-Squark Masse über diesen Prozess möglich.

Im Gegensatz zum SM können die QED-Korrekturen im MSSM nicht getrennt von den übrigen EW Korrekturen betrachtet werden. Die IR-Singularitäten werden allerdings in analoger Weise behandelt. Durch Photonen verursachte Produktionskanäle und Beiträge durch EW–QCD Interferenz tragen in EW NLO ebenfalls bei.

Es wurde gezeigt, dass obwohl die Korrekturen zu den totalen Wirkungsquerschnitten klein sind, die EW Korrekturen erheblich zu den differentiellen Wirkungsquerschnitten beitragen können. Die von den Photonen herrührenden Produktions-Raten sind numerisch vergleichbar mit den übrigen NLO Beträgen und dürfen nicht vernachlässigt werden. In Bereichen mit großem p_T und hoher invarianter Masse, die am LHC und dem Tevatron erreichbar sind, sind die NLO EW Korrekturen von Bedeutung und sollten in die numerischen Analysen eingeschlossen werden.

Appendix A

Choice of parameters

A.1 Standard Model Parameters

The current values of the Standard Model parameters are given in the following [5]

- Coupling constants:

$$\alpha^{-1} = 137.03599911 \qquad \alpha_s(M_Z) = 0.1176$$

- Masses:

    Gauge bosons:

$$M_W = 80.403 \text{ GeV} \qquad M_Z = 91.1876 \text{ GeV} \qquad m_\gamma = m_g = 0$$

    Leptons:

$$m_e = 510.999 \text{ keV} \qquad m_\mu = 105.658 \text{ MeV} \qquad m_\tau = 1.777 \text{ GeV}$$

$$m_{\nu_e} = 0 \qquad m_{\nu_\mu} = 0 \qquad m_{\nu_\tau} = 0$$

    Quarks:

$$m_u = 53.8 \text{ MeV} \qquad m_c = 1.5 \text{ GeV} \qquad m_t = 171.4 \text{ GeV}$$

$$m_d = 53.8 \text{ MeV} \qquad m_s = 150 \text{ MeV} \qquad m_b = 4.7 \text{ GeV}$$

The masses of the light flavor quarks, m_u, m_d and m_s, are effective parameters, chosen to reproduce the hadronic vaccum polarization of the photon. The masses of the first two generations of quarks are set to zero during the calculations whenever possible.

A.2 SPS 1a parameter set of the MSSM

Although some regions in the parameter space of the MSSM can be eliminated by imposing experimental constraints or are disfavored by theoretical arguments, the choice still remains very large. In order to unify the conventions used in the calculations and thus allow for comparison of independently obtained results, efforts were made to establish certain points in the MSSM parameter space as benchmarks scenarios. The Snowmass points and slopes (SPS) are benchmarks scenarios which were suggested in [146, 147]. They provide parameter sets which illustrate characteristic features of various SUSY breaking scenarios, such as minimal gravity-mediated (mSUGRA), gauge-mediated (GMSB) or anomaly-mediated (AMSB) SUSY breaking scenarios.

The SPS 1a point [147], defined in the framework of mSUGRA scenario, is a very popular benchmark point, often used for numerical studies. It is similar to the SPS 1a' point defined in [148], which is slightly changed to comply with the measured dark matter density. The mSUGRA scenario is characterized by four parameters. These are a common scalar mass M_0, a common gaugino mass $M_{1/2}$, a common trilinear coupling A_0 and the ratio of the vacuum expectation values of the two Higgs doublets $\tan \beta$. In addition, the sign of the Higgs mass parameter μ is not fixed and can be chosen freely. All parameters are real, unification of gauge couplings is assumed at the GUT scale, and the soft-breaking terms are universal at the high-energy scale. For SPS1a the values of the high-energy parameters are:

$$M_0 = 100 \text{GeV} , \quad M_{1/2} = 250 \text{GeV} , \quad A_0 = -100 \text{GeV} ,$$
$$\tan \beta = 10 , \quad \text{sign}(\mu) = +1 . \tag{A.1}$$

The mass parameters are defined at the GUT scale and then evolved via renormalization group equations (RGEs) to the low-energy scale, at which also $\tan \beta$ is specified. All mass parameters are defined in the $\overline{\text{DR}}$-scheme at the scale $Q = 454.7$ GeV. The values of the low-energy Higgs sector and gaugino sector parameters read

$$M_{\tilde{g}} = 595.2 \text{GeV} , \quad \mu = 352.4 \text{GeV} , \quad M_A = 393.6 \text{GeV} ,$$
$$\tan \beta = 10 , \quad M_1 = 99.1 \text{GeV} , \quad M_2 = 192.7 \text{GeV} , \tag{A.2}$$

where $M_{\tilde{g}}$ denotes the gluino mass, M_A is the mass of CP-odd Higgs boson, and M_1 and M_2 are gaugino mass parameters. The soft SUSY breaking parameters in the diagonal entries of the squark and slepton mass matrices of the first and second generation are chosen to be the same. The off-diagonal entries have been neglected, i.e. there is no sfermion mixing in the first two generations. The values of the diagonal parameters
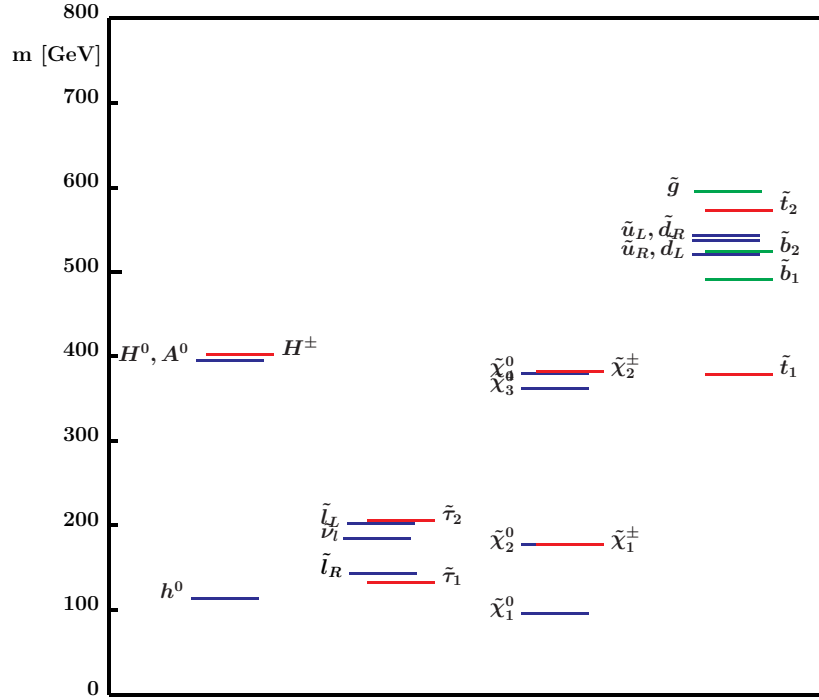
Figure A.1: The SUSY particle spectrum for the benchmark point corresponding to SPS 1a [146, 147].

are (the index i in $M_{\tilde{q}i_L}$ refers to the generation):

$$M_{\tilde{q}1_L} = M_{\tilde{q}2_L} = 539.9\text{GeV} , \quad M_{\tilde{d}_R} = 519.5\text{GeV} , \quad M_{\tilde{u}_R} = 521.7\text{GeV} ,$$
$$M_{\tilde{e}_L} = 196.6\text{GeV} , \quad M_{\tilde{e}_R} = 136.2\text{GeV} . \tag{A.3}$$

The soft SUSY breaking parameters in the diagonal entries of the squark and slepton mass matrices of the third generation have the following values,

$$M_{\tilde{q}3_L} = 495.9\text{GeV} , \quad M_{\tilde{b}_R} = 516.9\text{GeV} , \quad M_{\tilde{t}_R} = 424.8\text{GeV} ,$$
$$M_{\tilde{\tau}_L} = 195.8\text{GeV} , \quad M_{\tilde{\tau}_R} = 133.6\text{GeV} , \tag{A.4}$$

while the trilinear couplings appearing in the off-diagonal entries are

$$A_t = -510.0\text{GeV} , \quad A_b = -772.7\text{GeV} , \quad A_\tau = -254.2\text{GeV} . \tag{A.5}$$

The corresponding SUSY particle spectrum is shown in Fig. A.1.

In our numerical studies, we use the $\overline{\text{DR}}$-scheme parameters as on-shell scheme parameters. At one-loop level, the difference between these two renormalization schemes yields only finite contributions. These result into small shifts in the physical masses of the particles which have negligible numerical impact on our analysis.

Appendix B

Basic principles of supersymmetry

B.1 Conventions

As a generalization of the vector space coordinates in three-dimensional Euclidean space, each point in four-dimensional Minkowski space is determined by a contravariant four-vector

$$x^\mu = \left(x^0, x^1, x^2, x^3\right) = (t, \vec{x}) \ . \tag{B.1}$$

Using the metric tensor

$$g_{\mu\nu} = g^{\mu\nu} = \text{diag}\,(1, -1, -1, -1) \ , \tag{B.2}$$

also a covariant four-vector can be defined as

$$x_\mu = g_{\mu\nu}x^\mu = (t, -\vec{x}) \ . \tag{B.3}$$

From now on the Greek indices run from 0 to 3 while the Latin indices run from 1 to 3. We adopt the Einstein's sum convention, i.e the same two indices, one as covariant the other as contravariant, are being summed over. In addition, the natural units of $\hbar = c = 1$ are used.

We define the following abbreviations for the derivatives with respect to the generalized space coordinates:

$$\partial_\mu := \frac{\partial}{\partial x^\mu} = \left(\frac{\partial}{\partial t}, \vec{\nabla}\right) \ , \qquad \partial^\mu := \frac{\partial}{\partial x_\mu} = \left(\frac{\partial}{\partial t}, -\vec{\nabla}\right) \ . \tag{B.4}$$

The momentum four-vector is given by

$$p^\mu = i\partial^\mu = (E, \vec{p}) \ . \tag{B.5}$$

B.2   Spinors

B.2.1   Weyl spinors

Weyl spinors are defined as two-component anticommuting objects which transform under the Lorentz transformations Λ in the following way

$$
\begin{aligned}
\psi_\alpha &\rightarrow M(\Lambda)_\alpha{}^\beta \psi_\beta \ , \\
\bar\psi^{\dot\alpha} &\rightarrow \left((M(\Lambda)^{-1})^+\right)^{\dot\alpha}{}_{\dot\beta} \bar\psi^{\dot\beta} \ ,
\end{aligned}
\tag{B.6}
$$

with 2×2 complex matrices M given as

$$
\begin{aligned}
M(\Lambda) &= \left(e^{-\frac{i}{2}\omega_{\mu\nu}\frac{\sigma^{\mu\nu}}{2}}\right) \ , \\
(M^{-1})^+(\Lambda) &= \left(e^{-\frac{i}{2}\omega_{\mu\nu}\frac{\bar\sigma^{\mu\nu}}{2}}\right) \ .
\end{aligned}
\tag{B.7}
$$

Here $\omega_{\mu\nu}$ is an antisymmetric tensor, and spinor indices can take values 1 and 2. The tensors $\sigma^{\mu\nu}$ and $\bar\sigma^{\mu\nu}$ are defined as

$$
(\sigma^{\mu\nu})_\alpha{}^\beta = \frac{i}{2}\left(\sigma^\mu\bar\sigma^\nu - \sigma^\nu\bar\sigma^\mu\right)_\alpha{}^\beta \ , \qquad\qquad (\bar\sigma^{\mu\nu})^{\dot\alpha}{}_{\dot\beta} = \frac{i}{2}\left(\bar\sigma^\mu\sigma^\nu - \bar\sigma^\nu\sigma^\mu\right)^{\dot\alpha}{}_{\dot\beta} \ ,
\tag{B.8}
$$

where σ^μ and $\bar\sigma^\mu$ are Pauli matrices, generalized in four dimensions

$$
\sigma^\mu_{\alpha\dot\beta} = \left(\mathbb{1}, \sigma^k\right)_{\alpha\dot\beta} \ , \qquad\qquad \bar\sigma^{\mu\dot\alpha\beta} = \left(\mathbb{1}, -\sigma^k\right)^{\dot\alpha\beta} \ .
\tag{B.9}
$$

The three-dimensional Pauli matrices σ^k are given by

$$
\sigma^1 = \begin{pmatrix} 0 & 1 \\ 1 & 0 \end{pmatrix} \ , \qquad \sigma^2 = \begin{pmatrix} 0 & -i \\ i & 0 \end{pmatrix} \ , \qquad \sigma^3 = \begin{pmatrix} 1 & 0 \\ 0 & -1 \end{pmatrix} \ .
\tag{B.10}
$$

The Weyl spinors satisfy the following relations

$$
\begin{aligned}
\psi_\alpha = \epsilon_{\alpha\beta}\,\psi^\beta \qquad &\text{and} \qquad \psi^\alpha = \epsilon^{\alpha\beta}\,\psi_\beta \ , \\
\bar\psi_{\dot\alpha} = \epsilon_{\dot\alpha\dot\beta}\,\bar\psi^{\dot\beta} \qquad &\text{and} \qquad \bar\psi^{\dot\alpha} = \epsilon^{\dot\alpha\dot\beta}\,\bar\psi_{\dot\beta} \ ,
\end{aligned}
\tag{B.11}
$$

with ϵ being the totally antisymmetric tensor which is in two-dimensions:

$$
\begin{aligned}
\left(\epsilon^{\alpha\beta}\right) &:= \begin{pmatrix} 0 & 1 \\ -1 & 0 \end{pmatrix} \ , \qquad \left(\epsilon_{\alpha\beta}\right) := \begin{pmatrix} 0 & -1 \\ 1 & 0 \end{pmatrix} \ , \\
\left(\epsilon^{\dot\alpha\dot\beta}\right) &:= \begin{pmatrix} 0 & 1 \\ -1 & 0 \end{pmatrix} \ , \qquad \left(\epsilon_{\dot\alpha\dot\beta}\right) := \begin{pmatrix} 0 & -1 \\ 1 & 0 \end{pmatrix} \ .
\end{aligned}
\tag{B.12}
$$

With help of the Weyl spinor formalism the Dirac equation can be rewritten in two-component notation as

$$
(\bar\sigma_\mu p^\mu)^{\dot\alpha\beta}\,\psi_\beta = m\bar\psi^{\dot\alpha} \ , \qquad\qquad (\sigma_\mu p^\mu)_{\alpha\dot\beta}\,\bar\psi^{\dot\beta} = m\psi_\alpha \ .
\tag{B.13}
$$

B.2.2 Dirac and Majorana spinors

Two-component Weyl spinors can be combined into four-component spinor objects in the following way

$$\Psi = \begin{pmatrix} \psi_\alpha \\ \bar{\chi}^{\dot\alpha} \end{pmatrix} , \qquad \bar\Psi = \begin{pmatrix} \chi^\alpha & \bar\psi_{\dot\alpha} \end{pmatrix} . \tag{B.14}$$

If $\psi = \chi$, Ψ denotes a Majorana spinor, otherwise Ψ is a Dirac spinor. The four-component equivalents of the Pauli σ matrices are the Dirac γ matrices. They are defined by means of the Clifford algebra as

$$\{\gamma^\mu, \gamma^\nu\} = \gamma^\mu\gamma^\nu + \gamma^\nu\gamma^\mu = 2g^{\mu\nu} . \tag{B.15}$$

In addition, γ^5 is introduced by

$$\begin{aligned}
\gamma^5 &= i\gamma^0\gamma^1\gamma^2\gamma^3 = -\frac{i}{4!}\epsilon_{\mu\nu\rho\sigma}\gamma^\mu\gamma^\nu\gamma^\rho\gamma^\sigma , \\
\{\gamma^\mu, \gamma^5\} &= 0 , \\
(\gamma^5)^2 &= 0 ,
\end{aligned} \tag{B.16}$$

with $\epsilon_{\mu\nu\rho\sigma}$ being the totally antisymmetric tensor in four dimensions given by

$$\epsilon_{\mu\nu\rho\sigma} = \begin{cases} +1 & \text{for even permutation of } \{0,1,2,3\} \\ -1 & \text{for odd permutation of } \{0,1,2,3\} \\ 0 & \text{otherwise} \end{cases} \tag{B.17}$$

The choice of γ matrices which satisfy Eq. (B.15-B.16) is not unique. In the so-called chiral representation they are expressed as

$$\gamma^\mu = \begin{pmatrix} 0 & \sigma^\mu \\ \bar\sigma^\mu & 0 \end{pmatrix} , \qquad \gamma^5 = \begin{pmatrix} -\mathbb{1} & 0 \\ 0 & \mathbb{1} \end{pmatrix} , \tag{B.18}$$

with σ^μ, $\bar\sigma^\mu$ as given in Eq. (B.9). The 4×4 tensor matrices $\sigma^{\mu\nu}$ can be constructed from the γ matrices:

$$\sigma^{\mu\nu} = \frac{i}{2}[\gamma^\mu, \gamma^\nu] . \tag{B.19}$$

With help of γ^5 it is possible to define the projection operators

$$\omega_- \equiv \frac{1-\gamma^5}{2} = \begin{pmatrix} 1 & 0 \\ 0 & 0 \end{pmatrix} , \qquad \omega_+ \equiv \frac{1+\gamma^5}{2} = \begin{pmatrix} 0 & 0 \\ 0 & 1 \end{pmatrix} , \tag{B.20}$$

which project a Dirac spinor into its left-handed or right-handed component as

$$\omega_-\Psi = \begin{pmatrix} \psi_\alpha \\ 0 \end{pmatrix} \quad \text{and} \quad \omega_+\Psi = \begin{pmatrix} 0 \\ \bar\chi^{\dot\alpha} \end{pmatrix} . \tag{B.21}$$

Using the four-component notation the Dirac equation of Eq. (B.13) can be rewritten as

$$(\gamma_\mu p^\mu - m)\,\Psi \equiv (\not{p} - m) = 0 . \tag{B.22}$$

B.3 Superfields

B.3.1 Grassmann variables

Grassmann variables have fermionic character, i.e. they anticommute with all variables which also have fermionic character:

$$\{\theta, \xi\} = 0 \ . \tag{B.23}$$

In particular, the square of a Grassmann number is zero.

Grassmann numbers form an Abelian group with respect to the operation of addition. As concerns the multiplication with ordinary complex numbers, same distributive laws hold as for the scalar multiplication of a vector.

The integral over Grassmann numbers is defined as

$$\int d\theta (A + B\theta) = B \ , \tag{B.24}$$

where A and B are complex numbers. Analogously, the differentiation with respect to Grassmann numbers is given by

$$\frac{\partial}{\partial \theta}(A + B\theta) = B \ . \tag{B.25}$$

Complex Grassmann numbers can be built out of real and imaginary Grassmann parts. It is convenient to define the operation of complex conjugation in such a way that the product is reversed, as it is the case for hermitian conjugation of matrices:

$$(\theta\xi)^* = \xi^*\theta^* = -\theta^*\xi^* \ . \tag{B.26}$$

The complex Grassmann numbers θ and θ^* are treated as independent variables during integration

$$\int d\theta d\theta^* = \theta^*\theta = 1 \ . \tag{B.27}$$

Using the Grassmann variables enables to rewrite the superalgebra in the following way

$$\begin{aligned}
[\theta^\alpha Q_\alpha, \bar{Q}_{\dot\beta}\bar\theta^{\dot\beta}] &= 2\theta^\alpha \sigma^\mu_{\alpha\dot\beta}\bar\theta^{\dot\beta} P^\mu \ , \\
[\theta^\alpha Q_\alpha, \theta^\beta Q_\beta] &= [\bar{Q}_{\dot\alpha}\bar\theta^{\dot\alpha}, \bar{Q}_{\dot\beta}\bar\theta^{\dot\beta}] = 0 \ ,
\end{aligned} \tag{B.28}$$

which is very convenient for the formalism of superfields.

B.3.2 Chiral and vector superfields

In general a finite supersymmetric transformation is given, in complete analogy to the non-Abelian gauge transformations $e^{i\phi_\alpha T^\alpha}$, by the group element

$$G(x_\mu, \theta^\alpha, \bar{\theta}_{\dot{\alpha}}) = e^{i\{x_\mu P^\mu + \theta^\alpha Q_\alpha + \bar{\theta}_{\dot{\alpha}} \bar{Q}^{\dot{\alpha}}\}} , \tag{B.29}$$

where P^μ, Q_α and $\bar{Q}^{\dot{\alpha}}$ are the generators of the supersymmetry group. The variables x_μ, θ^α and $\bar{\theta}_{\dot{\alpha}}$ build the superspace with supercoordinate $z = (x_\mu, \theta^\alpha, \bar{\theta}_{\dot{\alpha}})$.

The formalism of superfields is a natural extension of the standard field formalism from the four-dimensional Minkowski space to the superspace. The superfields Φ must be therefore functions of all superspace variables $x_\mu, \theta^\alpha, \bar{\theta}_{\dot{\alpha}}$. The superfields can be expanded into component fields. Due to the anticommuting nature of Grassmann variables, this expansion truncates after few finite terms as

$$\begin{aligned} \Phi(x, \theta, \bar{\theta}) &= f(x) + \theta\phi(x) + \bar{\theta}\bar{\chi}(x) \\ &\quad + \theta\theta m(x) + \bar{\theta}\bar{\theta}n(x) + \theta\sigma^\mu\bar{\theta}\nu_\mu(x) \\ &\quad + \theta\theta\bar{\theta}\bar{\lambda}(x) + \bar{\theta}\bar{\theta}\theta\psi(x) + \theta\theta\bar{\theta}\bar{\theta}d(x) . \end{aligned} \tag{B.30}$$

Here f, m, n, d are scalar fields, ϕ, χ, λ, ψ are spinor fields, and ν_μ is a vector field. In general a superfield has 16 real fermionic and 16 real bosonic degrees of freedom.

Chiral and antichiral superfields are defined by the following conditions

$$\bar{D}_{\dot{\alpha}}\Phi(z) = 0 \qquad \text{or} \qquad D_\alpha\bar{\Phi} = 0 , \tag{B.31}$$

respectively. The covariant derivatives D_α, $\bar{D}_{\dot{\alpha}}$ are given by

$$\bar{D}_{\dot{\alpha}} = \partial_\alpha - i_\alpha(\sigma_\mu\tilde{\theta})\partial^\mu \qquad \text{or} \qquad D_\alpha = \bar{\partial}_{\dot{\alpha}} + i(\theta\sigma_\mu)_{\dot{\alpha}}\partial^\mu , \tag{B.32}$$

The component field expansion of a chiral superfield gives

$$\begin{aligned} \Phi(z) &= A(x) - i\theta\sigma^\mu\tilde{\theta}\partial_\mu A(x) - \frac{1}{4}\theta\theta\bar{\theta}\bar{\theta}\partial^\mu\partial_\mu A(x) \\ &\quad + \theta^\alpha\sqrt{2}\psi(x)_\alpha - \frac{i}{\sqrt{2}}\theta\theta\bar{\theta}\bar{\sigma}^\mu\partial_\mu\psi(x) + \theta\theta F(x) , \end{aligned} \tag{B.33}$$

where A, F are scalar fields and ψ is a left-handed spinor.

Vector superfields satisfy the relation

$$V^+(z) = V(z) . \tag{B.34}$$

The component field expansion of a vector superfield can be written in the following form:

$$
\begin{aligned}
V(z) \;=\; & C(x) + \theta\chi(x) + \tilde{\theta}\tilde{\chi}(x) + i\theta\theta M(x) - \bar{\theta}\bar{\theta}M^*(x) \\
& + \theta\sigma^\mu\bar{\theta}v_\mu + i\theta\theta\bar{\theta}\bar{\lambda}(x) + \frac{1}{2}\theta\theta\bar{\theta}\bar{\theta}D(x) \; .
\end{aligned}
\tag{B.35}
$$

with

$$
C^*(x) = C(x) \qquad , \qquad v_\mu^+ = v_\mu \qquad , \qquad D^*(x) = D(x) \; .
\tag{B.36}
$$

Here C, D are real scalar fields, M is a complex scalar field, χ and λ are spinor fields and v_μ is a real vector field. With help of the Wess-Zumino gauge [149] the unphysical degrees of freedom of C, M and χ can be eliminated.

In general, a supersymmetric non-Abelian gauge transformation of a vector superfield is defined as follows,

$$
e^{2gV} \rightarrow e^{-i2g\bar{\Lambda}}e^{2gV}e^{i2g\Lambda} \; ,
\tag{B.37}
$$

where g is the gauge coupling, Λ is a chiral superfield and V is a vector superfield. The generators of the gauge group, T^a, enter in the following way:

$$
\Lambda(z) = \Lambda^a(z)\,T^a \qquad \text{and} \qquad V(z) = V^a(z)\,T^a \; .
\tag{B.38}
$$

The gauge transformations of chiral and antichiral superfields can be introduced as follows,

$$
\Phi \rightarrow e^{-i2g\Lambda}\Phi \qquad \text{and} \qquad \bar{\Phi} \rightarrow \bar{\Phi}e^{i2g\bar{\Lambda}} \; .
\tag{B.39}
$$

B.4 Supersymmetric Lagrangian

The action of a supersymmetric Lagrangian must remain invariant under the supersymmetry transformations. This requirement is satisfied if the Lagrangian acts as total derivative under the supersymmetry transformations. The $\theta\theta$ and $\theta\theta\bar{\theta}\bar{\theta}$ components of chiral and vector superfields, the F and D terms, respectively, manifest this behavior. Therefore the supersymmetric Lagrangian consists of two parts

$$
\mathcal{L} = \int d^2\theta\mathcal{L}_F + \int d^2\theta d^2\bar{\theta}\mathcal{L}_D \; .
\tag{B.40}
$$

In order to build the supersymmetric Lagrangian, appropriate candidates among the chiral and vector superfield combinations have to be selected. Product of two or three

chiral superfields results in a chiral superfield and contributes to $\mathcal{L}_F$. Higher multiples are not suitable because of the requirement of renormalizability. The product of a chiral and an antichiral superfield leads to a vector superfield and thus contributes to $\mathcal{L}_D$. In the following, we present explicit contributions to a general supersymmetric Lagrangian:

(i) contributions originating from the superpotential:

$$
\begin{aligned}
\Phi_i(z)|_{\theta\theta} &= F_i \\
\Phi_i(z)\Phi_j(z)|_{\theta\theta} &= A_i F_j + A_j F_i - \psi_i \psi_j \\
\Phi_i(z)\Phi_j(z)\Phi_k(z)|_{\theta\theta} &= A_i A_j F_k + A_i F_j A_k + F_i A_j A_k \\
&\quad - A_i(\psi_j \psi_k) - \psi_i A_j \psi_k - (\psi_i \psi_j) A_k \ , \quad\quad \text{(B.41)}
\end{aligned}
$$

where Φ_i is a chiral superfield.

(ii) kinetic terms of the matter fields:

$$
\begin{aligned}
\bar{\Phi}_k \Phi_k|_{\theta\theta\bar{\theta}\bar{\theta}} &= \Big[(\partial_\mu A_k^+)(\partial^\mu A_k) + \frac{i}{2}(\bar{\psi}_k \bar{\sigma}^\mu \partial_\mu \psi_k) + \frac{i}{2}(\psi_k \sigma^\mu \partial_\mu \bar{\psi}_k) \\
&\quad + F_k^+ F_k \Big] \\
\bar{\Phi}_k e^{2gV} \Phi_k|_{\theta\theta\bar{\theta}\bar{\theta}} &= (\partial_\mu A_k^+ - ig_k A_k^+ v_\mu)(\partial^\mu A_k + ig_k v^\mu A_k) \\
&\quad + i\left[\bar{\psi}_k \bar{\sigma}^\mu (\partial_\mu + ig_k v_\mu) \psi_k \right] - i\sqrt{2} g_k(\bar{\psi}_k \bar{\lambda} A_k - A_k^+ \lambda \psi_k) \\
&\quad + g_k A_k^+ D A_k + F_k^+ F_k \\
&= (D_\mu A_k)^+(D^\mu A_k) + i\bar{\psi}_k \bar{\sigma}^\mu D_\mu \psi_k \\
&\quad - i\sqrt{2} g_k(\bar{\psi}_k \bar{\lambda} A_k - A_k^+ \lambda \psi_k) + g_k A_k^+ D A_k \\
&\quad + F_k^+ F_k \ . \quad\quad\quad\quad\quad\quad\quad\quad\quad\quad\quad\quad\quad \text{(B.42)}
\end{aligned}
$$

Here Φ_k is a chiral superfield and V denotes a vector superfield in the Wess-Zumino gauge. Furthermore, in the last step we have introduced the covariant derivative

$$
D_\mu := \partial_\mu + ig_k v_\mu \equiv \partial_\mu + ig_k v_\mu^a T^a \ . \quad\quad\quad\quad\quad\quad \text{(B.43)}
$$

(iii) kinetic terms of the gauge fields:

$$
\frac{1}{16g^2} \left([W^{a\alpha} W_\alpha^a]|_{\theta\theta} + \text{h.c.}\right) = -\frac{1}{4}(F_{\mu\nu}^a)^2 + i\bar{\lambda}^a \bar{\sigma}^\mu (D_\mu \lambda)^a + \frac{1}{2} D^a D^a \ , \quad \text{(B.44)}
$$

where W_α^a denotes the field strength tensor of the vector field V, defined as follows,

$$W_\alpha^a = -\frac{1}{4}\bar{D}\bar{D}\left(e^{-2gV}D_\alpha e^{2gV}\right) \tag{B.45}$$

with

$$F_{\mu\nu}^a = v_{\mu\nu}^a - ig\left((T^{\mathrm{adj}})^b\right)^{ac} v_\mu^b v_\nu^c = v_{\mu\nu}^a + ig\left((T^{\mathrm{adj}})^a\right)^{bc} v_\mu^b v_\nu^c . \tag{B.46}$$

Here $F_{\mu\nu}^a$ is the non-Abelian field strength tensor, which contains the generators of the gauge group $(T^{\mathrm{adj}})^a$ in the adjoint representation, and $v_{\mu\nu} = \partial_\mu v_\nu - \partial_\nu v_\mu$.

The two component auxiliary fields F and D do not have any physical meaning since they do not lead to any kinetic terms within the Lagrangian. As a consequence, their equations of motions are very simple

$$\frac{\partial \mathcal{L}}{\partial F_i} = 0 \qquad \text{and} \qquad \frac{\partial \mathcal{L}}{\partial D^a} = 0 , \tag{B.47}$$

and can easily be solved

$$F_i^+ = -\frac{\partial W(A)}{\partial A_i} \qquad \text{and} \qquad D^a = -A^+ g T^a A . \tag{B.48}$$

Inserting these relations into Eqs. (B.41-B.44) allows to eliminate F and D.

Appendix C

Parton densities

C.1   LO splitting functions

The leading order (LO) terms of the DGLAP splitting functions, which are shown schematically in Fig. 5.3, are given in the following:

$$
\begin{aligned}
P_{qq}(z) &= \frac{4}{3}\left[\frac{1+z^2}{(1-z)_+} + \frac{3}{2}\delta(1-z)\right] , \\
P_{qg}(z) &= \frac{1}{2}\left[z^2 + (1-z)^2\right] , \\
P_{gq}(z) &= \frac{4}{3}\left[\frac{1+(1-z)^2}{z}\right] , \\
P_{gg}(z) &= 6\left[\frac{1-z}{z} + \frac{z}{(1-z)_+} + z(1-z)\right] + \frac{33-2n_f}{6}\delta(1-z) .
\end{aligned}
$$

(C.1)

Here n_f denotes the number of active flavors and the +-prescription is defined, as follows

$$
\begin{aligned}
\frac{1}{(1+z)_+} &= \frac{1}{(1-z)} \quad \text{for} \quad z < 1 , \quad \text{and} \\
\int_0^1 dz \frac{f(z)}{(1-z)_+} &= \int_0^1 dz \frac{f(z)-f(1)}{1-z} .
\end{aligned}
$$

(C.2)

C.2   QED-modified DGLAP evolution equations

The QED-corrected evolution equations for the parton distributions inside the proton, including the photon-parton distribution, at leading order in both α_s and α are

$$
\begin{aligned}
\frac{\partial q_i(x, Q^2)}{\partial \ln Q^2} &= \frac{\alpha_\mathrm{s}}{2\pi} \int_x^1 \frac{dy}{y} \left\{ P_{qq}(y) q_i(\frac{x}{y}, Q^2) + P_{qg}(y) g(\frac{x}{y}, Q^2) \right\} \\
&+ \frac{\alpha}{2\pi} \int_x^1 \frac{dy}{y} \left\{ \tilde{P}_{qq}(y) e_i^2 q_i(\frac{x}{y}, Q^2) + P_{q\gamma}(y) e_i^2 \gamma(\frac{x}{y}, Q^2) \right\} \\
\frac{\partial g(x, Q^2)}{\partial \ln Q^2} &= \frac{\alpha_\mathrm{s}}{2\pi} \int_x^1 \frac{dy}{y} \left\{ P_{gq}(y) \sum_j q_j(\frac{x}{y}, Q^2) + P_{gg}(y) g(\frac{x}{y}, Q^2) \right\} \\
\frac{\partial \gamma(x, Q^2)}{\partial \ln Q^2} &= \frac{\alpha}{2\pi} \int_x^1 \frac{dy}{y} \left\{ P_{\gamma q}(y) \sum_j e_j^2 q_j(\frac{x}{y}, Q^2) + P_{\gamma\gamma}(y) \gamma(\frac{x}{y}, Q^2) \right\} \, , \quad \text{(C.3)}
\end{aligned}
$$

where

$$
\begin{aligned}
\tilde{P}_{qq} &= C_F^{-1} P_{qq} \, , & P_{\gamma q} &= C_F^{-1} P_{gq} \, , \\
P_{q\gamma} &= T_R^{-1} P_{qg} \, , & P_{\gamma\gamma} &= -\frac{2}{3} \sum_i e_i^2 \delta(1-y)
\end{aligned}
\quad \text{(C.4)}
$$

and momentum is conserved:

$$
\int_0^1 dx \, x \left\{ \sum_i q_i(x, Q^2) + g(x, Q^2) + \gamma(x, Q^2) \right\} = 1 \, . \tag{C.5}
$$

The choice of the factorization scales $\mu_{f(QCD)}^2 = \mu_{f(QED)}^2 = Q^2$ is conventional for DIS processes.

Appendix D

Loop integrals

In the following we introduce basic notations and conventions for the calculation of one-loop integrals. We focus on integrals which are relevant for this thesis.

A general one-loop integral can be defined as

$$T^N_{\mu_1,\ldots,\mu_P} = \frac{(2\pi\mu)^{4-D}}{i\pi^2} \int d^D q \frac{q_{\mu_1}\ldots q_{\mu_P}}{[q^2 - m_1^2][(q+k_1)^2 - m_2^2]\ldots[(q+k_{N-1})^2 - m_N^2]} ,$$
(D.1)

where the momenta in the denominator, k_i, are related to the external momenta, p_i, as follows,

$$k_1 = p_1 , \quad k_2 = p_1 + p_2 , \quad \ldots \quad k_N = \sum_{i=1}^{N} p_i .$$
(D.2)

The integral is given in D-dimensions as requested by the dimensional regularization and dimensional reduction. In the latter case the integrals are kept D-dimensional although the algebra is performed in four dimensions. The renormalization scale μ is introduced in order to preserve the same dimension of the integral as in four dimensions.
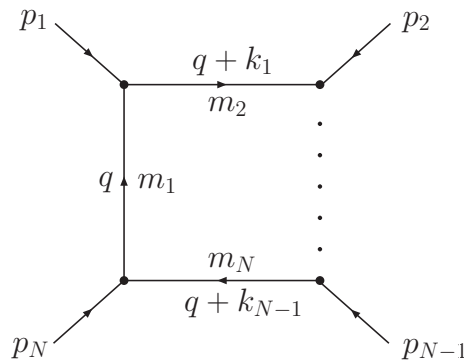

Figure D.1: Scheme of a general one-loop integral.

It is implicitly assumed that all propagators in the denominator have an infinitely small positive imaginary part ϵ which is set to zero after performing the integration. This corresponds to an explicit replacement of m_i^2 to $m_i^2 - i\epsilon$. Following the convention in [122], A denotes the one-point integrals, B the two-point integrals, etc.

As shown in [123], the tensor integrals can be systematically reduced to linear combinations of Lorentz covariant tensors constructed from the metric tensor $g_{\mu\nu}$ and a linearly independent set of the momenta. The choice of this set is not unique.

We choose, for instance, the momenta of incoming and outgoing partons in the process of top quark pair production. We follow the notation of section 6.1.1. The decomposition of tensor loop-integrals that are relevant for our calculations reads [106], in the case of two-point functions,

$$\frac{i}{16\pi^2}(B_0; p_\mu B_1)(p^2, m_t, \lambda) = \mu^{4-D} \int \frac{d^D q}{(2\pi)^D} \frac{(1; q_\mu)}{[q^2 - m_t^2][(q+p)^2 - \lambda^2]} \ , \qquad \text{(D.3)}$$

The photon mass parameter λ is used to regularize the IR singularities. Explicit formulae for the one- and two-point integrals are given below.

The three-point functions, defined as

$$\frac{i}{16\pi^2}(C_0; C_\mu; C_{\mu\nu}) = \mu^{4-D} \int \frac{d^D q}{(2\pi)^D} \frac{(1; q_\mu; q_\mu q_\nu)}{\Delta_1 \Delta_2 \Delta_3} \ , \qquad \text{(D.4)}$$

with

$$\Delta_1 = q^2 - \lambda^2 \ , \qquad \Delta_2 = (q - p_2)^2 - m_t^2 \ , \qquad \Delta_3 = (q + p_1 - p_3)^2 - m_t^2 \ , \quad \text{(D.5)}$$

can be decomposed in the following way:

$$
\begin{aligned}
C_\mu &= -p_{2\mu} C_1^1 + (p_1 - p_3)_\mu C_1^2 \ , \\
C_{\mu\nu} &= p_{2\mu} p_{2\nu} C_2^1 + (p_1 - p_3)_\mu (p_1 - p_3)_\nu C_2^2 + g_{\mu\nu} C_2^0 \\
&\quad - \left(p_{2\mu}(p_1 - p_3)_\nu + (p_1 - p_3)_\mu p_{2\nu} \right) C_2^{12} \ .
\end{aligned}
\qquad \text{(D.6)}
$$

The calculation of the box contributions requires decomposition of the four-point tensor integrals up to the rank three.

$$\frac{i}{16\pi^2}(D_0; D_\mu; D_{\mu\nu}; D_{\mu\nu\rho}) = \mu^{4-D} \int \frac{d^D q}{(2\pi)^D} \frac{(1; q_\mu; q_\mu q_\nu; q_\mu q_\nu q_\rho)}{\Delta_1 \Delta_2 \Delta_3 \Delta_4} \ , \qquad \text{(D.7)}$$

with

$$\Delta_4 = (q + p_1)^2 - m_t^2 \ , \qquad \text{(D.8)}$$

in the case of gg fusion.

In the $q\bar{q}$ annihilation subprocess, an additional IR singularity occurs and the propagators need to be rearranged as

$$
\begin{aligned}
\Delta_1 &= q^2 - m_t^2 , & \Delta_2 &= (q - p_2)^2 - \lambda^2 , \\
\Delta_3 &= (q + p_1 - p_3)^2 - m_t^2 , & \Delta_4 &= (q + p_1)^2 - m_t^2 .
\end{aligned}
\tag{D.9}
$$

The decomposition of the four-point tensor integrals as done in [106] reads

$$
\begin{aligned}
D_\mu &= -p_{2\mu} D_1^1 + (p_1 - p_3)_\mu D_1^2 + p_{1\mu} D_1^3 , \\
D_{\mu\nu} &= p_{2\mu} p_{2\nu} D_2^1 + (p_1 - p_3)_\mu (p_1 - p_3)_\nu D_2^2 + p_{1\mu} p_{1\nu} D_2^3 + g_{\mu\nu} D_2^0 \\
&\quad - (p_{2\mu}(p_1 - p_3)_\nu + (p_1 - p_3)_\mu p_{2\nu}) D_2^{12} - (p_{2\mu} p_{1\nu} + p_{1\mu} p_{2\nu}) D_2^{13} \\
&\quad + ((p_1 - p_3)_\mu p_{1\nu} + p_{1\mu}(p_1 - p_3)_\nu) D_2^{23} , \\
D_{\mu\nu\rho} &= p_{2\mu} p_{2\nu} p_{2\rho} D_3^1 + (p_1 - p_3)_\mu (p_1 - p_3)_\nu (p_1 - p_3)_\rho D_2^3 p_{1\mu} + p_{1\mu} p_{1\rho} D_3^3 \\
&\quad - (g_{\mu\nu} p_{2\rho} + cyc.) D_3^{01} + (g_{\mu\nu}(p_1 - p_3)_\rho + cyc.) D_3^{02} \\
&\quad + (g_{\mu\nu}(p_{1\rho} + cyc.) D_3^{03} + ((p_1 - p_3)_\mu p_{2\nu} p_{1\rho} + cyc.) D_3^{12} \\
&\quad - (p_{2\mu}(p_1 - p_3)_\nu p_{1\rho} + cyc.) D_3^{21} + (p_{1\mu} p_{2\nu} p_{2\rho} + cyc.) D_3^{13} \\
&\quad - (p_{2\mu} p_{1\nu} p_{1\rho} + cyc.) D_3^{31} + (p_{1\mu}(p_1 - p_3)_\nu (p_1 - p_3)_\rho + cyc.) D_3^{23} \\
&\quad + ((p_1 - p_3)_\mu p_{1\nu} p_{1\rho} + cyc.) D_3^{32} \\
&\quad - (p_{2\mu}(p_1 - p_3)_n u p_{1\rho} + perm.) D_3^{123} ,
\end{aligned}
\tag{D.10}
$$

where *cyc.* and *perm.* denote cyclic commutation and permutation of the indices, respectively.

Furthermore, the coefficients of the tensor decomposition can be expressed as functions of the scalar integrals [123]. A complete set of reduction equations for the one-loop integrals up to the rank four can be found in e.g. [150]. The expressions for the two-, three- and four-point scalar loop integrals were first given in [122]. Further improvements have been done in [124, 125].

The explicit analytical formula for the one-point scalar function A_0 in D dimensions reads

$$
\begin{aligned}
A_0(m) &= m^2 \left[\frac{2}{\epsilon} - \gamma_E + \ln 4\pi - \ln \frac{m^2}{\mu^2} + 1 \right. \\
&\quad \left. + \frac{1}{4} \left(\left(-\gamma_E + \ln 4\pi - \ln \frac{m^2}{\mu^2} + 1 \right)^2 + 1 + \frac{\pi^2}{6} \right) \epsilon \right] + \mathcal{O}(\epsilon^2) .
\end{aligned}
\tag{D.11}
$$

Here γ_E is the Euler-Mascheroni constant with numerical value $\gamma_E = 0.577216\ldots$. The $\frac{1}{\epsilon}$-term substitutes the UV divergence of the integral. As the transition from $D = 4 - \epsilon$

dimensions to four dimensions corresponds to $\epsilon \to 0$, we can neglect the $\mathcal{O}(\epsilon)$ terms and rewrite the one-point scalar integral into the commonly used form

$$A_0(m) = m^2 \left(\Delta - \ln \frac{m^2}{\mu^2} + 1 \right) + \mathcal{O}(\epsilon) , \tag{D.12}$$

with

$$\Delta = \frac{2}{\epsilon} - \gamma_E + \ln 4\pi . \tag{D.13}$$

The two-point scalar function B_0 can be expressed analytically as

$$
\begin{aligned}
B_0(p^2, m_1, m_2) \;=\;& \Delta + 2 - \ln \frac{m_1 m_2}{\mu^2} + \frac{m_1^2 - m_2^2}{p^2} \ln \frac{m_2}{m_1} \\
& - \frac{m_1 m_2}{p^2} \left(\frac{1}{r} - r \right) \ln r + \mathcal{O}(\epsilon) ,
\end{aligned}
\tag{D.14}
$$

where the parameter r is determined by the equation

$$x^2 + \frac{m_1^2 + m_2^2 - p^2 - i\epsilon}{m_1 m_2} x + 1 = (x + r)\left(x + \frac{1}{r} \right) . \tag{D.15}$$

The two-point function B_1 can be expressed in terms of scalar functions A_0 and B_0:

$$B_1(p^2, m_1, m_2) = \frac{1}{2p^2} \left[(m_2^2 - m_1^2 - p^2)B_0 + A_0(m_1) - A_0(m_2) \right] . \tag{D.16}$$

We also give definition of the dilogarithm by means of the integral representation

$$\text{Li}_2(z) = - \int_0^1 dt \, \frac{\ln(1 - tz)}{t} , \qquad z \in \mathbb{C} \backslash \{ x \in \mathbb{R} \, : \, x > 1 \} . \tag{D.17}$$

Appendix E

Analytical expressions for the NLO QED corrections

The QED 1-loop corrections to $q\bar{q}$ annihilation subprocess are given by

$$\delta\mathcal{M}_{q\bar{q}} = \delta\mathcal{M}_{q\bar{q}}^{in} + \delta\mathcal{M}_{q\bar{q}}^{fin} + \delta\mathcal{M}_{q\bar{q}}^{box} , \tag{E.1}$$

where the initial- and final-state vertex contributions can be written as

$$
\begin{aligned}
\mathcal{M}_{q\bar{q}}^{in} &= \delta_{\alpha\beta}\, \bar{u}_t^j(p_2)(-ig_s T_{jl}^c\gamma_\mu)\, v_{\bar{t}}^l(p_1) \left(\frac{-ig^{\mu\nu}}{\hat{s}}\right) \bar{v}_\beta^k(p_3)(i\hat{\Lambda}_\nu^{in})\, u_\alpha^i(p_4) , \\
\mathcal{M}_{q\bar{q}}^{fin} &= \delta_{\alpha\beta}\, \bar{u}_t^j(p_2)(i\hat{\Lambda}_\mu^{fin})\, v_{\bar{t}}^l(p_1) \left(\frac{-ig^{\mu\nu}}{\hat{s}}\right) \bar{v}_\beta^k(p_3)(-ig_s T_{ik}^c\gamma_\nu)\, u_\alpha^i(p_4) .
\end{aligned}
\tag{E.2}
$$

Here we follow the same notation as introduced in sections 6.1.1 and 6.2.1. The photon mass is regularized by the mass parameter λ. In order to obtain IR-finite results, also the real corrections of photon bremsstrahlung have to be added.

The renormalized quark-gluon vertex functions can be described in terms of UV-finite form factors in the following way:

$$i\hat{\Lambda}_\mu(\hat{s}) = (-ig_s T^c)\frac{\alpha}{4\pi}Q_q^2 \left[\gamma_\mu F_V + (p_3 - p_4)_\mu \frac{1}{2m_q}F_M\right] . \tag{E.3}$$

In general, axial-vector form factors could also be introduced, however, as a result of the interference with the Born matrix element $\mathcal{M}_B^{q\bar{q}}$ these do not contribute. As the light quark masses are set to zero whenever possible, when calculating the initial-state vertex contribution, also the magnetic term F_M is negligible. The vector form factor can be expressed in a compact form (given in e.g. [126])

$$
\begin{aligned}
F_V(s, m_q) &= 2\ln\left(\frac{\lambda^2}{s}\right)\left[\ln\left(\frac{s}{m_q^2}\right) - 1\right] + \ln^2\left(\frac{s}{m_q^2}\right) \\
&\quad + \ln\left(\frac{s}{m_q^2}\right) + \frac{\pi^2}{3} - 4 .
\end{aligned}
\tag{E.4}
$$

In the case of final-state top-quark pairs, the expressions for the vector and magnetic form factors read

$$
\begin{aligned}
F_V(s, m_t) &= \left\{ 2(s - 2m_t^2) C_0(s, m_t, m_t, \lambda) + 2 - 2\ln\left(\frac{\lambda^2}{m_t^2}\right) \right. \\
&\quad \left. - 3\left[B_0(s, m_t, m_t) - \Delta_{m_t} \right] \right\} , \tag{E.5} \\
F_M(s, m_t) &= \frac{4m_t^2}{4m_t^2 - s}\left[B_0(s, m_t, m_t) - \Delta_{m_t} - 2 \right] , \tag{E.6}
\end{aligned}
$$

with $\Delta_{m_t} = \Delta + \ln(\mu^2/m_t^2)$. In the expressions above, we use the notations and conventions for the loop-functions of App. D and we have skipped the $\hat{s}$ notation.

The expressions for the gluon-photon box contributions, $\delta\mathcal{M}_{q\bar{q}}^{box}$, are not presented here as they can be found in the exact form in [126] for the e^+e^- annihilation to heavy fermion pairs and can be deduced from there by simple substitutions $m_e \leftrightarrow m_q$ and $m_f \leftrightarrow m_t$ and appropriate choices of the coupling constant and of the color factor.

In the gg fusion subprocess, the one-loop matrix element is composed of self-energy, vertex and box contributions:

$$
\delta\mathcal{M}_{gg} = \delta\mathcal{M}_{gg}^{vert} + \delta\mathcal{M}_{gg}^{vert} + \delta\mathcal{M}_{gg}^{box} , \tag{E.7}
$$

The single QED contributions can be expressed in a compact way in terms of the coefficients of the standard matrix elements, which are also used in *FormCalc*. We closely follow the approach in [106] and refer to it for notations and conventions. In the case of photonic contributions, the standard matrix elements do not consist of axial-vector terms.

The s-channel vertex contribution can be expressed in the same way as the final-state vertex correction in the $q\bar{q}$ channel. The same expressions for the form factors are valid. In the t-channel (u-channel can be obtained by simple substitutions $t \leftrightarrow u$, $p_3 \leftrightarrow p_4$, $\epsilon_3 \leftrightarrow \epsilon_4$ and $T^a \leftrightarrow T^b$) the coefficients of the standard matrix elements are given by

$$
\begin{aligned}
G_1^{V,t} &= 4Q_t^2\Big[(t + m_t^2)C_0 - 2C_2^0 + B_0(0, m_t, m_t) - \frac{1}{2} + (t + 3m_t^2)C_1^1 \\
&\quad + 2(t + m_t^2)C_1^2 \Big] + 2\delta Z_V(m_t^2) , \\
G_4^{V,t} &= -4Q_t^2(t - m_t^2)\big[C_0 + C_1^1 + + 2C_1^2 + 2C_2^2 + C_2^{12} \big] , \\
G_{11}^{V,t} &= 4Q_t^2\Big[-2tC_0 + 2C_2^0 + -B_0(0, m_t, m_t) + \frac{1}{2} \\
&\quad - 2(t + m_t^2)C_1^1 - (3t + m_t^2)C_1^2 \Big] - 2\delta Z_V(m_t^2) , \\
G_{14}^{V,t} &= 4Q_t^2\big[C_1^1 + C_1^2 + C_2^1 + C_2^2 + C_2^{12} \big] , \\
G_{16}^{V,t} &= -4G_{14}^{V,t} , \tag{E.8}
\end{aligned}
$$

with $C_0 = C_0(t, m_t, m_t, \lambda)$ and $C_i^j = C_i^j(t, m_t, m_t, \lambda)$.

Concerning the self-energy contribution to the t-channel, the coefficients of the standard matrix elements can be expressed as

$$
\begin{aligned}
\hat{\Sigma}_V^t(t) &= 2Q_t^2 \left[-B_1(t, m_t, \lambda) - \frac{1}{2} \right] + \delta Z_V(m_t^2) , \\
\hat{\Sigma}_S^t(t) &= 4Q_t^2 \left[-B_0(t, m_t, \lambda) + \frac{1}{2} \right] + \frac{\delta m_t}{m_t} - \delta Z_V(m_t^2) .
\end{aligned} \tag{E.9}
$$

In the case of t-channel box contribution (u-channel can be obtained by simple substitutions $t \leftrightarrow u$, $p_3 \leftrightarrow p_4$, $\epsilon_3 \leftrightarrow \epsilon_4$ and $T^a \leftrightarrow T^b$), the coefficients of the standard matrix elements are given in the following:

$$
\begin{aligned}
G_1^{\square,t} &= 2Q_t^2 \big[-C_0 + (2m_t^2 - s)D_0 - 2(s - 4m_t^2)D_1^1 \\
&\quad - (s - 4m_t^2)D_1^2 + 6D_2^0 + t(2D_2^2 + D_3^2) \\
&\quad + 2(t + m_t^2)(D_2^{12} + D_3^{21}) + 6D_3^{02} + 2m_t^2 D_3^{12} - (s - 2m_t^2)D_3^{123} \big] , \\
G_2^{\square,t} &= 2Q_t^2 \big[-C_0 + D_2^0 + t(2D_2^2 + D_3^2) \\
&\quad + 2(t + m_t^2)(D_2^{12} + D_3^{21}) + 4D_3^{02} + 2m_t^2 D_3^{12} - (s - 2m_t^2)D_3^{123} \big] , \\
G_4^{\square,t} &= 4Q_t^2 \big[C_0 + 4(m_t^2 - s)D_1^1 + (t + m_t^2)(D_1^2 + D_3^{12} + D_3^{123}) - 4D_2^0 \\
&\quad + (t + m_t^2 - s)D_2^{12} - (s - 2m_t^2)(D_2^1 + D_2^{13}) \\
&\quad + 2(D_3^{01} - D_3^{02}) + m_t^2 D_3^1 + t D_3^{21} + (3m_t^2 - s)D_3^{13} \big] , \\
G_6^{\square,t} &= 4Q_t^2 \big[2D_1^2 + 6D_2^{12} + 3D_2^2 + D_3^2 + 2D_3^{12} + 4D_3^{21} + 2D_3^{123} \big] , \\
G_{11}^{\square,t} &= 2Q_t^2 \big[2C_0 + (s - 2m_t^2)D_0 - 2(t + m_t^2)D_1^1 \\
&\quad + 2(t + m_t^2)(D_2^1 + D_2^{13} + D_3^{12} + D_3^{123}) + 2t(2D_2^{12} + D_3^{21}) \\
&\quad - 4D_2^0 + 12D_3^{01} + 2m_t^2(D_3^1 - D_1^2) - 2(s - 3m_t^2)D_3^{13} \big] , \\
G_{12}^{\square,t} &= -4Q_t^2 \big[4D_2^0 + 2(t + m_t^2)(D_2^1 + D_2^{13}) + 2(3t + m_t^2)D_2^{12} \\
&\quad + t(2D_2^2 + D_3^2) + 8D_3^{01} + 4D_3^{02} + 2m_t^2 D_3^1 + 2(t + 2m_t^2)D_3^{12} \\
&\quad + 2(2t + m_t^2)D_3^{21} + 2(3m_t^2 - s)D_3^{13} + (4m_t^2 - s + 2t)D_3^{123} \big] , \\
G_{14}^{\square,t} &= 4Q_t^2 \big[2D_1^1 + D_1^2 - D_2^1 - D_2^2 - 4D_2^{12} - 2D_2^{13} \big] , \\
G_{16}^{\square,t} &= -4Q_t^2 \big[8D_1^1 + 3D_1^2 + 3D_2^1 + 2D_2^2 + 8D_2^{12} + 3D_2^{13} + 2D_3^1 \\
&\quad + 6D_3^{12} + 6D_2^{13} + D_3^2 + 6D_3^{21} + 6D_3^{123} \big] ,
\end{aligned} \tag{E.10}
$$

where $C_0 = C_0(s, m_t, m_t, m_t)$, $D_0 = D_0(t, m_t, m_t, m_t, \lambda)$, and $D_i^j = D_i^j(t, m_t, m_t, m_t, \lambda)$. The full expressions for the gg channel can be obtained by combining the standard matrix elements as given in [106] with the expressions for their coefficients listed above.

Bibliography

[1] S. L. Glashow, Partial symmetries of weak interactions, *Nucl. Phys.* **22** (1961) 579–588.

S. Weinberg, A model of leptons, *Phys. Rev. Lett.* **19** (Nov, 1967) 1264–1266.

A. Salam, Weak and electromagnetic interactions, *Elementary Particle Theory, Proceedings Of The Nobel Symposium Held 1968 At Lerum, Sweden* (1986) 367–377.

[2] S. L. Glashow, J. Iliopoulos, and L. Maiani, Weak interactions with lepton-hadron symmetry, *Phys. Rev. D* **2** (Oct, 1970) 1285–1292.

[3] H. Fritzsch, M. Gell-Mann, and H. Leutwyler, Advantages of the color octet gluon picture, *Phys. Lett.* **B47** (1973) 365–368.

[4] D. J. Gross and F. Wilczek, Ultraviolet behavior of non-abelian gauge theories, *Phys. Rev. Lett.* **30** (1973) 1343–1346.

D. J. Gross and F. Wilczek, Asymptotically free gauge theories. 1, *Phys. Rev.* **D8** (1973) 3633–3652.

D. J. Gross and F. Wilczek, Asymptotically free gauge theories. 2, *Phys. Rev.* **D9** (1974) 980–993.

H. D. Politzer, Reliable perturbative results for strong interactions?, *Phys. Rev. Lett.* **30** (1973) 1346–1349.

H. D. Politzer, Asymptotic freedom: an approach to strong interactions, *Phys. Rept.* **14** (1974) 129–180.

[5] Particle Data Group Collaboration, W. M. Yao *et al.*, Review of particle physics, *J. Phys.* **G33** (2006) 1–1232.

[6] H. P. Nilles, Supersymmetry, supergravity and particle physics, *Phys. Rept.* **110** (1984) 1.

[7] H. E. Haber and G. L. Kane, The search for supersymmetry: probing physics beyond the standard model, *Phys. Rept.* **117** (1985) 75.

[8] F. del Aguila, J. A. Aguilar-Saavedra, and R. Pittau, Neutrino physics at large colliders, `hep-ph/0606198`.

[9] P. W. Higgs, Broken symmetries, massless particles and gauge fields, *Phys. Lett.* **12** (1964) 132–133.

P. W. Higgs, Broken symmetries and the masses of gauge bosons, *Phys. Rev. Lett.* **13** (1964) 508–509.

P. W. Higgs, Spontaneous symmetry breakdown without massless bosons, *Phys. Rev.* **145** (1966) 1156–1163.

F. Englert and R. Brout, Broken symmetry and the mass of gauge vector mesons, *Phys. Rev. Lett.* **13** (1964) 321–322.

T. W. B. Kibble, Symmetry breaking in non-Abelian gauge theories, *Phys. Rev.* **155** (1967) 1554–1561.

[10] N. Cabibbo, Unitary symmetry and leptonic decays, *Phys. Rev. Lett.* **10** (1963) 531–532.

M. Kobayashi and T. Maskawa, CP violation in the renormalizable theory of weak interaction, *Prog. Theor. Phys.* **49** (1973) 652–657.

[11] Y. Nambu, Axial vector current conservation in weak interactions, *Phys. Rev. Lett.* **4** (1960) 380–382.

J. Goldstone, Field theories with 'superconductor' solutions, *Nuovo Cim.* **19** (1961) 154–164.

J. Goldstone, A. Salam, and S. Weinberg, Broken symmetries, *Phys. Rev.* **127** (1962) 965–970.

[12] T. Hambye and K. Riesselmann, Matching conditions and Higgs mass upper bounds revisited, *Phys. Rev.* **D55** (1997) 7255–7262, [`hep-ph/9610272`].

[13] LEP Working Group for Higgs boson searches Collaboration, R. Barate *et al.*, Search for the standard model Higgs boson at LEP, *Phys. Lett.* **B565** (2003) 61–75, [`hep-ex/0306033`].

[14] The LEP Collaborations ALEPH, DELPGI, L3, OPAL and the LEP Electroweak Working Group Collaboration, A combination of preliminary electroweak measurements and constraints on the standard model, `hep-ex/0612034`.

[15] J. Erler, SM precision constraints at the LHC / ILC, `hep-ph/0701261`.

[16] G. 't Hooft, Renormalization of massless Yang-Mills fields, *Nucl. Phys.* **B33** (1971) 173–199.

G. 't Hooft, Renormalizable Lagrangians for massive Yang-Mills fields, *Nucl. Phys.* **B35** (1971) 167–188.

[17] L. D. Faddeev and V. N. Popov, Feynman diagrams for the Yang-Mills field, *Phys. Lett.* **B25** (1967) 29–30.

[18] H. Georgi and S. L. Glashow, Unity of all elementary particle forces, *Phys. Rev. Lett.* **32** (1974) 438–441.

[19] H. Fritzsch and P. Minkowski, Unified interactions of leptons and hadrons, *Ann. Phys.* **93** (1975) 193–266.

[20] U. Amaldi, W. de Boer, and H. Fürstenau, Comparison of grand unified theories with electroweak and strong coupling constants measured at LEP, *Phys. Lett.* **B260** (1991) 447–455.

U. Amaldi, W. de Boer, P. H. Frampton, H. Fürstenau, and J. T. Liu, Consistency checks of grand unified theories, *Phys. Lett.* **B281** (1992) 374–383.

[21] S. Weinberg, Implications of dynamical symmetry breaking, *Phys. Rev.* **D13** (1976) 974–996.

S. Weinberg, Implications of dynamical symmetry breaking: an addendum, *Phys. Rev.* **D19** (1979) 1277–1280.

[22] L. Susskind, Dynamics of spontaneous symmetry breaking in the Weinberg-Salam theory, *Phys. Rev.* **D20** (1979) 2619–2625.

[23] WMAP Collaboration, D. N. Spergel *et al.*, First year Wilkinson Microwave Anisotropy Probe (WMAP) observations: Determination of cosmological parameters, *Astrophys. J. Suppl.* **148** (2003) 175, [`astro-ph/0302209`].

[24] S. R. Coleman and J. Mandula, All possible symmetries of the S matrix, *Phys. Rev.* **159** (1967) 1251–1256.

[25] R. Haag, J. T. Lopuszanski, and M. Sohnius, All possible generators of super-symmetries of the S matrix, *Nucl. Phys.* **B88** (1975) 257.

[26] M. F. Sohnius, Introducing supersymmetry, *Phys. Rept.* **128** (1985) 39–204.

[27] S. Dimopoulos and H. Georgi, Softly broken supersymmetry and SU(5), *Nucl. Phys.* **B193** (1981) 150.

[28] N. Sakai, Naturalness in supersymmetric 'GUTS', *Zeit. Phys.* **C11** (1981) 153.

[29] L. Susskind, The gauge hierarchy problem, technicolor, supersymmetry, and all that. (talk), *Phys. Rept.* **104** (1984) 181–193.

[30] G. Jungman, M. Kamionkowski, and K. Griest, Supersymmetric dark matter, *Phys. Rept.* **267** (1996) 195–373, [`hep-ph/9506380`].

[31] M. Drees, An introduction to supersymmetry, `hep-ph/9611409`.

S. P. Martin, A supersymmetry primer, `hep-ph/9709356`.

[32] P. Fayet and J. Iliopoulos, Spontaneously broken supergauge symmetries and Goldstone spinors, *Phys. Lett.* **B51** (1974) 461–464.

[33] L. O'Raifeartaigh, Spontaneous symmetry breaking for chiral scalar superfields, *Nucl. Phys.* **B96** (1975) 331.

[34] A. H. Chamseddine, R. Arnowitt, and P. Nath, Locally supersymmetric grand unification, *Phys. Rev. Lett.* **49** (1982) 970.

R. Barbieri, S. Ferrara, and C. A. Savoy, Gauge models with spontaneously broken local supersymmetry, *Phys. Lett.* **B119** (1982) 343.

[35] H. P. Nilles, M. Srednicki, and D. Wyler, Weak interaction breakdown induced by supergravity, *Phys. Lett.* **B120** (1983) 346.

H. P. Nilles, M. Srednicki, and D. Wyler, Constraints on the stability of mass hierarchies in supergravity, *Phys. Lett.* **B124** (1983) 337.

E. Cremmer, P. Fayet, and L. Girardello, Gravity induced supersymmetry breaking and low–energy mass spectrum, *Phys. Lett.* **B122** (1983) 41.

[36] L. J. Hall, J. D. Lykken, and S. Weinberg, Supergravity as the messenger of supersymmetry breaking, *Phys. Rev.* **D27** (1983) 2359–2378.

[37] M. Dine and A. E. Nelson, Dynamical supersymmetry breaking at low–energies, *Phys. Rev.* **D48** (1993) 1277–1287, [`hep-ph/9303230`].

M. Dine, A. E. Nelson, Y. Nir, and Y. Shirman, New tools for low–energy dynamical supersymmetry breaking, *Phys. Rev.* **D53** (1996) 2658–2669, [`hep-ph/9507378`].

[38] G. F. Giudice and R. Rattazzi, Theories with gauge–mediated supersymmetry breaking, *Phys. Rept.* **322** (1999) 419–499, [`hep-ph/9801271`].

[39] H. E. Haber, Introductory low–energy supersymmetry, `hep-ph/9306207`.

[40] L. Girardello and M. T. Grisaru, Soft breaking of supersymmetry, *Nucl. Phys.* **B194** (1982) 65.

[41] R. N. Mohapatra and A. Rasin, A supersymmetric solution to CP problems, *Phys. Rev.* **D54** (1996) 5835–5844, [`hep-ph/9604445`].

[42] P. Fayet, Spontaneously broken supersymmetric theories of weak, electromagnetic and strong interactions, *Phys. Lett.* **B69** (1977) 489.

G. R. Farrar and P. Fayet, Phenomenology of the production, decay, and detection of new hadronic states associated with supersymmetry, *Phys. Lett.* **B76** (1978) 575–579.

[43] D. I. Kazakov, Beyond the Standard Model (in search of supersymmetry), `hep-ph/0012288`.

[44] B. C. Allanach *et al.*, Les Houches 'Physics at TeV colliders 2005' Beyond the Standard Model working group: Summary report, `hep-ph/0602198`.

[45] A. Djouadi, M. Drees, and J.-L. Kneur, Updated constraints on the minimal supergravity model, *JHEP* **03** (2006) 033, [`hep-ph/0602001`].

[46] CLIC Physics Working Group Collaboration, E. Accomando *et al.*, Physics at the CLIC multi-TeV linear collider, `hep-ph/0412251`.

[47] LHC/LC Study Group Collaboration, G. Weiglein *et al.*, Physics interplay of the LHC and the ILC, *Phys. Rept.* **426** (2006) 47–358, [`hep-ph/0410364`].

[48] K. Desch, E. Gross, S. Heinemeyer, G. Weiglein, and L. Zivkovic, LHC / LC interplay in the MSSM Higgs sector, *JHEP* **09** (2004) 062, [`hep-ph/0406322`].

[49] N. Arkani-Hamed and S. Dimopoulos, Supersymmetric unification without low energy supersymmetry and signatures for fine–tuning at the LHC, *JHEP* **06** (2005) 073, [`hep-th/0405159`].

G. F. Giudice and A. Romanino, Split supersymmetry, *Nucl. Phys.* **B699** (2004) 65–89, [`hep-ph/0406088`].

[50] N. Arkani-Hamed, S. Dimopoulos, G. F. Giudice, and A. Romanino, Aspects of split supersymmetry, *Nucl. Phys.* **B709** (2005) 3–46, [`hep-ph/0409232`].

W. Kilian, T. Plehn, P. Richardson, and E. Schmidt, Split supersymmetry at colliders, *Eur. Phys. J.* **C39** (2005) 229–243, [`hep-ph/0408088`].

[51] S. Dimopoulos and D. W. Sutter, The supersymmetric flavor problem, *Nucl. Phys.* **B452** (1995) 496–512, [`hep-ph/9504415`].

[52] F. Gabbiani, E. Gabrielli, A. Masiero, and L. Silvestrini, A complete analysis of FCNC and CP constraints in general SUSY extensions of the Standard Model, *Nucl. Phys.* **B477** (1996) 321–352, [`hep-ph/9604387`].

[53] J. R. Ellis, G. Ridolfi, and F. Zwirner, Radiative corrections to the masses of supersymmetric Higgs bosons, *Phys. Lett.* **B257** (1991) 83–91.

H. E. Haber and R. Hempfling, Can the mass of the lightest Higgs boson of the Minimal Supersymmetric Model be larger than m(Z)?, *Phys. Rev. Lett.* **66** (1991) 1815–1818.

Y. Okada, M. Yamaguchi, and T. Yanagida, Upper bound of the lightest Higgs boson mass in the Minimal Supersymmetric Standard Model, *Prog. Theor. Phys.* **85** (1991) 1–6.

[54] A. Brignole, Radiative corrections to the supersymmetric neutral Higgs boson masses, *Phys. Lett.* **B281** (1992) 284–294.

[55] P. H. Chankowski, S. Pokorski, and J. Rosiek, Charged and neutral supersymmetric Higgs boson masses: Complete one loop analysis, *Phys. Lett.* **B274** (1992) 191–198.

P. H. Chankowski, S. Pokorski, and J. Rosiek, Complete on–shell renormalization scheme for the minimal supersymmetric Higgs sector, *Nucl. Phys.* **B423** (1994) 437–496, [`hep-ph/9303309`].

[56] A. Dabelstein, The one loop renormalization of the MSSM Higgs sector and its application to the neutral scalar Higgs masses, *Z. Phys.* **C67** (1995) 495–512, [`hep-ph/9409375`].

[57] R. Hempfling and A. H. Hoang, Two loop radiative corrections to the upper limit of the lightest Higgs boson mass in the minimal supersymmetric model, *Phys. Lett.* **B331** (1994) 99–106, [`hep-ph/9401219`].

[58] S. Heinemeyer, W. Hollik, and G. Weiglein, QCD corrections to the masses of the neutral CP–even Higgs bosons in the MSSM, *Phys. Rev.* **D58** (1998) 091701, [`hep-ph/9803277`].

S. Heinemeyer, W. Hollik, and G. Weiglein, Precise prediction for the mass of the lightest Higgs boson in the MSSM, *Phys. Lett.* **B440** (1998) 296–304, [`hep-ph/9807423`].

[59] S. Heinemeyer, W. Hollik, and G. Weiglein, The masses of the neutral CP-even Higgs bosons in the MSSM: Accurate analysis at the two-loop level, *Eur. Phys. J.* **C9** (1999) 343–366, [`hep-ph/9812472`].

[60] R.-J. Zhang, Two-loop effective potential calculation of the lightest CP-even Higgs-boson mass in the MSSM, *Phys. Lett.* **B447** (1999) 89–97, [`hep-ph/9808299`].

J. R. Espinosa and R.-J. Zhang, MSSM lightest CP-even Higgs boson mass to $\mathcal{O}(\alpha_t \alpha_s)$: The effective potential approach, *JHEP* **03** (2000) 026, [`hep-ph/9912236`].

[61] G. Degrassi, P. Slavich, and F. Zwirner, On the neutral Higgs boson masses in the MSSM for arbitrary stop mixing, *Nucl. Phys.* **B611** (2001) 403–422, [`hep-ph/0105096`].

[62] J. R. Espinosa and R.-J. Zhang, Complete two-loop dominant corrections to the mass of the lightest CP-even Higgs boson in the Minimal Supersymmetric Standard Model, *Nucl. Phys.* **B586** (2000) 3–38, [`hep-ph/0003246`].

[63] A. Brignole, G. Degrassi, P. Slavich, and F. Zwirner, On the $\mathcal{O}(\alpha_t^2)$ two-loop corrections to the neutral Higgs boson masses in the MSSM, *Nucl. Phys.* **B631** (2002) 195–218, [`hep-ph/0112177`].

[64] A. Brignole, G. Degrassi, P. Slavich, and F. Zwirner, On the two-loop sbottom corrections to the neutral Higgs boson masses in the MSSM, *Nucl. Phys.* **B643** (2002) 79–92, [`hep-ph/0206101`].

[65] S. Heinemeyer, W. Hollik, H. Rzehak, and G. Weiglein, High–precision predictions for the MSSM Higgs sector at $\mathcal{O}(\alpha_{\rm b}\alpha_{\rm s})$, *Eur. Phys. J.* **C39** (2005) 465–481, [`hep-ph/0411114`].

[66] A. Dedes, G. Degrassi, and P. Slavich, On the two–loop Yukawa corrections to the MSSM Higgs boson masses at large $\tan\beta$, *Nucl. Phys.* **B672** (2003) 144–162, [`hep-ph/0305127`].

[67] G. Degrassi, S. Heinemeyer, W. Hollik, P. Slavich, and G. Weiglein, Towards high–precision predictions for the MSSM Higgs sector, *Eur. Phys. J.* **C28** (2003) 133–143, [`hep-ph/0212020`].

[68] S. Heinemeyer, W. Hollik, and G. Weiglein, The mass of the lightest MSSM Higgs boson: A compact analytical expression at the two–loop level, *Phys. Lett.* **B455** (1999) 179–191, [`hep-ph/9903404`].

[69] W. Pauli and F. Villars, On the invariant regularization in relativistic quantum theory, *Rev. Mod. Phys.* **21** (1949) 434–444.

[70] C. G. Bollini and J. J. Giambiagi, Dimensional renormalization: The number of dimensions as a regularizing parameter, *Nuovo Cim.* **B12** (1972) 20–25.

   J. F. Ashmore, A method of gauge invariant regularization, *Lett. Nuovo Cim.* **4** (1972) 289–290.

   G. 't Hooft and M. J. G. Veltman, Regularization and renormalization of gauge fields, *Nucl. Phys.* **B44** (1972) 189–213.

[71] W. Siegel, Supersymmetric dimensional regularization via dimensional reduction, *Phys. Lett.* **B84** (1979) 193.

[72] D. M. Capper, D. R. T. Jones, and P. van Nieuwenhuizen, Regularization by dimensional reduction of supersymmetric and nonsupersymmetric gauge theories, *Nucl. Phys.* **B167** (1980) 479.

[73] D. Stockinger, Regularization by dimensional reduction: Consistency, quantum action principle, and supersymmetry, *JHEP* **03** (2005) 076, [`hep-ph/0503129`].

[74] W. A. Bardeen, A. J. Buras, D. W. Duke, and T. Muta, Deep inelastic scattering beyond the leading order in asymptotically free gauge theories, *Phys. Rev.* **D18** (1978) 3998.

A. J. Buras, Asymptotic freedom in deep inelastic scattering processes in the leading order and beyond, *Rev. Mod. Phys.* **52** (1980) 199.

[75] W. J. Marciano and A. Sirlin, Precise SU(5) predictions for $\sin^2 \theta_W$, m_W and m_Z, *Phys. Rev. Lett.* **46** (1981) 163.

A. Sirlin, Role of $\sin^2 \theta_W(m_Z)$ at the Z^0 peak, *Phys. Lett.* **B232** (1989) 123.

[76] G. Passarino and M. J. G. Veltman, On the definition of the weak mixing angle, *Phys. Lett.* **B237** (1990) 537.

[77] M. Böhm, H. Spiesberger, and W. Hollik, On the one loop renormalization of the electroweak standard model and its application to leptonic processes, *Fortsch. Phys.* **34** (1986) 687–751.

W. F. L. Hollik, Radiative corrections in the Standard Model and their role for precision tests of the electroweak theory, *Fortschr. Phys.* **38** (1990) 165–260.

W. Hollik, Renormalization of the Standard Model, . *Langacker, P. (ed.): Precision tests of the standard electroweak model, Advanced series on directions in high-energy physics,* 37-116, also in MPI-Ph-93-021.

[78] A. Denner, Techniques for calculation of electroweak radiative corrections at the one loop level and results for W physics at LEP-200, *Fortschr. Phys.* **41** (1993) 307–420.

[79] T. Fritzsche, Berechnung von Observablen zur supersymmetrischen Teilchen-erzeugung an Hochenergie-Collidern unter Einschluss hoererer Ordnungen, PhD thesis, . Cuvillier, Göttingen, 2005, ISBN 3-86537-577-4.

[80] CTEQ Collaboration, R. Brock *et al.*, Handbook of perturbative QCD: Version 1.0, *Rev. Mod. Phys.* **67** (1995) 157–248.

[81] J. D. Bjorken and E. A. Paschos, Inelastic Electron Proton and gamma Proton Scattering, and the Structure of the Nucleon, *Phys. Rev.* **185** (1969) 1975–1982.

R. P. Feynman, Very high-energy collisions of hadrons, *Phys. Rev. Lett.* **23** (1969) 1415–1417.

R. P. Feynman, Photon-hadron interactions, . Reading 1972, 282p.

[82] J. C. Collins, D. E. Soper, and G. Sterman, Factorization of Hard Processes in QCD, *Adv. Ser. Direct. High Energy Phys.* **5** (1988) 1–91, [`hep-ph/0409313`].

[83] E. D. Bloom *et al.*, High-energy inelastic e p scattering at 6-degrees and 10-degrees, *Phys. Rev. Lett.* **23** (1969) 930–934.

M. Breidenbach *et al.*, Observed behavior of highly inelastic electron - proton scattering, *Phys. Rev. Lett.* **23** (1969) 935–939.

J. I. Friedman and H. W. Kendall, Deep inelastic electron scattering, *Ann. Rev. Nucl. Part. Sci.* **22** (1972) 203–254.

[84] J. D. Bjorken, Asymptotic Sum Rules at Infinite Momentum, *Phys. Rev.* **179** (1969) 1547–1553.

[85] G. Altarelli, R. K. Ellis, and G. Martinelli, Large Perturbative Corrections to the Drell-Yan Process in QCD, *Nucl. Phys.* **B157** (1979) 461.

[86] G. Curci, W. Furmanski, and R. Petronzio, Evolution of Parton Densities Beyond Leading Order: The Nonsinglet Case, *Nucl. Phys.* **B175** (1980) 27.

J. C. Collins and D. E. Soper, Parton distribution and decay functions, *Nucl. Phys.* **B194** (1982) 445.

[87] G. Altarelli and G. Parisi, Asymptotic Freedom in Parton Language, *Nucl. Phys.* **B126** (1977) 298.

[88] P. Nason, S. Dawson, and R. K. Ellis, The One Particle Inclusive Differential Cross-Section for Heavy Quark Production in Hadronic Collisions, *Nucl. Phys.* **B327** (1989) 49–92.

[89] A. De Rujula, R. Petronzio, and A. Savoy-Navarro, Radiative corrections to high-energy neutrino scattering, *Nucl. Phys.* **B154** (1979) 394.

J. Kripfganz and H. Perlt, Electroweak radiative corrections and quark mass singularities, *Z. Phys.* **C41** (1988) 319–321.

J. Blumlein, Leading log radiative corrections to deep inelastic neutral and charged current scattering at HERA, *Z. Phys.* **C47** (1990) 89–94.

[90] H. Spiesberger, QED radiative corrections for parton distributions, *Phys. Rev.* **D52** (1995) 4936–4940, [`hep-ph/9412286`].

[91] M. Roth and S. Weinzierl, QED corrections to the evolution of parton distributions, *Phys. Lett.* **B590** (2004) 190–198, [`hep-ph/0403200`].

[92] A. D. Martin, R. G. Roberts, W. J. Stirling, and R. S. Thorne, Parton distributions incorporating QED contributions, *Eur. Phys. J.* **C39** (2005) 155–161, [`hep-ph/0411040`].

[93] CDF Collaboration, F. Abe *et al.*, Observation of top quark production in $p\bar{p}$ collisions, *Phys. Rev. Lett.* **74** (1995) 2626–2631, [`hep-ex/9503002`].

[94] D0 Collaboration, S. Abachi *et al.*, Observation of the top quark, *Phys. Rev. Lett.* **74** (1995) 2632–2637, [`hep-ex/9503003`].

[95] Tevatron Electroweak Working Group Collaboration, E. Brubaker *et al.*, Combination of CDF and D0 results on the mass of the top quark, `hep-ex/0608032`.

[96] I. I. Y. Bigi, Y. L. Dokshitzer, V. A. Khoze, J. H. Kühn, and P. M. Zerwas, Production and decay properties of ultraheavy quarks, *Phys. Lett.* **B181** (1986) 157.

[97] CDF and D0 Collaboration, E. Shabalina, Top quark production cross section at the Tevatron, `hep-ex/0605045`.

D0 Collaboration, L. Cerrito and t. CDF, Measurements of the top quark at the Tevatron collider, `hep-ex/0701036`.

[98] F. Gianotti, Physics at the LHC, *Phys. Rept.* **403** (2004) 379–399.

[99] M. Glück, J. F. Owens, and E. Reya, Gluon contribution to hadronic J/ψ production, *Phys. Rev.* **D17** (1978) 2324.

B. L. Combridge, Associated production of heavy flavor states in pp and $p\bar{p}$ interactions: some QCD estimates, *Nucl. Phys.* **B151** (1979) 429.

J. Babcock, D. W. Sivers, and S. Wolfram, QCD estimates for heavy particle production, *Phys. Rev.* **D18** (1978) 162.

K. Hagiwara and T. Yoshino, Hadroproduction of heavy quark flavors in QCD, *Phys. Lett.* **B80** (1979) 282.

L. M. Jones and J. Wyld, H. W., Production of bound quark - anti-quark systems, *Phys. Rev.* **D17** (1978) 2332–2337.

H. M. Georgi, S. L. Glashow, M. E. Machacek, and D. V. Nanopoulos, Charmed particles from two - gluon annihilation in proton proton collisions, *Ann. Phys.* **114** (1978) 273.

[100] U. Baur, E. W. N. Glover, and A. D. Martin, Electroweak interference effects in two jet production at $p\bar{p}$ colliders, *Phys. Lett.* **B232** (1989) 519.

[101] V. S. Fadin and V. A. Khoze, Threshold behavior of heavy top production in e^+e^- collisions, *JETP Lett.* **46** (1987) 525–529.

V. S. Fadin, V. A. Khoze, and T. Sjostrand, On the threshold behavior of heavy top production, *Z. Phys.* **C48** (1990) 613–622.

[102] E. L. Berger and H. Contopanagos, The Perturbative Resummed Series for Top Quark Production in Hadron Reactions, *Phys. Rev.* **D54** (1996) 3085–3113, [`hep-ph/9603326`].

S. Catani, M. L. Mangano, P. Nason, and L. Trentadue, The Top Cross Section in Hadronic Collisions, *Phys. Lett.* **B378** (1996) 329–336, [`hep-ph/9602208`].

E. Laenen, J. Smith, and W. L. van Neerven, All order resummation of soft gluon contributions to heavy quark production in hadron hadron collisions, *Nucl. Phys.* **B369** (1992) 543–599.

E. Laenen, J. Smith, and W. L. van Neerven, Top quark production cross-section, *Phys. Lett.* **B321** (1994) 254–258, [`hep-ph/9310233`].

[103] R. Bonciani, S. Catani, M. L. Mangano, and P. Nason, NLL resummation of the heavy-quark hadroproduction cross- section, *Nucl. Phys.* **B529** (1998) 424–450, [`hep-ph/9801375`].

[104] M. Cacciari, S. Frixione, M. L. Mangano, P. Nason, and G. Ridolfi, The t anti-t cross-section at 1.8-TeV and 1.96-TeV: A study of the systematics due to parton densities and scale dependence, *JHEP* **04** (2004) 068, [`hep-ph/0303085`].

[105] N. Kidonakis and R. Vogt, Next-to-next-to-leading order soft-gluon corrections in top quark hadroproduction, *Phys. Rev.* **D68** (2003) 114014, [`hep-ph/0308222`].

[106] W. Beenakker, A. Denner, W. Hollik, R. Mertig, T. Sack, and D. Wackeroth, Electroweak one loop contributions to top pair production in hadron colliders, *Nucl. Phys.* **B411** (1994) 343–380.

[107] C. Kao, G. A. Ladinsky, and C. P. Yuan, Leading weak corrections to the production of heavy top quarks at hadron colliders, *Int. J. Mod. Phys.* **A12** (1997) 1341–1372.

[108] J. H. Kühn, A. Scharf, and P. Uwer, Electroweak corrections to top-quark pair production in quark-antiquark annihilation, *Eur. Phys. J.* **C45** (2006) 139–150, [`hep-ph/0508092`].

[109] S. Moretti, M. R. Nolten, and D. A. Ross, Weak corrections to gluon-induced $t\bar{t}$ hadro-production, *Phys. Lett.* **B639** (2006) 513–519, [`hep-ph/0603083`].

[110] W. Bernreuther, M. Fuecker, and Z.-G. Si, Weak interaction corrections to hadronic top quark pair production, *Phys. Rev.* **D74** (2006) 113005, [`hep-ph/0610334`].

[111] J. H. Kühn, A. Scharf, and P. Uwer, Electroweak effects in top-quark pair production at hadron colliders, `hep-ph/0610335`.

[112] A. Stange and S. Willenbrock, Yukawa correction to top quark production at the Tevatron, *Phys. Rev.* **D48** (1993) 2054–2061, [`hep-ph/9302291`].

[113] H.-Y. Zhou, C.-S. Li, and Y.-P. Kuang, Yukawa corrections to top quark production at the LHC in two-Higgs-doublet models, *Phys. Rev.* **D55** (1997) 4412–4420, [`hep-ph/9603435`].

[114] S. Alam, K. Hagiwara, S. Matsumoto, K. Hagiwara, and S. Matsumoto, One loop supersymmetric QCD radiative corrections to the top quark production in p anti-p collisions. (Revised version), *Phys. Rev.* **D55** (1997) 1307–1315, [`hep-ph/9607466`].

Z. Sullivan, Supersymmetric QCD correction to top-quark production at the Tevatron, *Phys. Rev.* **D56** (1997) 451–457, [`hep-ph/9611302`].

C.-S. Li, H.-Y. Zhou, Y.-L. Zhu, and J.-M. Yang, Strong supersymmetric quantum effects on top quark production at the Fermilab Tevatron, *Phys. Lett.* **B379** (1996) 135–140, [`hep-ph/9606271`].

C.-S. Li, B.-Q. Hu, J.-M. Yang, and C.-G. Hu, Supersymmetric QCD corrections to top quark production in p anti-p collisions, *Phys. Rev.* **D52** (1995) 5014–5017.

[115] J. Kim, J. L. Lopez, D. V. Nanopoulos, and R. Rangarajan, Enhanced supersymmetric corrections to top-quark production at the Tevatron, *Phys. Rev.* **D54** (1996) 4364–4373, [`hep-ph/9605419`].

[116] H.-Y. Zhou and C.-S. Li, Supersymmetric QCD corrections to top quark pair production at CERN LHC, *Phys. Rev.* **D55** (1997) 4421–4429.

[117] C.-S. Li, J.-M. Yang, Y.-l. Zhu, and H.-Y. Zhou, Yukawa corrections to top pair production in photon-photon collision, *Phys. Rev.* **D54** (1996) 4662–4676, [`hep-ph/9606382`].

[118] W. Hollik, W. M. Mösle, and D. Wackeroth, Top pair production at hadron colliders in non-minimal standard models, *Nucl. Phys.* **B516** (1998) 29–54, [`hep-ph/9706218`].

[119] J. Küblbeck, M. Böhm, and A. Denner, Feyn Arts: Computer algebraic generation of Feynman graphs and amplitudes, *Comput. Phys. Commun.* **60** (1990) 165–180.

T. Hahn, Generating Feynman diagrams and amplitudes with FeynArts 3, *Comput. Phys. Commun.* **140** (2001) 418–431, [`hep-ph/0012260`].

T. Hahn and C. Schappacher, The implementation of the minimal supersymmetric standard model in FeynArts and FormCalc, *Comput. Phys. Commun.* **143** (2002) 54–68, [`hep-ph/0105349`].

[120] T. Hahn, New developments in FormCalc 4.1, `hep-ph/0506201`.

[121] T. Hahn and M. Perez-Victoria, Automatized one-loop calculations in four and D dimensions, *Comput. Phys. Commun.* **118** (1999) 153–165, [`hep-ph/9807565`].

[122] G. 't Hooft and M. J. G. Veltman, Scalar one loop integrals, *Nucl. Phys.* **B153** (1979) 365–401.

[123] G. Passarino and M. J. G. Veltman, One loop corrections for e+ e- annihilation into $\mu^+\mu^-$ in the Weinberg Model, *Nucl. Phys.* **B160** (1979) 151.

[124] W. Beenakker and A. Denner, Infrared divergent scalar box integrals with applications in the electroweak Standard Model, *Nucl. Phys.* **B338** (1990) 349–370.

[125] A. Denner, U. Nierste, and R. Scharf, A compact expression for the scalar one loop four point function, *Nucl. Phys.* **B367** (1991) 637–656.

[126] W. Beenakker, S. C. van der Marck, and W. Hollik, e^+e^- annihilation into heavy fermion pairs at high-energy colliders, *Nucl. Phys.* **B365** (1991) 24–78.

[127] F. Bloch and A. Nordsieck, Note on the radiation field of the electron, *Phys. Rev.* **52** (1937) 54–59.

[128] S. Dittmaier, A general approach to photon radiation off fermions, *Nucl. Phys.* **B565** (2000) 69–122, [`hep-ph/9904440`].

[129] S. Dittmaier and M. Krämer, Electroweak radiative corrections to W-boson production at hadron colliders, *Phys. Rev.* **D65** (2002) 073007, [`hep-ph/0109062`].

[130] S. Catani and M. H. Seymour, The dipole formalism for the calculation of QCD jet cross sections at next-to-leading order, *Phys. Lett.* **B378** (1996) 287–301, [`hep-ph/9602277`].

S. Catani and M. H. Seymour, A general algorithm for calculating jet cross sections in NLO QCD, *Nucl. Phys.* **B485** (1997) 291–419, [`hep-ph/9605323`].

[131] U. Baur, S. Keller, and D. Wackeroth, Electroweak radiative corrections to W boson production in hadronic collisions, *Phys. Rev.* **D59** (1999) 013002, [`hep-ph/9807417`].

[132] K. P. O. Diener, S. Dittmaier, and W. Hollik, Electroweak higher-order effects and theoretical uncertainties in deep-inelastic neutrino scattering, *Phys. Rev.* **D72** (2005) 093002, [`hep-ph/0509084`].

[133] J. R. Ellis and S. Rudaz, Search for supersymmetry in toponium decays, *Phys. Lett.* **B128** (1983) 248.

[134] A. Djouadi, J. Kalinowski, P. Ohmann, and P. M. Zerwas, Heavy SUSY Higgs bosons at e^+e^- linear colliders, *Z. Phys.* **C74** (1997) 93–111, [`hep-ph/9605339`].

[135] ALEPH Collaboration, A. Heister *et al.*, Search for scalar quarks in e^+e^- collisions at $\sqrt{s}$ up to 209-GeV, *Phys. Lett.* **B537** (2002) 5–20, [`hep-ex/0204036`].

DELPHI Collaboration, P. Abreu *et al.*, Search for supersymmetric partners of top and bottom quarks at $\sqrt{s} = 189$ GeV, *Phys. Lett.* **B496** (2000) 59–75, [`hep-ex/0103034`].

L3 Collaboration, M. Acciarri *et al.*, Searches for scalar quarks in e^+e^- interactions at $\sqrt{s} = 189$-GeV, *Phys. Lett.* **B471** (1999) 308–320, [`hep-ex/9910020`].

OPAL Collaboration, G. Abbiendi *et al.*, Search for scalar top and scalar bottom quarks at LEP, *Phys. Lett.* **B545** (2002) 272–284, [`hep-ex/0209026`].

[136] A. C. Kraan, Stop and sbottom searches at LEP, `hep-ex/0305051`.

[137] CDF Collaboration, A. A. Affolder *et al.*, Search for scalar top quark production in $p\bar{p}$ collisions at $\sqrt{s}$ = 1.8 TeV, *Phys. Rev. Lett.* **84** (2000) 5273–5278, [`hep-ex/9912018`].

The D0 Collaboration, V. M. Abazov *et al.*, Search for pair production of light scalar top quarks in $p\bar{p}$ collisions at $\sqrt{s}$ = 1.8 TeV, *Phys. Rev. Lett.* **93** (2004) 011801, [`hep-ex/0404028`].

[138] CDF and D0 Collaboration, T. Nunnemann, Searches for scalar top and bottom quarks at the Tevatron, *PoS* **HEP2005** (2006) 348, [`hep-ex/0602038`].

[139] H1 Collaboration, A. Aktas *et al.*, Search for bosonic stop decays in R-parity violating supersymmetry in $e^{+}p$ collisions at HERA, *Phys. Lett.* **B599** (2004) 159–172, [`hep-ex/0405070`].

ZEUS Collaboration, S. Chekanov *et al.*, Search for stop production in R-parity-violating supersymmetry at HERA, `hep-ex/0611018`.

[140] G. L. Kane and J. P. Leveille, Experimental constraints on gluino masses and supersymmetric theories, *Phys. Lett.* **B112** (1982) 227.

P. R. Harrison and C. H. Llewellyn Smith, Hadroproduction of supersymmetric particles, *Nucl. Phys.* **B213** (1983) 223.

E. Reya and D. P. Roy, Supersymmetric particle production at $p\overline{p}$ collider energies, *Phys. Rev.* **D32** (1985) 645.

S. Dawson, E. Eichten, and C. Quigg, Search for supersymmetric particles in hadron - hadron collisions, *Phys. Rev.* **D31** (1985) 1581.

H. Baer and X. Tata, Component formulae for hadroproduction of left-handed and right-handed squarks, *Phys. Lett.* **B160** (1985) 159.

[141] W. Beenakker, R. Höpker, M. Spira, and P. M. Zerwas, Squark production at the Tevatron, *Phys. Rev. Lett.* **74** (1995) 2905–2908, [`hep-ph/9412272`].

W. Beenakker, R. Höpker, M. Spira, and P. M. Zerwas, Squark and gluino production at hadron colliders, *Nucl. Phys.* **B492** (1997) 51–103, [`hep-ph/9610490`].

[142] W. Beenakker, M. Krämer, T. Plehn, M. Spira, and P. M. Zerwas, Stop production at hadron colliders, *Nucl. Phys.* **B515** (1998) 3–14, [`hep-ph/9710451`].

[143] A. Bartl *et al.*, Search of stop, sbottom, tau-sneutrino, and stau at an $e^{+}e^{-}$ linear collider with $\sqrt{s}$ = 0.5-TeV to 2-TeV, *Z. Phys.* **C76** (1997) 549–560, [`hep-ph/9701336`].

[144] G. Bozzi, B. Fuks, and M. Klasen, Non-diagonal and mixed squark production at hadron colliders, *Phys. Rev.* **D72** (2005) 035016, [hep-ph/0507073].

[145] W. Beenakker, R. Höpker, T. Plehn, and P. M. Zerwas, Stop decays in SUSY-QCD, *Z. Phys.* **C75** (1997) 349–356, [hep-ph/9610313].

A. Djouadi, W. Hollik, and C. Jünger, QCD corrections to scalar quark decays, *Phys. Rev.* **D55** (1997) 6975–6985, [hep-ph/9609419].

S. Kraml, H. Eberl, A. Bartl, W. Majerotto, and W. Porod, QCD corrections to scalar quark decays, *Phys. Lett.* **B386** (1996) 175–182, [hep-ph/9605412].

[146] B. C. Allanach *et al.*, The Snowmass points and slopes: Benchmarks for SUSY searches, hep-ph/0202233.

[147] G. Weiglein, The LHC / LC study group and the snowmass points and slopes, hep-ph/0301111.

[148] J. A. Aguilar-Saavedra *et al.*, Supersymmetry parameter analysis: SPA convention and project, *Eur. Phys. J.* **C46** (2006) 43–60, [hep-ph/0511344].

[149] J. Wess and B. Zumino, Supergauge transformations in four-dimensions, *Nucl. Phys.* **B70** (1974) 39–50.

J. Wess and B. Zumino, Supergauge invariant extension of quantum electrodynamics, *Nucl. Phys.* **B78** (1974) 1.

[150] A. Denner and S. Dittmaier, Reduction of one-loop tensor 5-point integrals, *Nucl. Phys.* **B658** (2003) 175–202, [hep-ph/0212259].

Acknowledgements

I would like to thank to all who supported me during the work on the thesis.